

Physical characterization of brown dwarfs

Elena Manjavacas

Max-Planck-Institut für Astronomie

Heidelberg 2014

Dissertation in Astronomy

submitted to the

**Combined Faculties of the Natural Sciences and Mathematics
of the Ruperto-Carola-University of Heidelberg, Germany,**

for the degree of

Doctor of Natural Sciences

Put forward by

M.Sc. *Elena Manjavacas*

born in Mota del Cuervo, España

Oral examination: 03.02.2015

Physical characterization of brown dwarfs

Elena Manjavacas

Max-Planck-Institut für Astronomie

**Referees: Prof. Dr. Thomas Henning
Prof. Dr. Norbert Christlieb**

Zusammenfassung

Die Ursprüngliche Massenfunktion beschreibt die Masseverteilung einer Sternpopulation und kleineren Objekten zum Zeitpunkt ihrer Geburt. Sie definiert die Entwicklung der Sternpopulation und gibt Auskunft über die Sternentstehungsgeschichte. Die Bestimmung der Ursprünglichen Massenfunktion im substellaren Bereich ist bis heute eine ungeklärte Frage in der Astrophysik. Braune Zwerge haben nicht genug Masse um das Wasserstoffbrennen aufrecht zu erhalten. Als Konsequenz sind Masse und Alter entartet und somit kann ein älteres massereiches Objekt von einem jungen massearmen Objekt nicht unterschieden werden. In dieser Doktorarbeit werde ich, mit Hilfe verschiedener Beobachtungsmethoden zur Charakterisierung Brauner Zwerge, daran arbeiten das allgemeine Problem zur Bestimmung der Ursprünglichen Massenfunktion besser zu verstehen.

In meinem ersten Projekt berechnete ich die trigonometrische Parallaxe einer Auswahl von 6 kalten Braunen Zwergen. Ich bestimmte die Leuchtkraft für diese Objekte und fand heraus, dass möglicherweise ein Objekt ein binäres System aus zwei Braunen Zwergen ist. In meinem zweiten Projekt bestätigte, ich mit Hilfe spektroskopischer Daten, die Alter von sieben Braunen Zwergen (die Alter liegen zwischen 1 Million und 150 Millionen Jahren). Das Ziel des letzten Projekts meiner Doktorarbeit war es den Anteil der binären Systeme Brauner Zwerge, mit Hilfe spektroskopischer Daten von 22 Objekten im Optischen und Nahinfraroten, genauer zu bestimmen. Ich fand sechs neue Kandidaten binärer Systeme Brauner Zwerge, von denen bereits zwei bekannt gewesen waren. Die, in dieser Doktorarbeit, bestimmten Distanzen, Alter und Anteile binärer Systeme von Braunen Zwergen tragen zur Bestimmung der Ursprünglichen Massenfunktion bei.

In den nächsten Jahren werden der Gaia Satellit, das James Webb Teleskop und das E-ELT neue Daten liefern, die uns erlauben weitere Binärsysteme Brauner Zwerge zu entdecken, deren Atmosphäre und Entwicklung und die Ursprüngliche Massenfunktion zu bestimmen.

Abstract

The initial mass function describes the distribution of masses for a population of stars and sub-stellar objects when they are born. It defines the evolution of a population of stars and provides constraints on the star formation theory. The determination of the initial mass function in the sub-stellar regime is still an open question in Astrophysics. Brown dwarfs do not have enough mass to sustain hydrogen fusion. As a consequence, mass and age are degenerate for these objects. An older high mass object may be indistinguishable from a younger low mass object. In this PhD thesis, through the characterization of brown dwarfs using several observational methods, I work towards solving the general problem of constraining the substellar initial mass function.

In my first project, I calculated trigonometric parallaxes of a sample of six cool brown dwarfs. I determined the luminosity for our objects and I found that one of them might be a brown dwarf binary. In my second project, I confirmed the youth of seven brown dwarfs (ages between 1 and 150 Myr) using spectroscopic data. In the last project of this PhD thesis, I aimed to refine the brown dwarf binary fraction using spectroscopic data in the optical and in the near infrared for 22 brown dwarfs. I found six new brown dwarf binary candidates, two of them were previously known. The determination of distances, ages and the refinement of the brown dwarf binary fraction in this PhD thesis contribute to the determination of the initial mass function.

In the next years, the Gaia satellite, the James Webb Space Telescope and the E-ELT will provide new data, allowing the discovery of new brown dwarf binaries, the constraining of atmospheric and evolutionary models, and the refinement of the initial mass function.

PUBLICATIONS

Some of the ideas and work described in this thesis have previously appeared in the following publications:

Parallaxes of cool brown dwarfs, Manjavacas, E.; Goldman, B.; Reffert, S.; Henning, T., 2013, *Astronomy & Astrophysics*. Vol. 560, pp. 52

New constraints on the formation and settling of dust in the atmospheres of young M and L dwarfs, Manjavacas, E.; Bonnefoy, M.; Schlieder, J. E.; Allard, F.; Rojo, P.; Goldman, B.; Chauvin, G.; Homeier, D.; Lodieu, N.; Henning, 2014, *Astronomy & Astrophysics*. Vol. 564, pp. 21

Hunting for binaries with X-Shooter spectra, Manjavacas, E.; Goldman, B.; Alcalá, J. M.; Zapatero-Osorio, M. R.; Béjar, V. J. S.; Homeier, D.; Bonnefoy, M.; Smart, R. L.; Henning, T.; Allard, F., 2014, submitted to *Astronomy & Astrophysics*.

A mis padres y a mi tío Rafa ...

CONTENTS

1	INTRODUCTION	1
1.1	THE INITIAL MASS FUNCTION AND THE IMPORTANCE OF BROWN DWARF CHARACTERIZATION	1
1.2	BROWN DWARFS: NEITHER STARS NOR PLANETS	2
1.2.1	ULTRACOOL DWARF SPECTRAL CHARACTERISTICS	5
1.2.2	YOUNG BROWN DWARFS: BROWN DWARFS OR FREE-FLOATING PLANETS?	5
1.2.3	BROWN DWARF BINARITY	7
1.3	BROWN DWARF ATMOSPHERIC MODELS	8
2	OUTLINE OF THIS DISSERTATION	11
2.1	PARALLAXES OF COOL BROWN DWARFS	11
2.2	NEW CONSTRAINTS ON THE FORMATION AND SETTLING OF DUST IN THE ATMOSPHERES OF YOUNG M AND L DWARFS	12
2.3	HUNTING FOR BROWN DWARF BINARIES WITH X-SHOOTER	13
3	PARALLAX MEASUREMENTS OF COOL BROWN DWARFS	15
3.1	INTRODUCTION	15
3.2	OBSERVATIONS	16

3.3	ANALYSIS	17
3.3.1	ASTROMETRY	17
3.3.2	DCR CORRECTION	18
3.3.3	PARALLAXES	19
3.3.3.1	Relative parallaxes	19
3.3.3.2	Correction from relative to absolute parallax	19
3.3.4	ABSOLUTE PARALLAX ACCURACY	20
3.4	RESULTS	21
3.5	DISCUSSION	21
3.5.1	2MASS J11061197+2754225	21
3.5.2	ULAS J130217.21+130851.2	22
3.5.3	ULAS J141756.22+133045.8	22
3.5.4	2MASS J22541892+3123498	23
3.5.5	ULAS J232035.28+144829.8	23
3.5.6	ULAS J232123.79+135454.9	23
3.6	CONCLUSIONS	24
3.A	STELLAR PATHS OF THE TARGETS	28
4	NEW CONSTRAINTS ON THE FORMATION AND SETTLING OF DUST IN THE ATMOSPHERES OF YOUNG M AND L DWARFS	31
4.1	INTRODUCTION	31
4.2	OBSERVATIONS AND DATA REDUCTION	32
4.3	EMPIRICAL ANALYSIS	33
4.3.1	AN AGE-SEQUENCE OF M9.5 DWARFS	33
4.3.2	YOUNG FIELD L-DWARFS?	36
4.3.3	INDICES AND EQUIVALENT WIDTHS	38

4.4	SPECTRAL SYNTHESIS	43
4.4.1	NEAR-INFRARED SPECTRA	45
4.4.2	SPECTRAL ENERGY DISTRIBUTIONS	50
4.5	DISCUSSION	52
4.5.1	BEHAVIOR OF ATMOSPHERIC MODELS	52
4.5.2	REVISED PROPERTIES	54
4.5.2.1	DENIS-P J124514.1-442907 (TWA 29)	55
4.5.2.2	EROS-MP J0032-4405	56
4.5.2.3	Cha J130540.8-773958	58
4.5.2.4	2MASS J22134491-2136079	59
4.6	CONCLUSIONS	59
4.A	PROPERTIES OF THE SPECTRA OF YOUNG COMPANIONS	61
4.B	BEST MATCHES OF EROS J0032, 2M 2213, 2M 2126, AND 2M 2208 WITH LIBRARY SPECTRA.	62
5	HUNTING FOR BROWN DWARF BINARIES WITH X-SHOOTER	65
5.1	INTRODUCTION	65
5.2	THE SAMPLE, OBSERVATIONS AND DATA REDUCTION	66
5.2.1	SAMPLE SELECTION	66
5.2.2	OBSERVATIONS AND DATA REDUCTION	66
5.3	EMPIRICAL ANALYSIS	69
5.3.1	FINDING L PLUS T BROWN DWARF BINARIES	69
5.3.2	FINDING L PLUS L OR T PLUS T BROWN DWARF BINARIES	71
5.4	EQUIVALENT WIDTHS	78
5.5	COMPARISON TO SYNTHETIC SPECTRA	82
5.6	REVISED PROPERTIES	83

5.6.1	SIMP 01365662+0933473	87
5.6.2	DENIS-P J0255.0-4700	88
5.6.3	2MASS J13411160-3052505	88
5.6.4	2MASS J00531899-3631102	89
5.6.5	2MASS J02572581-3105523	89
5.7	VERY LOW MASS BINARY FRACTION	90
5.8	CONCLUSIONS	90
5.A	OBSERVING LOG	92
5.B	BEST MATCHES TO POTENTIAL L PLUS T BINARIES	97
5.C	SYNTHETIC L PLUS L OR T PLUS T BEST MATCHES TO TEMPLATE SPECTRA	97
5.D	BEST MATCHES REST OF OBJECTS	97
	SUMMARY AND FUTURE WORK	109
	ACKNOWLEDGMENTS	113
	BIBLIOGRAPHY	115

“Man must rise above the Earth, to the top of the atmosphere and beyond, for only thus will he fully understand the world in which he lives.”

— Socrates

The existence of substellar objects with masses between stars and planets was theoretically predicted 50 years ago. Only 20 years ago, the first brown dwarfs were discovered. Since then, more than 1000 brown dwarfs have been found, establishing the connection between stars and planets.

1.1 THE INITIAL MASS FUNCTION AND THE IMPORTANCE OF BROWN DWARF CHARACTERIZATION

The initial mass function (IMF) is an empirical function that describes the distribution of masses for a population of stars and substellar objects when they are born. The Vogt-Russell Theorem states that the structure of a star in hydrostatic and thermal equilibrium is determined by the total mass and the chemical composition of the star, provided that the total pressure, the internal energy per unit mass, opacity and energy generation rate are functions only of the local values of density, temperature and chemical composition. Furthermore, the mass and composition of a star determine its radius, luminosity and its evolution in the Hertzsprung-Russell (HR) diagram. Therefore, if the IMF is known for a population of stars with broadly the same composition, we can determine the evolution of this population.

The empirical determination of the IMF and its possible variations in time and space provide fundamental constraints on the star formation theory. Many stars form in groups in star forming regions and clusters. The observed IMF in these regions provide information on the mass distribution and how the initial general and local conditions influence the distribution of the stellar masses.

The first attempts to empirically derive the IMF were made by Salpeter (1955) and Miller & Scalo (1979), who derived the IMF by studying the luminosity function, i.e. the number of stars per luminosity interval, of field stars in the Solar neighborhood. Salpeter (1955) determined that the IMF is a power law: $\phi(m) \propto m^{-\alpha}$, in which $\alpha = 2.35$ for stars with masses between $0.4M_{\odot}$ and $10M_{\odot}$. This IMF shows that the number of stars in each mass range increases rapidly with decreasing mass. Miller & Scalo (1979) improved the luminosity function of Salpeter (1955) using the newest parallax data at that time and extended the IMF down to $0.1M_{\odot}$ and up to $50M_{\odot}$. Kroupa (2001) updated the IMF to allow the power law to change depending on the mass interval. Chabrier (2003) attempted to extend the IMF ($\phi(m)$) down to the substellar regime:

$$\phi(m)\Delta m = \frac{A}{m} \exp\left[-\frac{(\log(m) - \log(m_c))^2}{2\sigma^2}\right], \text{ for objects with } M < 1M_{\odot},$$

$$\text{where: } A = 0.158^{+0.051}_{-0.046}; m_c = 0.079^{+0.021}_{-0.016}; \sigma = 0.69^{+0.05}_{-0.01}$$

Nevertheless, as this result is based in theoretical brown dwarf models, which did not account for all complex processes like dust sedimentation, cloud diffusion, and non-equilibrium chemistry, the IMF derived by Chabrier (2003) in the substellar regime needs to be utilized with care. In Figure 1.1 (Bastian et al. 2010), I show the value of Γ ($\alpha = \Gamma + 1$) for the IMF for clusters, nearby star-formation regions, associations, and the field as a function of sampled stellar mass together with the IMF from Salpeter (1955), Kroupa (2001) and Chabrier (2003).

Objects in the substellar regime ($M \leq 75M_{\text{Jup}}$) do not have enough mass to sustain hydrogen fusion, therefore during their evolution, substellar objects cool down (Chabrier & Baraffe 1997; Burrows et al. 1997a) and are never static in luminosity or in the HR diagram. This implies that there is no direct relation between spectral types, masses and ages. Due to the difficulty in measuring masses, it is challenging to constrain the IMF in the substellar regime.

There have been several attempts to determine the field IMF in the substellar regime using simulations (Burgasser 2004; Deacon et al. 2008; Day-Jones et al. 2013) and in several open clusters (Zapatero Osorio et al. 2004a; Caballero et al. 2007; Melnikov & Eisloffel 2012; Scholz et al. 2013). Nevertheless, it is necessary to characterize volume-limited samples in the field to address observationally the problem of the IMF in the substellar regime.

1.2 BROWN DWARFS: NEITHER STARS NOR PLANETS

Brown dwarfs ($13M_{\text{Jup}} < M < 75M_{\text{Jup}}$) are substellar objects which are not able to sustain hydrogen fusion.

In 1963 Kumar (1963a,b) inferred the existence of a limiting mass below which a contracting star cannot reach the main-sequence stage because the temperature and density at the center are too low for hydrogen-

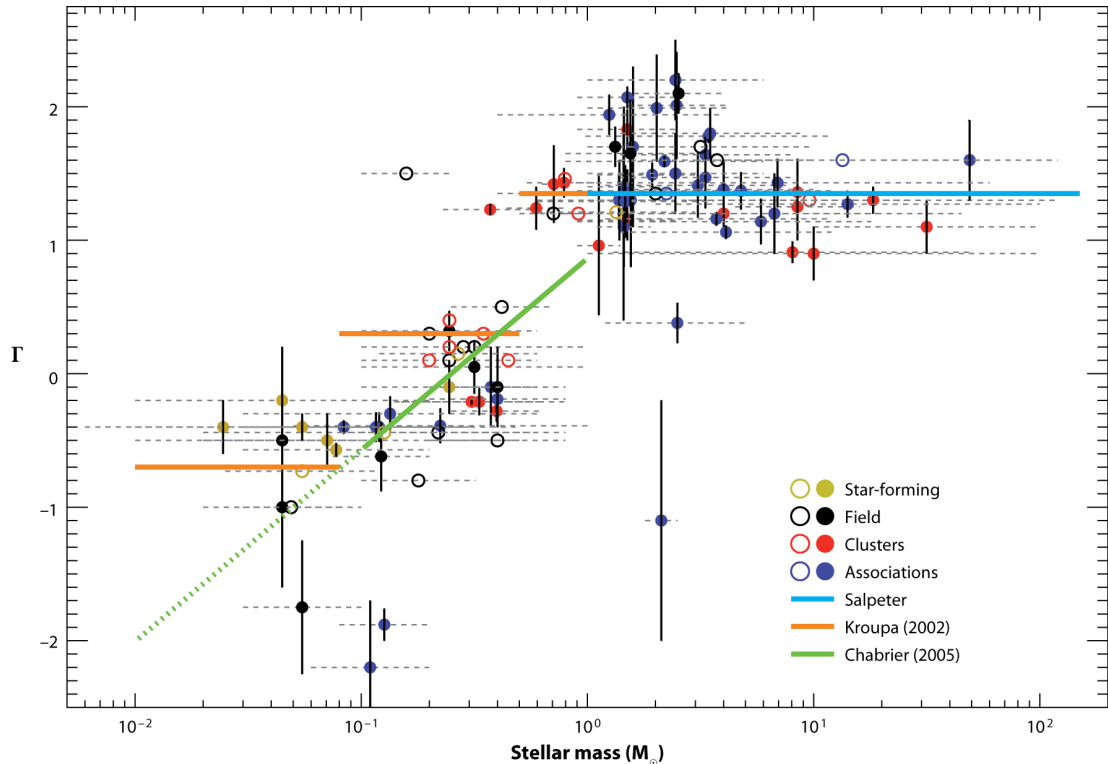


Figure 1.1: From Bastian et al. (2010). A representation of the alpha plot by Scalo (1998) and Kroupa (2001). We show the derived index, Γ ($\alpha = \Gamma + 1$), of the initial mass function (IMF) in clusters, nearby star-forming regions, associations, and the field as a function of sampled stellar mass. The colored solid lines represent three analytical IMFs: Shown in green is the Chabrier (2003) IMF (the dashed green line is an extrapolation into the substellar regime), with the Salpeter (1955) IMF in light blue, and the Kroupa (2001) IMF in orange (which is essentially Salpeter above $1M_{\odot}$). Open circles represent results from studies where no errors for Γ are provided. Filled circles are accompanied with their corresponding errors.

burning to start. Calculating convective interior models for stars with masses between 0.09 and 0.04 solar masses (M_{\odot}), he estimated the hydrogen-burning mass limit to be $0.07M_{\odot}$ for objects belonging to the population I (solar metallicity objects) and $0.09M_{\odot}$ for objects that belong to the population II (low metallicity objects) (Kumar 1963a,b). In the core of objects with masses below these limits, the slow increment of the central temperature, combined with the quick increment of the central density will cause the core gas to become partially degenerate, before the core temperature is high enough to begin thermonuclear reactions. Kumar called these objects *black dwarfs*. At the same time, Hayashi & Nakano (1963) developed a similar theory to determine the hydrogen-burning minimum mass, determining this limit at $0.07M_{\odot}$, with a maximum core temperature of 3.5×10^6 K. Objects with masses below this limit cool down indefinitely. The term *brown dwarf* was not introduced until 1975 by J. Tarter, to differentiate these objects from another kind of object which had already been named black dwarfs, specifically those white dwarfs that have cooled down to a point at which they do not emit significant heat.

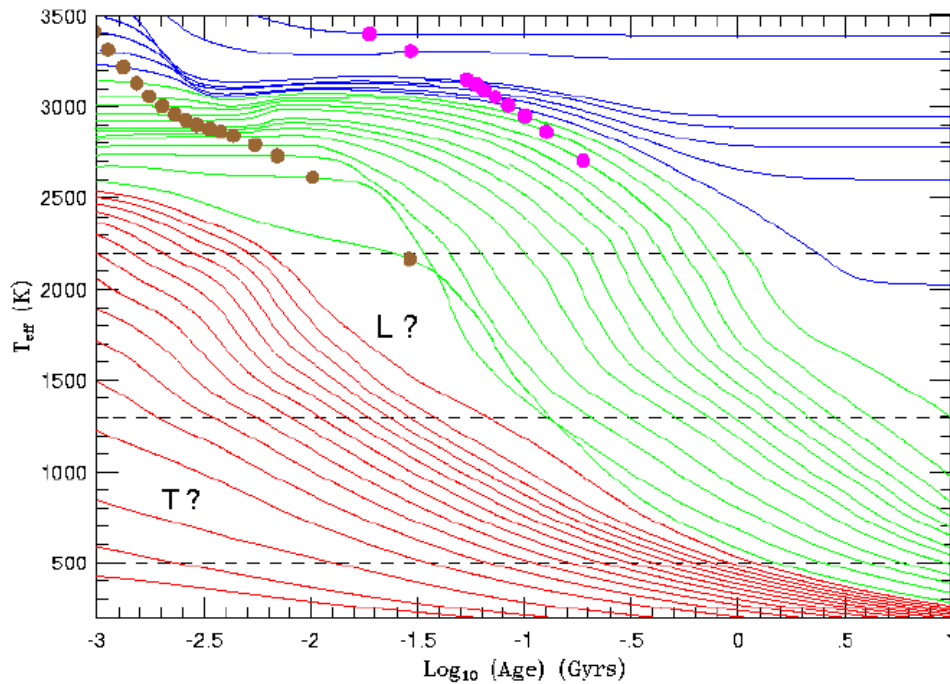


Figure 1.2: From Burrows et al. (2001). Evolution of temperature with time for stars (blue lines), brown dwarfs (green lines) and exoplanets (red lines). Every line represents the evolution of temperature for a different mass. For a given object, the gold dots mark when 50% of the deuterium has burned and the magenta dots mark when 50% of the lithium has burned.

30 years after their theoretical prediction, the first brown dwarfs were discovered. The first brown dwarfs to be found were GD165 (Becklin & Zuckerman 1988), PPI 15 (Basri et al. 1995), Teide1 (Rebolo et al. 1995) and Gliese229B (Nakajima et al. 1995). This last one was the first T brown dwarf discovered. Since then, with 2MASS, DENIS, SDSS, UKIDSS and WISE surveys, more than 1000 brown dwarfs have been found¹. During their lives, brown dwarfs cool down and change spectral types, moving from the M, to the L, the T and finally to the recently discovered, Y spectral class (Cushing et al. 2011).

In Figure 1.2 the temperature of low mass stars ($\sim 80M_{\text{Jup}}$ - blue lines), brown dwarfs ($13M_{\text{Jup}}$ to $73M_{\text{Jup}}$ - green lines) and exoplanets ($0.3M_{\text{Jup}}$ to $13M_{\text{Jup}}$ - red lines) are shown. As brown dwarfs cool down with time, in contrast to stars, there is no correlation between spectral types, masses and ages. This is the so-called age-mass degeneracy (Burrows et al. 2001).

¹www.dwarfarchives.org

1.2.1 ULTRACOOL DWARF SPECTRAL CHARACTERISTICS

During their evolution, brown dwarfs cool down effective temperature, therefore changing spectral types and molecular and atomic spectral characteristics. There are several molecular absorptions and atomic lines present in the spectra of M, L and T dwarfs, the most important in the red optical and near infrared:

- In the z-band we find Ti, Fe, Ca, Si and Mg atomic lines, in M-dwarfs, that disappear in early L-dwarfs. The FeH molecular absorption at $0.9969 \mu\text{m}$ is also present in the M-dwarfs. The VO band at $\sim 1.06 \mu\text{m}$ appears in the mid-M dwarfs and it is maximum at M9, and disappears in the mid-L dwarfs. The amount of flux in this band decreases with spectral type.
- In the J-band we find the Na I doublet at $1.14 \mu\text{m}$ and the two K doubles at 1.175 and $1.25 \mu\text{m}$ in the M, L and T dwarfs. In the M until the mid-L, the Fe feature at $1.189 \mu\text{m}$ is present. In the T dwarfs, we find the CH₄ bands from 1.15 to $1.25 \mu\text{m}$.
- In the H-band we find in H₂O band from the mid-M dwarfs through the L and T dwarf sequence. Absorption due to the FeH molecule appears in the mid-M dwarfs in the wavelength range between 1.59 to $1.75 \mu\text{m}$ (Cushing et al. 2003). In the T sequence, appear the CH₄ bands at $\sim 1.67 \mu\text{m}$ and are also present in the late L-dwarfs (McLean et al. 2003).
- In the K-band, there are ¹²CO molecular absorptions from $2.29 \mu\text{m}$ in the M and L dwarfs and H₂O bands from mid-M dwarfs through the L and T sequence. CH₄ bands at $2.2 \mu\text{m}$ appear in late L dwarfs onwards.

1.2.2 YOUNG BROWN DWARFS: BROWN DWARFS OR FREE-FLOATING PLANETS?

Young brown dwarfs, with ages below 200 Myr, are still contracting (Burrows et al. 1997b; Baraffe et al. 1998a). Therefore, young objects can have larger radii, lower gravity and higher luminosities than older and more massive objects despite an identical effective temperature. In Fig. 1.3, Burrows et al. (2001) presents models that represent the evolution of radii with time for stars (blue lines), brown dwarfs (green lines) and exoplanets (red lines).

Low surface gravity affects in the optical and near infrared spectra of young brown dwarfs. Young objects with low surface gravity have weaker alkali lines in the optical and in the near infrared, their H-band spectra have a triangular shape and they have redder colors in the near infrared compared to their older counterparts. Redder colors in the near infrared may be due to a dustier atmosphere. The sedimentation of dust is less efficient in young brown dwarfs due to their low surface gravities and the dust persists in the high atmosphere of these objects. In Figure 1.4, from Manjavacas et al. (2014), I show an age-sequence of spectra in the J and K band of several objects with the same spectral type (M9.5), but with different gravities. We can observe the effect of gravity for the different objects ($g \sim M/R^2$).

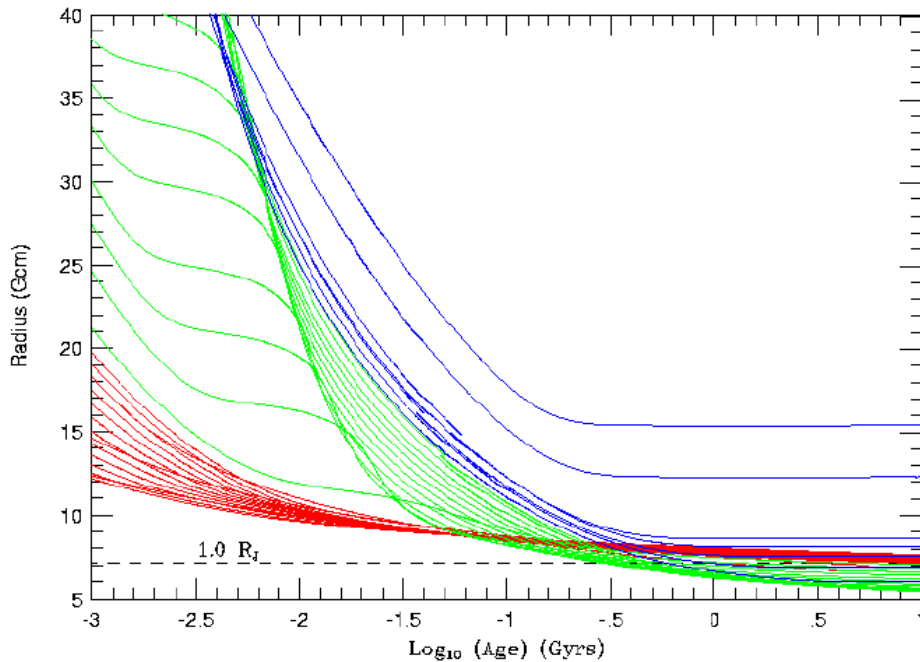


Figure 1.3: From Burrows et al. (2001). Evolution of radius with time for stars (blue lines), brown dwarfs (green lines) and exoplanets (red lines). Every line represents the evolution of radius for a different mass.

Young brown dwarfs have usually lower masses as well, some of them below minimal brown dwarf mass. This limit is defined by the IAU in $13 M_{\text{Jup}}$, and it is the minimum mass to burn deuterium. However, this mass limit does not differentiate between possible origins of the object. There are some companions to stars with masses higher than $13 M_{\text{Jup}}$, as for example NGC 4349 127 b, with $M \sim 20 M_{\text{Jup}}$ (Lovis & Mayor 2007), and free-floating objects with masses below $13 M_{\text{Jup}}$, like for example Cha 110913-773444 with $M \sim 8 M_{\text{Jup}}$ (Luhman et al. 2005a). This brings up a very important question: should NGC 4349 127 b considered a brown dwarf and Cha 110913-773444 a free-floating planet?

The exact boundary line between planets and brown dwarfs has been further come into question with the discovery of directly imaged planets. Some directly imaged planets are photometric and spectroscopic matches to L-type young brown dwarfs. An example of the difficulties in differentiating young brown dwarfs from exoplanets is given in Chapter 4 (Manjavacas et al. 2014). In this work, we found that the spectrum of the young L2 object, 2MASS J232252.99-615127.5 (Cruz et al. 2009a), is well reproduced by the spectrum of 1RXS J160929.1-210524b (Lafrenière et al. 2008a, 2010a), a planetary mass companion ($8_{-2}^{+4} M_{\text{Jup}}$) to a young solar-mass star. Thus, it is still unclear what observational difference between planetary-mass young brown dwarfs and planet companions to stars.

The study of the spectral characteristics of young objects provide an idea of the ages of these objects, allowing constraints on masses for these objects and therefore breaking the so-called age-mass degeneracy.

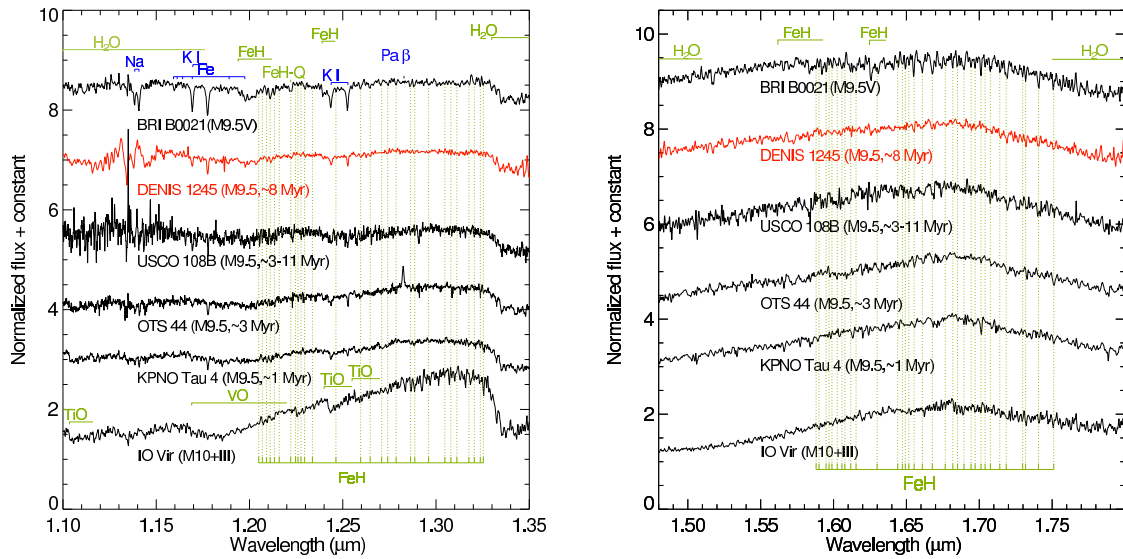


Figure 1.4: From Manjavacas et al. (2014). Age-sequence of different objects with similar spectral type (M9.5) and different gravities in the J (right plot) and H band (left plot). We can appreciate the difference of the spectral characteristics for these objects when we go from higher (upper spectrum) to lower gravities (bottom spectrum).

1.2.3 BROWN DWARF BINARITY

Most stars are discovered in binary or multiple systems (Raghavan et al. 2010). Binaries or multiple systems provide constraints on fundamental parameters such as dynamical masses (Konopacky et al. 2013) that are an essential test of the evolutionary models. Several authors derived empirical masses for brown dwarfs: Lane et al. (2001), Zapatero Osorio et al. (2004b), Dupuy et al. (2009), Dupuy et al. (2010), Konopacky et al. (2010), Dupuy & Liu (2012a) and Dupuy et al. (2014). Binaries are also contaminants to calculate number densities and the initial mass function. In addition, photometric distances estimated for binaries are systematically too low, due to their higher luminosity compared to single objects with the same spectral type.

The binary fraction decreases when the mass decreases, from 80%-60% for O, A and B stars to 40% for M dwarfs (Burgasser et al. 2007; Goldman et al. 2008). This tendency seems to continue in the brown dwarf regime, where the binary fraction is estimated to be around 20% for L- and T- brown dwarfs (Gizis et al. 2003; Burgasser et al. 2007; Goldman et al. 2008).

Allen (2007) used Bayesian techniques to retrieve the underlying mass ratio and semi-major axis distribution for low mass stellar and brown dwarf companions. He found the peak of the separation distribution of brown dwarfs is approximately 3 au (see Figure 1.5) and that 98% of the brown dwarf binaries have separations smaller than 20 au. The peak of the separation distribution is very close to the resolution limit of high resolution imaging surveys (Burgasser et al. 2007). The best resolution reached with HST (Hub-

ble Space Telescope) or with Keck II using adaptive optics is $0.2''$, so for brown dwarf binary systems at typical distances of 20-40 pc, the smallest separation we can resolve is 4-8 au.

Joergens (2008) concluded after studying brown dwarf binaries in the Chameleon star forming region, that the percentage of brown dwarfs systems with separations smaller than ~ 1 au is less than 10%.

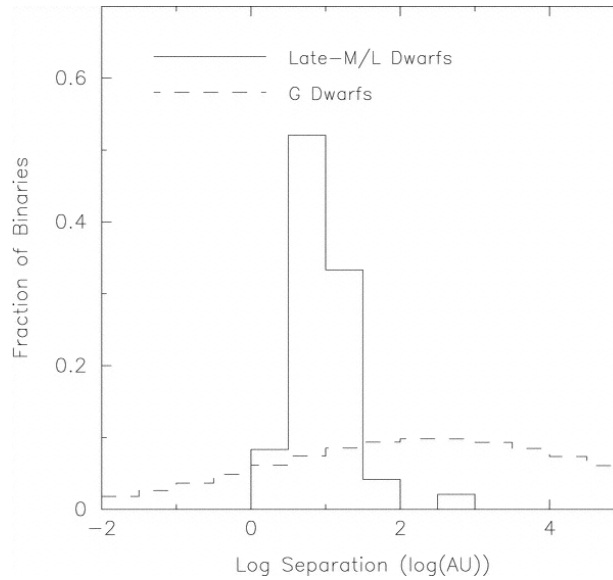


Figure 1.5: From Allen (2007). Separation distribution of M and L dwarfs (solid line, from Burgasser et al. (2007)) and G stars (dashed line, from Duquennoy & Mayor (1991)).

Burgasser et al. (2006, 2010) and Bardalez Gagliuffi et al. (2014b) have developed an empirical method to detect spectrally blended brown dwarf binaries (i.e. L plus T or M plus T) using seeing-limited spectroscopy, studying those parts of the spectra that are peculiar compared to single objects. In general these type of spectral binaries show a bluer spectral energy distribution in the near infrared than single objects of the same spectral type, and some spectral features are stronger, like the CH_4 and H_2O features at $1.1 \mu\text{m}$ which are deeper for binaries and the CH_4 feature at $1.6 \mu\text{m}$ which is stronger in comparison to the $2.2 \mu\text{m}$ CH_4 band.

1.3 BROWN DWARF ATMOSPHERIC MODELS

Atmospheric models allow us to disentangle the effect of varying T_{eff} , $\log g$, and (metallicity) M/H on the spectral features of brown dwarfs.

In Chapters 3, 4 and 5 we test different versions of the BT-Settl atmospheric models (Allard et al. 2001) using photometric colors (Chapter 3) or spectroscopy (Chapters 4 and 5).

The cloud model for the BT-Settl models are implemented in the PHOENIX in the atmospheric code version

15.5 (Allard et al. 2001). The PHOENIX models suppose the following assumptions:

- Local Thermodynamic Equilibrium (LTE): The emitted radiation is represented by a blackbody spectrum which interacts with the matter inside the volume. The Maxwell-Boltzmann distribution is used to calculate the number of atoms or molecules in different excited energy states. The Saha equation determines the number of atoms in different ionization states.
- Plane parallel and spherical atmospheres: The physical variables depend only on the vertical depth.
- Hydrostatic equilibrium: The object does not experience radical modifications in its structure, like large scale pulsations or mass loss.
- Mixing length and microturbulence: The convection in the atmosphere is described by the mixing-length theory, which models parcels of gas rising and disintegrating after a typical mixing length distance. This microturbulence is a form of turbulence that changes over small distance scales and causes broadening of the absorption lines in the spectrum and depends on the effective temperature and the surface gravity.

In the BT-Settl models, the opacity contribution of the strongest atomic lines are accounted for up to 5000Å from line centers. The atmospheric models are characterized by: 1/ surface gravity, $\log(g)$, 2/ effective temperature, T_{eff} , 3/ the mixing length, 4/ the microturbulence velocity, set to 2 km/s and 5/ the element abundances set to solar abundances.

The chemical equilibrium of the PHOENIX is solved for 40 elements with six ionization stages per element and 600 relevant molecular species for oxygen-rich ideal gas compositions (Allard & Hauschildt 1995). As brown dwarfs cool down with time, more condensates form and sediment out of the upper atmosphere. The BT-Settl models, adopt the equations for condensation, coagulation and sedimentation time scales from Rossow (1978). According to Allard et al. (2001) the models predict that most of the hydrogen is locked in H_2 , the oxygen is in CO , H_2O and SiO and the carbon in CO and CH_4 in brown dwarfs atmospheres. For T_{eff} lower than 2600 K, several species start to condensate. The first species to condensate is ZrO_2 at $T \sim 2000$ K and corundum (Al_2O_3) at $T \sim 1800$ K. At temperatures lower than 1600 K, MgAl_2O_4 , CaSiO_3 , Ca_2SiO_4 , $\text{Ca}_2\text{Al}_2\text{SiO}_7$, $\text{Ca}_2\text{MgSi}_2\text{O}_7$, $\text{CaMgSi}_2\text{O}_6$, Ti_4O_7 and Ti_2O_3 . When the effective temperature decreases, more grains appear, like enstatite (MgSiO_3) and forsterite (Mg_2SiO_4) and TiO , FeH and CaH are strongly depleted. Other less reactive elements like Li , K , Rb , Cs and CrH are unaffected and the detection of their features is easier in these objects' spectra. At effective temperatures between 1800 and 1000 K methane (CH_4) appears and CO disappears.

The BT-Settl models assume a plane-parallel symmetry, i.e. an homogeneous distribution of clouds across the surfaces of brown dwarfs. The number of density grains is provided by the chemical equilibrium calculations. The grains have diameters between 0.00625 and 0.24 μm .

The molecular opacity database includes: 1/ a list of 43×10^6 atomic transitions (Kurucz 1994), 2/ collision-induced absorption opacities for H_2 , He , H , N_2 , Ar , CH_4 and CO_2 (Borysow et al. 1997), 3/ H_2O and TiO

linelist (Schwenke 1998), 4/ a CO linelist (Goorvitch 1994; Goorvitch & Chackerian 1994b,a), 5/ VO and CrH lines and 6/ FeH lines (Phillips & Davis 1993).

In Figure 1.6 the result of the computed BT-Settl models is shown.

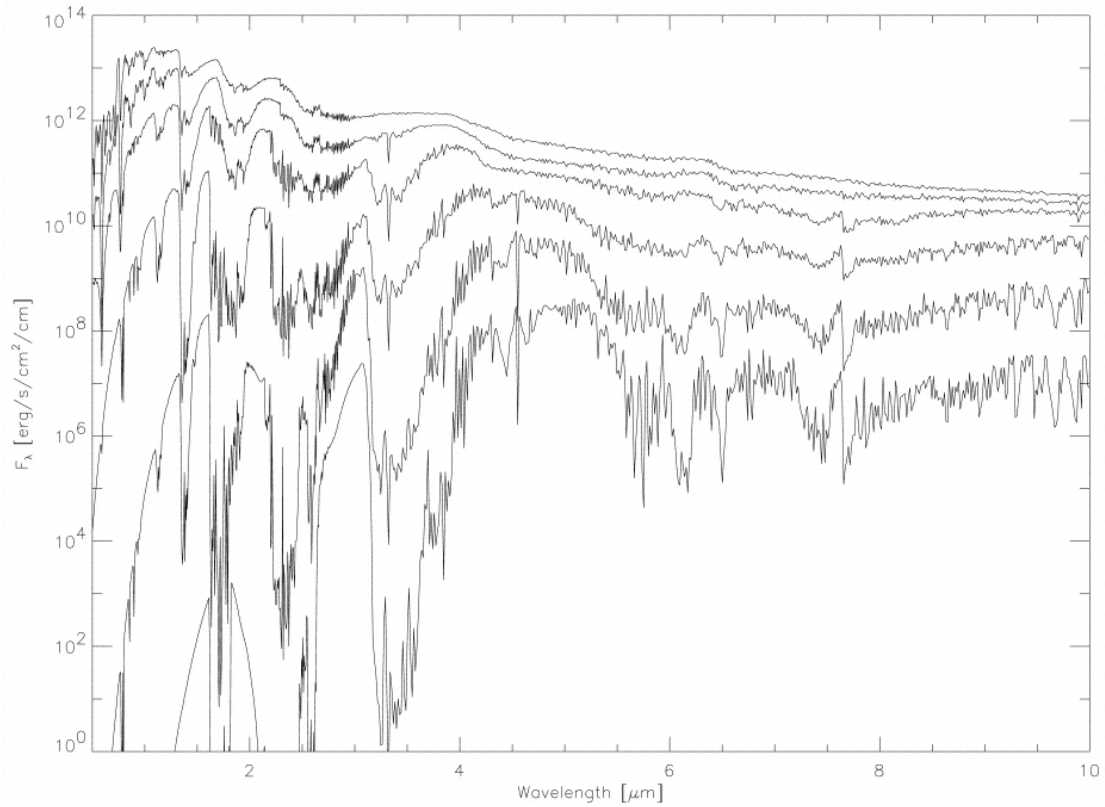


Figure 1.6: From Allard et al. (2001). Spectral sequence of synthetic spectra of brown dwarfs. From top to bottom, $T_{\text{eff}} = 2500, 1900, 1300, 700, 400$ and 200 K, for $\log g = 5.0$.

OUTLINE OF THIS DISSERTATION

In order to determine the initial mass function in the substellar regime and to constraint the different brown dwarf formation scenarios, it is mandatory to determine the brown dwarf physical properties, specifically masses. To estimate brown dwarf masses, it is necessary in most cases to constrain the age, as explained in Section 1.2. A proper characterization of a large brown dwarf sample helps to improve atmospheric and evolutionary models and to progress in our knowledge of the physics of these objects.

During this PhD thesis although I did not directly address the problem of determining the substellar initial mass function, I have approached the problem of brown dwarf characterization in three different manners: In Chapter 3 I calculate brown dwarf distances, to obtain luminosities of our objects; in Chapter 4 I study the spectra of young brown dwarfs to constrain ages and in Chapter 5 I look for spectral brown dwarf binaries using spectroscopy and improving our measurement of the fraction of known spectral binaries.

2.1 PARALLAXES OF COOL BROWN DWARFS

Accurate parallax measurements allow us to determine physical properties of brown dwarfs and help us constrain evolutionary and atmospheric models, break age-mass degeneracy, and reveal unresolved binaries.

We measured absolute trigonometric parallaxes and proper motions of six cool brown dwarfs using background galaxies to establish an absolute reference frame. We derived absolute *J*-band magnitudes for these brown dwarfs. The six T brown dwarfs in our sample have spectral types between T2.5 and T8 with photometric distances below 25 pc.

The observations were taken in the *J*-band with the Omega-2000 camera on the 3.5 m telescope at Calar Alto. The reduction of the astrometric measurements was carried out with respect to the field stars. The relative parallax and proper motions were transformed into absolute measurements using the background

galaxies in our fields.

We obtained absolute parallaxes for our six brown dwarfs with a precision between 3 and 6 mas. We compared our results in a color-magnitude diagram with other brown dwarfs with determined parallax and with the BT-Settl 2012 atmospheric models. For four of the six targets, we found a good agreement in luminosity with objects of similar spectral types. We obtained an improved accuracy in the parallaxes and proper motions in comparison to previous works. The object 2MASS J11061197+2754225 is more than 1 mag overluminous in all bands, which point to binarity or high order multiplicity.

2.2 NEW CONSTRAINTS ON THE FORMATION AND SETTLING OF DUST IN THE ATMOSPHERES OF YOUNG M AND L DWARFS

The lower gravity of young brown dwarfs (< 100 Myr) modifies their spectral features. A proper characterization of brown dwarfs is crucial for the identification of the least massive and latest-type objects in star-forming regions, and to explain the origin(s) of the peculiar spectrophotometric properties of young directly imaged extrasolar planets and brown dwarf companions.

We obtained medium-resolution near-infrared spectra of seven young M9.5-L3 dwarfs previously classified at optical wavelengths. We aim to empirically confirm the low surface gravity of the objects in the near-infrared. We also test whether self-consistent atmospheric models correctly represent the formation and the settling of dust clouds in the atmosphere of young late-M and L dwarfs.

We used the Infrared Spectrometer And Array Camera (ISAAC) at the Very Large Telescope (VLT) to obtain the spectra of the targets. We compared the spectra to those of mature and young brown dwarfs, and to young late-type companions to nearby stars with known ages, to identify and study gravity-sensitive features. We computed spectral indices weakly sensitive to the surface gravity to derive near-infrared spectral types. Finally, we found the best fit between each spectrum and synthetic spectra from the BT-Settl 2010 and 2013 atmospheric models. Using the best fit, we derived the atmospheric parameters of the objects and identified which spectral characteristics the models do not reproduce.

We confirmed that our objects were young brown dwarfs and we found near-infrared spectral types in agreement with the ones determined at optical wavelengths. The spectrum of the L2 γ dwarf 2MASSJ232252.99-615127.5 reproduces the spectrum of the planetary mass companion 1RXS J160929.1-210524b well. The BT-Settl models fit the spectra and the 1-5 μm spectral energy distribution of the L0-L3 dwarfs for temperatures between 1600-2000 K. But the models fail to reproduce the shape of the H band and the near-infrared slope of some of our targets. This fact, and the best-fit solutions found with super-solar metallicity, are indicative of a lack of dust, in particular at high altitude, in the cloud models.

The modeling of the vertical mixing and of the grain growth will be revised in the next version of the BT-Settl models. These revisions may suppress the remaining non reproducibilities. Our spectra pro-

vide additional templates for the characterization of the numerous young L-type companions that will be detected in the coming years by planet imaging instruments such as VLT/SPHERE, Gemini/GPI, Subaru/SCExAO, and LBTI/LMIRCam.

2.3 HUNTING FOR BROWN DWARF BINARIES WITH X-SHOOTER

The refinement of the brown dwarf binary fraction may contribute to the understanding of the substellar formation mechanisms. Peculiar brown dwarf spectra or discrepancies between optical and near-infrared spectral type classification of brown dwarfs may indicate unresolved brown dwarf binary systems. We obtained medium-resolution spectra of 22 brown dwarfs that are potential binary candidates in the optical and the near-infrared using the *Wideband ultraviolet-infrared single target spectrograph* (X-Shooter) at the Very Large Telescope (VLT).

We aim to select brown dwarf binary candidates to refine the brown dwarf binary fraction. We also test whether BT-Settl 2014 atmospheric models reproduce the physics in the atmospheres of these objects.

We used different procedures tailored to the various types of expected binaries. To find different spectral type binaries, we used spectral indices and we compared the selected candidates to single spectra and to compositions of two single spectra from libraries, to try to reproduce our X-Shooter spectra. We also created artificial binaries within the same spectral class, and we tried to find them using the same method as for brown dwarf binaries with different spectral types. We compared our spectra to the BT-Settl models 2014. From the best fit of the composite synthetic models to the observed spectra, we derived the atmospheric parameters of the objects and identified which spectral features the models are unable to reproduce.

We selected six possible L plus T brown dwarfs binary candidates. All candidates, except one, are better reproduced by a combination of two single brown dwarf spectra than by a single spectrum. The one-sided F-test discarded this object as a binary candidate. We found that we are not able to find the artificial binaries with components of the same spectral type using the same method used for L plus T brown dwarfs.

We conclude that the combination of L plus L or T plus T spectra cannot be found using the same method used for L plus T brown dwarf binaries. To find equal spectral type binaries, parallaxes, radial velocity measurements or high resolution imaging are needed. BT-Settl models 2014 are able to reproduce the majority of the SEDs from our objects in the optical and in the near infrared. Nonetheless, these models do not reproduce the shape of the H-band, maybe because FeH and CH₄ opacities are incomplete in BT-Settl models. Best matches to models give a range of effective temperatures between 950 K and 1900 K, and a range of gravities between 4.0 and 5.5. Some best matches correspond to supersolar metallicity.

PARALLAX MEASUREMENTS OF COOL BROWN DWARFS*

3.1 INTRODUCTION

Accurate measurements of distances allow us to determine physical properties of brown dwarfs, including luminosities or absolute fluxes to check atmospheric models, temperatures, space motions, and space densities.

Our goal is to derive parallaxes with a high accuracy (5-10%), we constrained our sample to objects with photometric distances up to 25 pc. Our sample of objects is located at spectrophotometric distances of 10–25 pc with magnitudes in J between 13.9 and 18.0, which are suitable for astrometry.

Since the first parallax programs for brown dwarfs began with Dahn et al. (2002a), Vrba et al. (2004a), and Tinney et al. (2003), the relationship between the color and magnitude of BDs has been studied (Burgasser et al. 2008; Schilbach et al. 2009; Marocco et al. 2010; Faherty et al. 2012a; Dupuy & Liu 2012b) among others. One of the most significant results of these studies is the large dispersion in luminosity for objects with similar spectral types (Faherty et al. 2012a), which shows the importance of other factors, such as gravity, metallicity, sedimentation, and binarity (Tsuji et al. 1996; Burrows et al. 2006; Saumon & Marley 2008). Increasing the number of cool brown dwarfs with accurate distance measurements allows us to understand the variation in the color magnitude and H-R diagrams, as we can determine the luminosity more accurately. Also, the J -band bump in the color-magnitude diagram, a brightening observed in the J band for brown dwarfs with spectral types between T1 and T5, is not well understood (Burgasser et al. 2002a, Tinney et al. 2003 and Vrba et al. 2004a). There are still few objects with parallaxes in the L/T transition, which prevent the progress of understanding brown dwarf evolution.

In this chapter, we report the absolute parallaxes and the absolute proper motions of six T ultra cool dwarfs with spectral types between T2.5 and T8 and spectrophotometric distances between 10–25 pc.

*This chapter is adapted from the paper: Manjavacas, E.; Goldman, B.; Reffert, S.; Henning, T., 2013, *Astronomy & Astrophysics*. Vol. 560, pp. 52

Table 3.1: This table gives the sample of objects with their spectral types, photometry and references for our targets.

Name	SpT	J [mag]	H [mag]	K_s [mag]	ref.obj.	exS	epochs	Ref.
2MASS J11061197+2754225	T2.5 (1)	14.96±0.04	14.20±0.05	13.84±0.05	96	49	10	(1)
ULAS J130217.21+130851.2	T8 (5)	18.11±0.04	18.60±0.06	18.28±0.03	247	68	12	(2)
ULAS J141756.22+133045.8	T5.5 (3)	16.77±0.01	17.00±0.03	17.00±0.04	77	99	10	(3)
2MASS J22541892+3123498	T4 (4)	15.32±0.05	15.06±0.08	14.99±0.15	644	125	10	(4)
ULAS J232035.28+144829.8	T6 (6)	16.79±0.02	17.14±0.04	17.40±0.03	298	46	12	(3)
ULAS J232123.79+135454.9	T7.5 (2)	16.69±0.03	17.09±0.06	17.36±0.10	278	73	11	(3)

(1) Looper et al. (2007); (2) Burningham et al. (2010); (3) Scholz (2010); (4) Burgasser et al. (2002b); (5) Cushing et al. (2011); (6) Murray et al. (2011)

In Section 3.2, we explain how our selection criteria are used to select our targets and how the observations were carried out. In Section 3.3, we describe the data reduction: how the astrometry was performed, the estimation of the differential chromatic refraction (DCR), and the calculation of the relative and absolute parallax and proper motions. In Section 3.4, we compare our results to those of other previous studies, which included our object. Finally, we present our conclusions in Section 5.8.

3.2 OBSERVATIONS

Initially, we selected eight T dwarfs with expected spectrophotometric distances smaller than 25 pc. Spectrophotometric distances of our targets were estimated using the relation given by Goldman et al. (2010). Only objects brighter than 18 mag in the J band were selected, so that good signal-to-noise (S/N) observations could be obtained in a reasonable amount of time. Two targets were discarded later from the list, since they were located in fields with bright stars nearby, which compromised the accuracy of the astrometry. Finally, all the targets had to be observable most part of the year to have a better coverage of the parallax ellipse. In Table 1, we present an overview of our targets, which provide spectral types and derived JHK photometry in the MKO (Mauna Kea Observatories) system (Stephens & Leggett 2004) for targets with 2MASS photometry. For the rest, we provide UKIDSS (UKIRT Infrared Deep Sky Survey) photometry, which is similar to MKO (Hewett et al. 2006). For the target ULAS J232035.28+144829.8, we provide the photometry from Murray et al. (2011), which is also similar to MKO. In the last column, we add references to the discovery papers.

Images were taken with the near-IR camera Omega-2000 on the 3.5 m telescope at Calar Alto in J band. Omega-2000 is a prime-focus, near-IR camera with a wide field that uses a 2k x 2k focal plane array with sensitivity from the z band to the K band. The camera provides a 15.4' x 15.4' field of view with a resolution of 0.45"/pixel. The wide field of Omega-2000 allows us to convert from relative parallaxes and proper motions to absolute values using galaxies (between 50 and 130 galaxies in each field). The

astrometric observations were taken in service mode in the J band. In all the cases, 15 single frames with exposure times of 60s were taken with dithering.

Our observations have been taken between March 2011 and June 2013 in 24 epochs. The baseline varies from 23 to 27 months. In the case of the object ULAS J232035.28+144829.8, we also used one observation, which was taken in July 2009 with Omega-2000 in the methane filter; therefore, the baseline for this object is almost four years. The average seeing on Calar Alto during our observations was around 1.0". We typically observed at 1-2 hr from the meridian, so that DCR might be significant (Stone 1996, Pravdo & Shaklan 1996). Further details about the estimation of the DCR corrections are given in Section 3.3.2.

Dark frames and sky flats were taken every evening, and the bad pixel mask was derived from the dark current analysis by an appropriate cut in the goodness-of-fit of the linear relation between dark current and exposure time. The fifteen individual raw images were corrected using flats, darks and bad pixels mask frames. To perform the reduction of the raw images, we used the MPIA Omega-2000 pipeline, which runs under MIDAS. The outputs are single, calibrated images for each epoch. Before performing the analysis of our images, we stacked the fifteen single exposures to get a better S/N. The stacking process was carried out using the algorithm explained in Mutchler & Fruchter (1997) and Fruchter & Hook (2002). The single images are slightly shifted, so they must be previously aligned. These images are aligned in a world coordinate system, so that corresponding astronomical objects are stacked on top of each other. A median image of the shifted frames is extracted. Since the images were shifted with different offsets, only the central area overlaps for all frames. The outer regions, where individual images do not contribute are marked and left blank. To check if the stacking actually improved the final value for the parallax and proper motions, we repeated the analysis using the fifteen single frames and the result obtained was less accurate than using stacked images. Therefore, we used the stacked frames for the final analysis.

3.3 ANALYSIS

3.3.1 ASTROMETRY

We obtained positional measurements for all of the sources in each field from SExtractor (Bertin & Arnouts 1996) using the parameter XWIN_IMAGE. SExtractor determines the background and identifies whether pixels belong to background or to objects. The program splits up the area that is not background into separate objects and determines the properties of each object. The output from SExtractor is a catalog for each epoch and field that contains all the objects in each field, the positions with error, instrumental magnitudes and errors, instrumental fluxes and errors, and star/galaxy classification among other parameters. The errors in position provided by SExtractor are estimated using photon statistics. This estimate is considered to be a lower value of the real error.

The next step to create an astrometric catalog with the objects in our fields was to associate the detections in the multiple epochs that belonged to a common set of objects. For that, we cross-identified stars and we

matched detections in a given frame to an astrometric reference catalog. As the telescope did not provide WCS information in the image headers, we used the software from www.astrometry.net (Lang et al. 2010) to perform a preliminary astrometry. The reference catalog used is the USNO-B1.0 catalog (Monet et al. 2003). This preliminary astrometry cannot be better than the accuracy of the catalog, which is around 200 mas. Then, we refined the initial guess using the software SCAMP (Bertin 2006) by choosing the first stacked image of the first epoch for each target as reference catalog. The reference objects used to perform the astrometry were distributed uniformly in the fields. These fields contained between 70 and 650 references. A different weight was given to the high S/N reference objects and the small S/N reference objects.

We constructed the catalog of associated detections by starting with the list of detections in the first stacked image on the first epoch, and then adding detections from the next epoch by finding matches between the objects in the catalogs. We performed the match of the catalogs using the IRAF routine `tables.ttools.tmatch`. This routine deletes the objects, which are not detected in all the epochs, but mainly faint targets and stars at the edges of the fields. We used a search radius of 1'' around the object from the reference catalog.

3.3.2 DCR CORRECTION

The DCR effect results in astrometric shifts of the centroids (in any single-band imaging survey) because of the dependence of the refractive index of air on the wavelength. The reference objects and the targets have a different flux distribution in the *J* band because they have different spectral types. Thus, their positions shift relative to one another due to different amounts of atmospheric refraction. Therefore, the DCR is a potential source of astrometric error, and it must be estimated.

In our case, the observations were typically performed between 1 and 2 hr from the meridian. To estimate the magnitude of the resulting DCR for the field stars and the targets, we used the formula according to Monet et al. (1992), Stone (1996), Pravdo & Shaklan (1996), and Kaczmarczik et al. (2009). We calculated the DCR effect for the targets relative to the typical field stars (M dwarfs). The correction due to DCR was typically 1 mas for the relative position between target and field stars. Since our typical parallax errors are of the order of 3-6 mas (see Section 3.3.3.2), it was not necessary to take the DCR into account. We also checked the influence of an epoch taken far from the meridian in the final result for the parallax. The conclusion was that the final parallax value did not change significantly. We discuss other astrometric error sources in detail in Section 3.3.4.

3.3.3 PARALLAXES

3.3.3.1 RELATIVE PARALLAXES

For the target and each object in the field, we use the positions in each epoch with their errors as an input to a χ^2 fit. Errors used for the fitting are the residuals in right ascension and declination, respectively, and have been determined iteratively. These errors include all the error sources explained in Section 3.3.4. We fit the positions (α_0 and δ_0), proper motions (μ_α and μ_δ), and the parallax (π). Each fit to $2 \times N_{epochs}$ measurements had $2 \times N_{epochs} - 5$ degrees of freedom. It is important to note that this parallax is a relative parallax, which uses field objects in the field of the target as references.

The apparent trajectory of each object in the field was then fitted to an astrometric model:

$$\Delta\alpha(t) = \mu_\alpha(t - t_0) + \pi \cdot (p_\alpha(t) - p_\alpha(t_0)) \quad (3.1)$$

$$\Delta\delta(t) = \mu_\delta(t - t_0) + \pi \cdot (p_\delta(t) - p_\delta(t_0)), \quad (3.2)$$

where $\Delta\alpha(t)$ and $\Delta\delta(t)$ are the positional offsets with respect to the first epoch of observation at t_0 ; t is the time; μ_α and μ_δ are the proper motion in RA and DEC, π is the parallax; and p_α and p_δ are the parallax factors in RA and DEC, respectively.

The parallax factors were computed using the Earth geocenter as obtained from the JPL DE405 solar system ephemeris. This model is based on the methods in the *Hipparcos* (Perryman 1997) and *Tycho* Catalogues (Hog et al. 2000).

We present the plots of the stellar paths obtained using Equations 3.1 and 3.2 in the appendix.

3.3.3.2 CORRECTION FROM RELATIVE TO ABSOLUTE PARALLAX

As mentioned before, the parallaxes from the astrometric solution are relative to the position of the background objects chosen as references. In general, these objects were field objects that may have their own parallaxes and proper motions, so that a correction is based upon the true parallaxes of the reference objects to convert to an absolute measurement. The field objects used as references are weighted depending on their S/N, giving more weight to the objects with better S/N. Given the large field of view of Omega-2000 (15.4' x 15.4'), we can find a sufficient number of extragalactic sources in all our fields. To derive the absolute parallax from the relative parallax, we used the extragalactic sources (exS) that we found in the fields of our targets. We searched for the extragalactic sources by setting the keyword CLASS_STAR

in SExtractor. This software classifies extragalactic sources and stars in a field using neural networks, as explained in Bertin & Arnouts (1996) by applying a method called *backpropagation*. Afterward, we determined the relative parallaxes of all the objects that were classified as extragalactic sources. We made a histogram of parallaxes and proper motions of these sources. As we could detect plenty of outliers in the histograms, we removed the objects with parallaxes or proper motions that were further than $3\text{-}\sigma$ away from the median in parallaxes or proper motions. We fitted a Gaussian function to the histogram of the parallaxes after deleting these outliers. Finally, the relative parallax for the extragalactic sources (π_{exS}) is the mean of the fitted Gaussian, and the error of this parallax is the error in the mean for the Gaussian fitted to our data.

We correct the relative parallax to the absolute parallax as follows: $\pi_{abs} = \pi_{rel} - \pi_{exS}$, where π_{abs} is the absolute parallax for the object, π_{rel} is the relative parallax of the object, and π_{exS} is derived as described above.

We execute a similar procedure to calculate the absolute proper motions given in Table 3.2.

3.3.4 ABSOLUTE PARALLAX ACCURACY

We have several error sources, which arise at different phases in our analysis:

- Centroid errors. These errors are calculated by SExtractor using an iterative method. The positional uncertainties due to image centroiding in the relative position of the target is on average ~ 1.5 mas.
- Atmospheric image motions. Atmospheric effects also limit the precision of the astrometry in several different ways, such as intensity scintillation, image blurring, image motion and speckle structure. We estimated this effect using the expression given in Lindegren (1980): $\epsilon^2 \simeq 0.71R^{2/3}T^{-1}$ under the condition: $14T \gg 4300R \gg d$. The parameter T is the integration time in seconds (60 s x 15 single images), R is the diameter of the field in radians ($4.5 * 10^{-3}$ rad) and d is the diameter of the telescope in meters (3.5 m). The variance for the atmospheric image motion is estimated to be 5 mas per epoch.
- DCR effect. This error was calculated as explained in Section 3.3.2, and it is typically 1 mas per epoch.
- Plate solution. Distortions are introduced by the instrument because it is not sufficiently stable, as it is dismantled between two epochs. The program SCAMP calculates the best astrometric solution performing a χ^2 minimization and calculates the distortions using the relative positions of the reference objects between the reference catalog and the catalogs of all epochs. The value of the residual distortion is between 5 and 10 mas for bright stars per epoch. The distortions due to the images stacking are negligible. We measure up to 0.04% distortions or 0.5 pixel distortions from center to corner (Bailer-Jones et al. 2000).

- Error in the conversion from relative to absolute parallaxes. It is calculated Section 3.3.3.2. The typical value of these uncertainties is ~ 1.5 mas.

3.4 RESULTS

The astrometric and photometric results for the six objects are compiled in Table 3.2. Column 1 contains the object’s name. Columns 2 and 3 give the derived absolute proper motions in right ascension (μ_α) and declination (μ_δ) for the targets; column 4 gives the relative parallax (π_{rel}). In column 5, we provide the absolute parallax (π_{abs}). Column 6 contains the derived distance (d) from the absolute parallax results. Column 7 provides the photometric distance (d_{phot}) in pc, using the relation published in Goldman et al. (2010), and column 8 contains the values for χ^2 and N_{dof} , which is the number of degrees of freedom.

To characterize our targets, we plot them in a color-magnitude diagram (CMD) with the 177 L, L-T, and T brown dwarfs published by Dupuy & Liu (2012b) with magnitudes in the MKO system. Our magnitudes were originally in the 2MASS photometric system, so that we use the relation published in Stephens & Leggett (2004) to transform between the 2MASS photometric system and the MKO system. The rest of the targets have UKIDSS photometry, which is similar to the MKO photometry (Hewett et al. 2006). For the target ULAS 2320+1448 we provide the photometry from Murray et al. (2011), also similar to MKO. We plot ($J - H$, M_J) and ($J - K$, M_J) and ($W1 - W2$, M_w1) using WISE photometry.

We overplot our CMD with the BT-Settl models by Allard et al. (2012b). The color-magnitude diagrams are shown in Figure 3.1 with overplotted isochrones from Allard et al. (2012b). We show the stellar paths for all the objects in the Appendix.

3.5 DISCUSSION

3.5.1 2MASS J11061197+2754225

This object was discovered by Looper et al. (2007). It was identified using a near infrared (NIR) proper-motion survey based on multi-epoch data from the Two Micron All Sky Survey (2MASS). It was classified as a T2.5 BD using the IRTF SpeX spectrograph in low-resolution mode with a resolution of $R \sim 150$. Looper et al. (2007) estimated the spectrophotometric distance as 15.5 ± 1.2 pc, which was calculated using the spectral types that were derived in the same article and by using the Liu et al. (2006) spectral type versus magnitude relation without known binaries. Burgasser et al. (2010) proposed this target to be a strong binary candidate in a $T0.0 \pm 0.2$ and $T4.5 \pm 0.2$ system, although Looper et al. (2008a) performed high angular resolution imaging with NIRC2/Keck II, finding only one source.

The location of the object in Figures 3.1 and 3.3 seem to give a luminosity inconsistent with the classifi-

cation provided before (Looper et al. 2007; Kirkpatrick et al. 2010) by using indices in the NIR. Looper et al. (2007) mentions that J1106+27 is distinctly ($> 1-\sigma$) bluer in the z-J band in SDSS than all the T2 brown dwarfs in their sample. In our CMD (see Fig. 3.1 and 3.3), the object is also overluminous by ~ 1 mag. Due to its overluminosity, this object is a good candidate for a binary system or even high order multiplicity, although this issue should be studied in more detail using high resolution images or high resolution spectroscopy. The spectroscopic distance provided by Looper et al. (2007) is not compatible with the distance derived from the trigonometric absolute parallax within the error bars. The calculated distance is $20.6^{+1.0}_{-1.2}$ pc.

3.5.2 ULAS J130217.21+130851.2

This object was discovered by Burningham et al. (2010), and it was classified as a T8.5 BD by using NIRI on the Gemini North Telescope and IRCS on the Subaru telescope on Mauna Kea, Hawaii. The spectral classification was based on the spectral indices given by Burgasser et al. (2006). The object ULAS J1302+13 was later re-typed as T8 by Cushing et al. (2011).

With regard to Fig. 3.1 and 3.3, this object is not overluminous. The value of the distance has been calculated for the first time and is $15.4^{+1.1}_{-1.4}$ pc.

3.5.3 ULAS J141756.22+133045.8

The discovery of ULAS J141756.22+133045.8 was first published by Scholz (2010). It was classified as $T5.5 \pm 1.0$ BD and based on colors and absolute magnitudes from UKIDSS and SDSS. The absolute proper motions were also estimated, using UKIDSS and SDSS data with a baseline of five years, but only with three different epochs.

The result supplied in Scholz (2010) for the absolute proper motions were $\mu_\alpha \cos \delta = -76 \pm 3$ mas/yr and $\mu_\delta = 77 \pm 3$ mas/yr. Scholz (2010) pointed out that the formal errors were very small and were due to the few number of epochs and so that the errors could be unrealistic. The estimated errors by Scholz (2010) were 24 mas/yr, which was the scatter of their data around the best fit to the model.

Burningham et al. (2013) presented YJHK spectroscopy for this object using the Gemini Near Infrared Spectrograph (GNIRS) and derived a type a spectral type of $T5 \pm 0.5$.

Comparing the results from Scholz (2010) for the proper motions with our results and taking the errors into account, the results are compatible. With regard to Fig. 3.3, we can conclude that this object is slightly overluminous in WISE by around 0.2 mag. In Fig. 3.1, this overluminosity is not that clear, although the object is at the edge of the bulk of objects. Our result for the distance is $30.3^{+2.5}_{-3.8}$ pc.

3.5.4 2MASS J22541892+3123498

The object 2MASS J22541892+3123498 was first published as a brown dwarf by Burgasser et al. (2002b). It was classified as a T5V BD by using spectral observations in NIR with $R \sim 1200$ and by calculating the spectral indices, as explained in Burgasser et al. (2002b). Afterward, the spectral type was recalculated using the criteria given in Burgasser et al. (2003) as a standard T4 BD (Burgasser et al. 2004, 2006). The proper motions were also estimated by Jameson et al. (2008) using WFCAM at UKIRT from February to August 2006. Their result for the proper motions was $\mu_\alpha \cos \delta = 68 \pm 15$ mas/yr and $\mu_\delta = 200 \pm 11$ mas/yr.

Our results for the proper motions agree with the result given by Jameson et al. (2008) within the error bars. This object is not overluminous. The provided distance is $13.9^{+0.5}_{-0.6}$ pc, and it has been calculated for the first time.

3.5.5 ULAS J232035.28+144829.8

The discovery of this object was first published by Burningham et al. (2010), and it was classified as a T5 spectral type using medium resolution spectroscopy. In Scholz (2010), the object is classified as $T7.0 \pm 2.0$ using colors from UKIDSS and SDSS. In Murray et al. (2011), the spectral indices were recalculated, using data from NIRI on the Gemini-North telescope with a spectral resolution of $R \sim 460$; the new classification is $T6 \pm 1$.

In Scholz (2010), the proper motions were given as $\mu_\alpha \cos \delta = 387 \pm 5$ mas/yr and $\mu_\delta = 121 \pm 2$ mas/yr. These proper motions were calculated with a baseline of seven years; nevertheless, there were only three epochs in total, and two of them very close to each other. The estimated error in Scholz (2010) due to the scatter around the best fit to the model was 11 mas/yr.

In Murray et al. (2011), the proper motions and the distance were also estimated performing a photometric follow-up using UKIDSS, by obtaining proper motions of $\mu_\alpha \cos \delta = 399 \pm 26$ mas/yr, $\mu_\delta = 122 \pm 26$ mas/yr, and distance of 24 ± 5 pc.

The proper motions, which we obtained, agree to the values provided by Scholz (2010) and Murray et al. (2011) within the error bars, but our values are more precise. We also agree with Murray et al. (2011) on the distance to within the error bars. This object is not overluminous (see Fig. 3.1 and 3.3). The calculated distance is $21.1^{+1.6}_{-2.2}$ pc.

3.5.6 ULAS J232123.79+135454.9

The brown dwarf discovery of ULAS J232123.79+135454.9 was first published by Scholz (2010). It was classified with a spectral type of $T7.5 \pm 1.5$ using UKIDSS and SDSS colors. This object was also classified in Burningham et al. (2010) as a T7.5 using medium resolution spectroscopy.

Table 3.2: Summary of the results.

Object	μ_α (mas/yr)	μ_δ (mas/yr)	π_{rel} (mas)	π_{abs} (mas)	d (pc)	d_{phot} (pc)	χ^2/N_{dof}
2M J1106+2754	-311 ± 4	-438 ± 5	46 ± 3	48 ± 3	$20.6^{+1.0}_{-1.2}$	12.5 ± 1.4	21.8/17
ULAS J1302+1308	-445 ± 6	5 ± 7	67 ± 5	65 ± 5	$15.4^{+1.1}_{-1.4}$	16.1 ± 2.3	25.4/19
ULAS J1417+1330	-121 ± 4	50 ± 3	32 ± 3	33 ± 3	$30.3^{+2.5}_{-3.8}$	23.8 ± 5.1	23.0/17
2M J2254+3123	67 ± 3	187 ± 7	71 ± 2	72 ± 3	$13.9^{+0.5}_{-0.6}$	14.7 ± 1.9	23.4/17
ULAS J2320+1448	410 ± 4	121 ± 3	47 ± 3	47 ± 4	$21.1^{+1.6}_{-2.2}$	20.7 ± 3.6	22.6/19
ULAS J2321+1354	76 ± 4	-576 ± 6	83 ± 3	84 ± 4	$11.8^{+0.5}_{-0.6}$	10.8 ± 0.7	22.2/19

Scholz (2010) also provided the proper motions using SDSS and UKIDSS with a baseline of seven years and four epochs taken along this baseline. The proper motions were given as $\mu_\alpha \cos \delta = 56 \pm 15$ mas/yr and $\mu_\delta = -577 \pm 10$ mas/yr with an estimated error of 10 mas/yr due to the scatter of the data around the fit to the best model. Kirkpatrick et al. (2012) provided a distance limit of approximately 20 pc.

The object ULAS J232123.79+135454.9 is not overluminous (see Fig. 3.1 and 3.3). We agree with Scholz (2010) on the result for the proper motion within the error bars. Kirkpatrick et al. (2012) adopted a distance of 14.1 pc. Our result for the distance is $11.8^{+0.5}_{-0.6}$ pc.

3.6 CONCLUSIONS

We have measured the trigonometric parallaxes of six T brown dwarfs for the first time with spectral types between T2.5 and T7.5.

We compare our results to the spectrophotometric distance given by Goldman et al. (2010) and to the results of the spectrophotometric distance and proper motions provided in other studies such as Scholz (2010), Looper et al. (2007) and Kirkpatrick et al. (2012) among others. Our results generally agree well with other studies, but they are more precise.

We also compare the locations of our targets in (J-H, M_J) and (J-K, M_J) CMDs to those of the objects by Dupuy & Liu (2012b) and to the evolutionary tracks by Allard et al. (2012b).

Four of our six targets are not overluminous. Nevertheless, the object ULAS J141756.22+133045.8 is slightly overluminous in the WISE CMD. It has an absolute magnitude in W1, which is around 0.2 mag brighter than the objects with the same spectral types. Its overluminosity is not seen in the CMDs in MKO photometry. The object 2MASS J11061197+2754225 is more than 1 mag overluminous in all the bands, pointing to binarity or even higher multiplicity. To confirm these results, high resolution imaging and high resolution spectroscopy is needed.

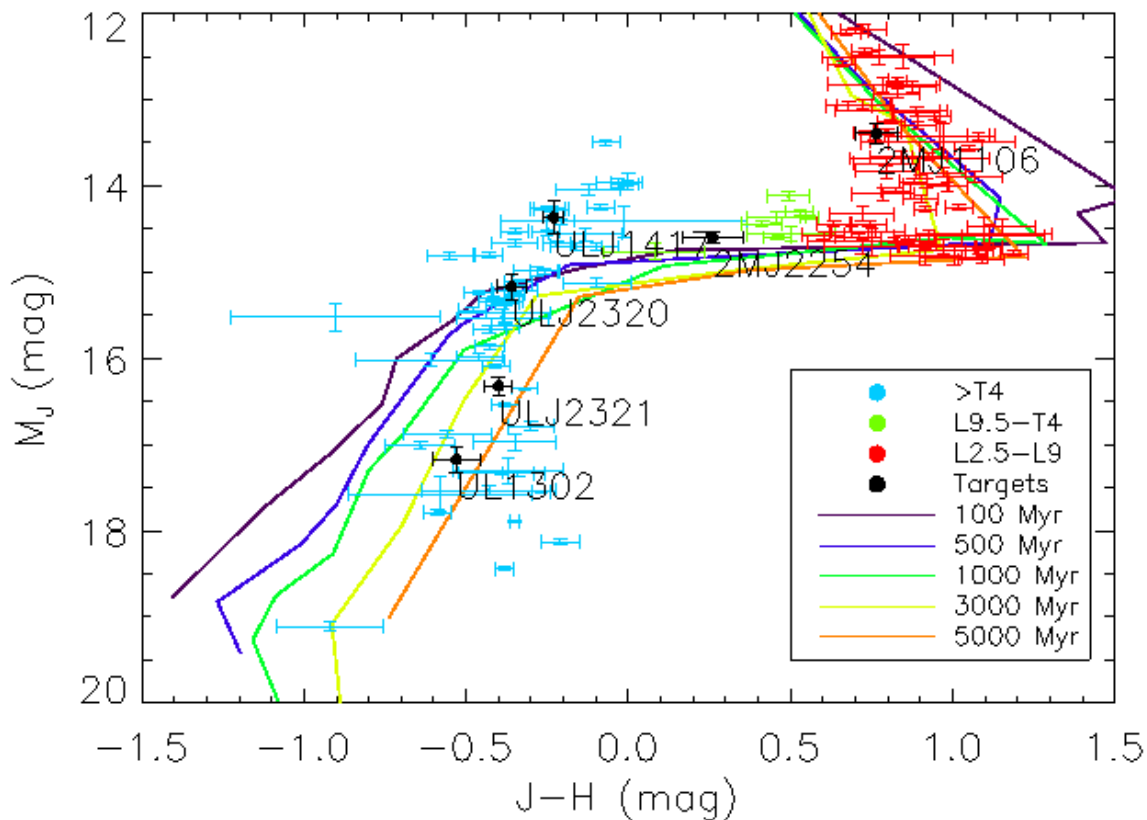


Figure 3.1: Color-magnitude diagram in the MKO system showing the brown dwarf sample from Dupuy & Liu (2012b) (except M-type brown dwarfs), our targets and the BT Settl-models (Allard et al. 2012b). The objects in the Dupuy & Liu (2012b) sample with spectral type between L2.5-L9 are shown in red; the objects with spectral types between L9.5 and T4 are shown in green; and the objects with spectral type $>T4$ are shown in light blue. Our targets, which are listed in Table 3.1, are shown in black. We overplot the evolutionary models from Allard et al. (2012b) in MKO photometry for different ages from 100 Myr to 5000 Myr.

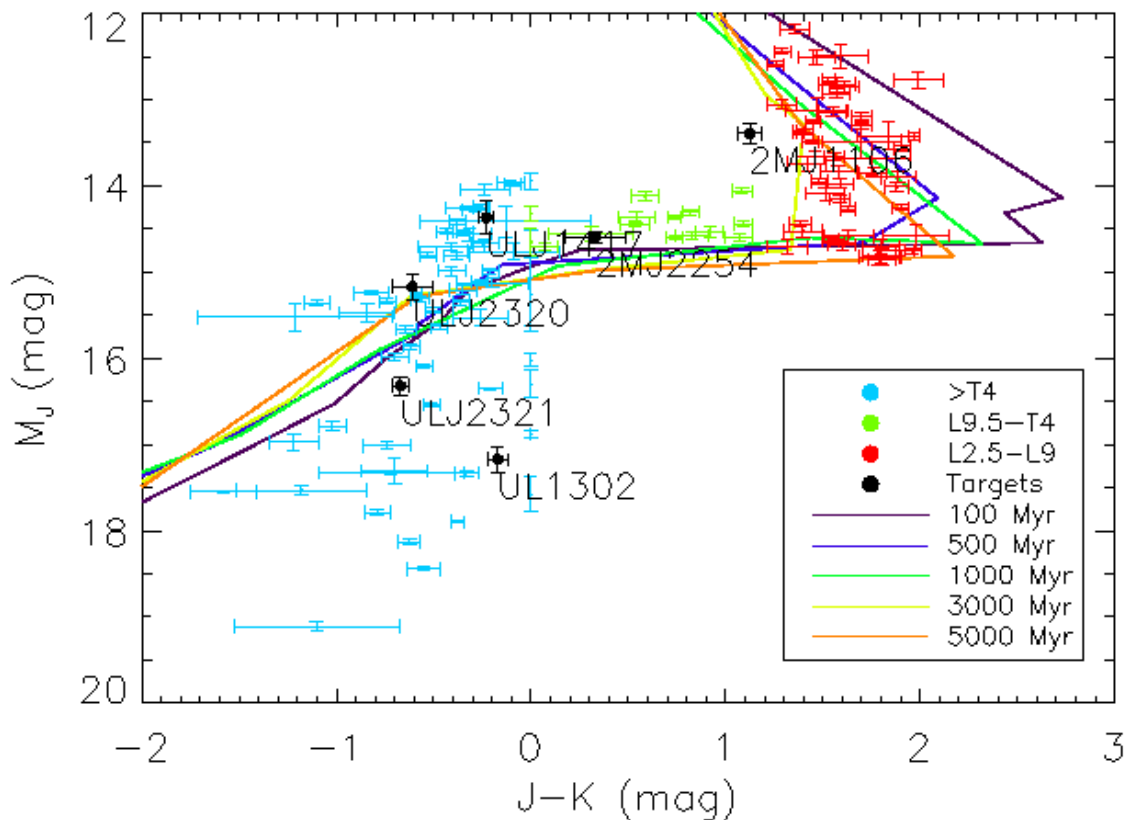


Figure 3.2: Color-magnitude diagram in the MKO system showing the brown dwarf sample from Dupuy & Liu (2012b) (except M-type brown dwarfs), our targets and the BT Settl-models (Allard et al. 2012b). The objects in the Dupuy & Liu (2012b) sample with spectral type between L2.5-L9 are shown in red; the objects with spectral types between L9.5 and T4 are shown in green; and the objects with spectral type $>T4$ are shown in light blue. Our targets, which are listed in Table 3.1, are shown in black. We overplot the evolutionary models from Allard et al. (2012b) in MKO photometry for different ages from 100 Myr to 5000 Myr.

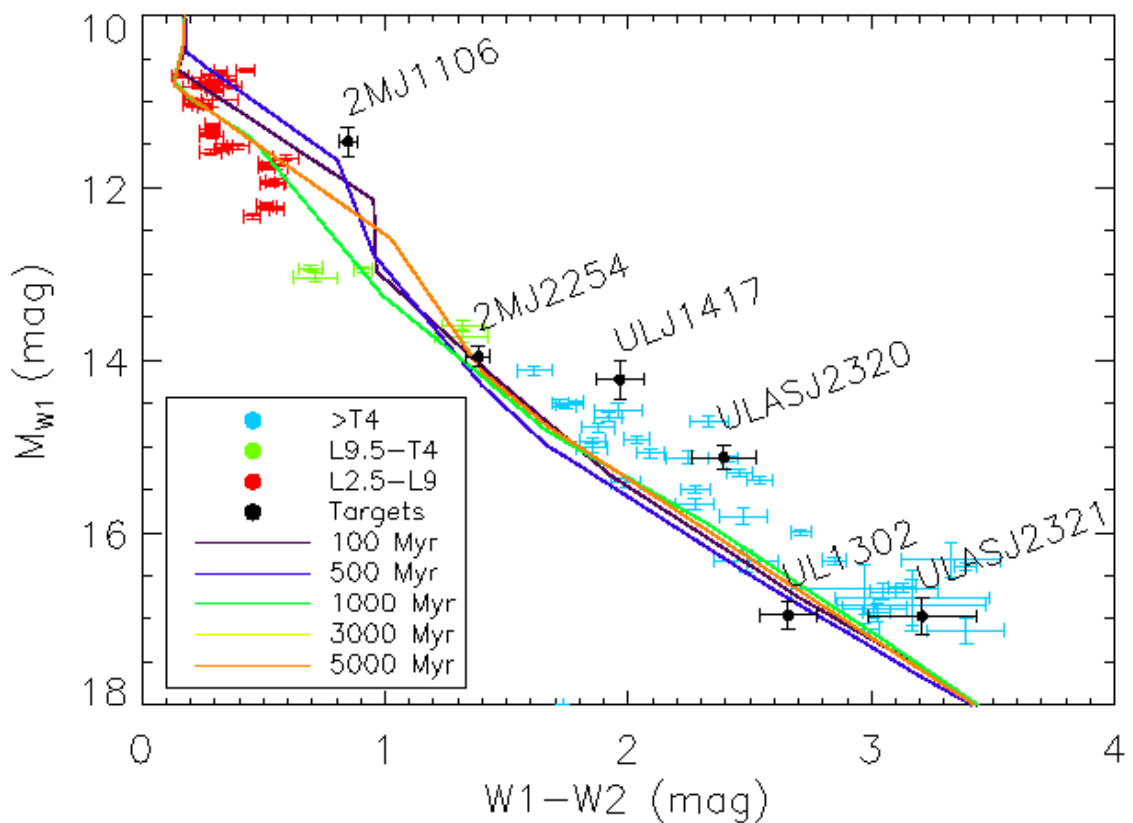


Figure 3.3: Color-magnitude diagram in WISE photometry with $W1-W2$ color vs M_{W1} (WISE). We plot the objects from Dupuy & Liu (2012b) with WISE photometry. L2.5-L9 brown dwarfs are colored in red; objects with spectral types between L9.5 and T4 are green; and objects with spectral type $>T4$ are colored in light blue. Our targets are plotted in black. We overplot the evolutionary models from Allard et al. (2012b) in WISE photometry for different ages, from 100 Myr to 5000 Myr.

3.A STELLAR PATHS OF THE TARGETS

We include the stellar paths, which represent the change in right ascension (RA) and declination (DEC) in time for our targets in this Appendix.

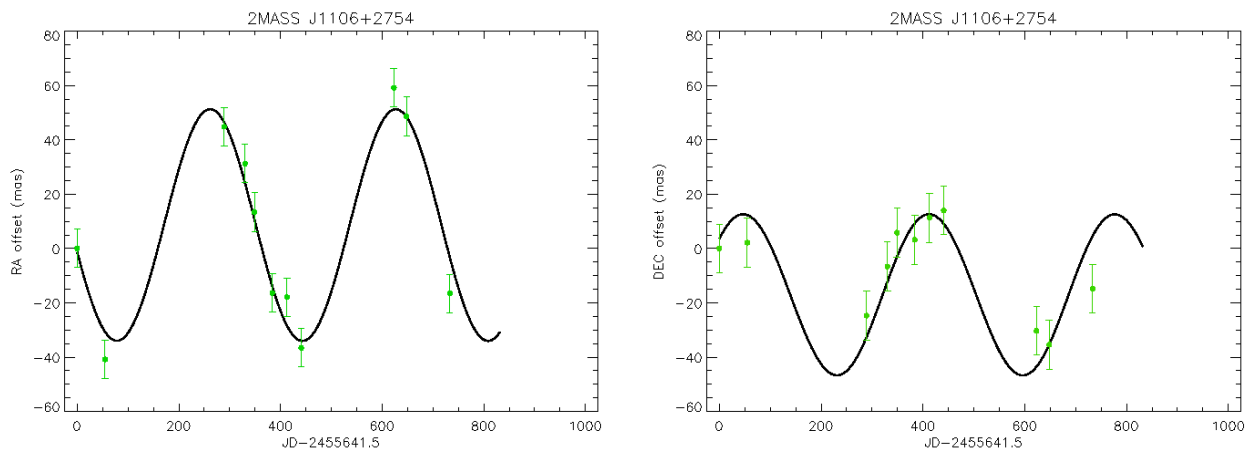


Figure 3.4: Stellar paths for the object 2MASS J11061197+2754225.

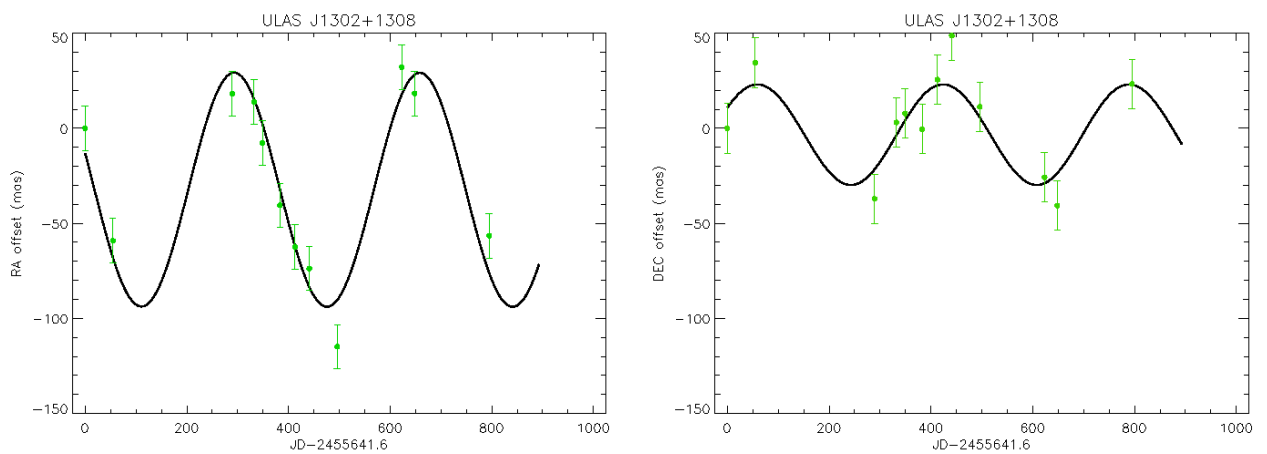


Figure 3.5: Stellar paths for the object ULAS J130217.2+130851.2.

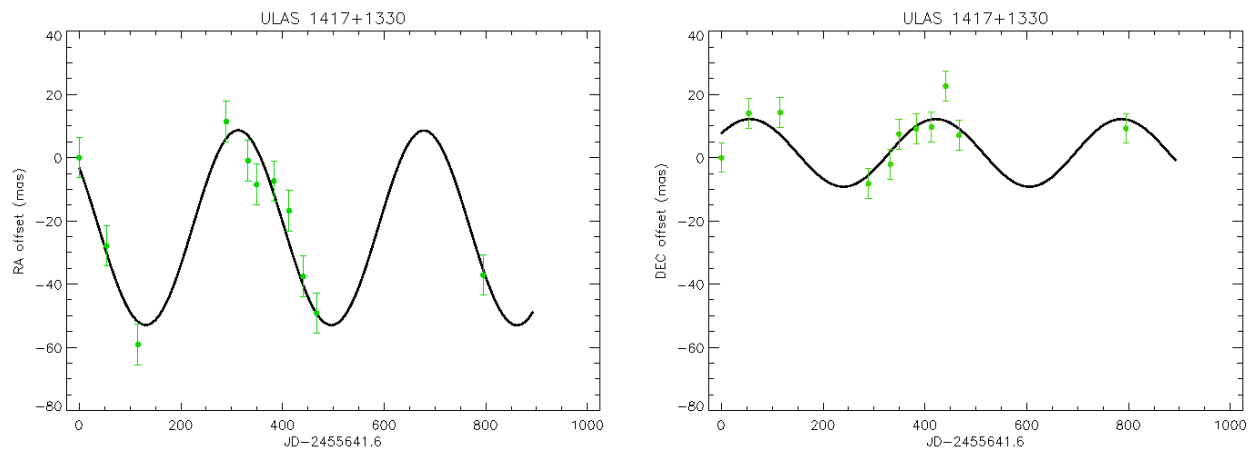


Figure 3.6: Stellar paths for the object ULAS J141756.22+133045.8.

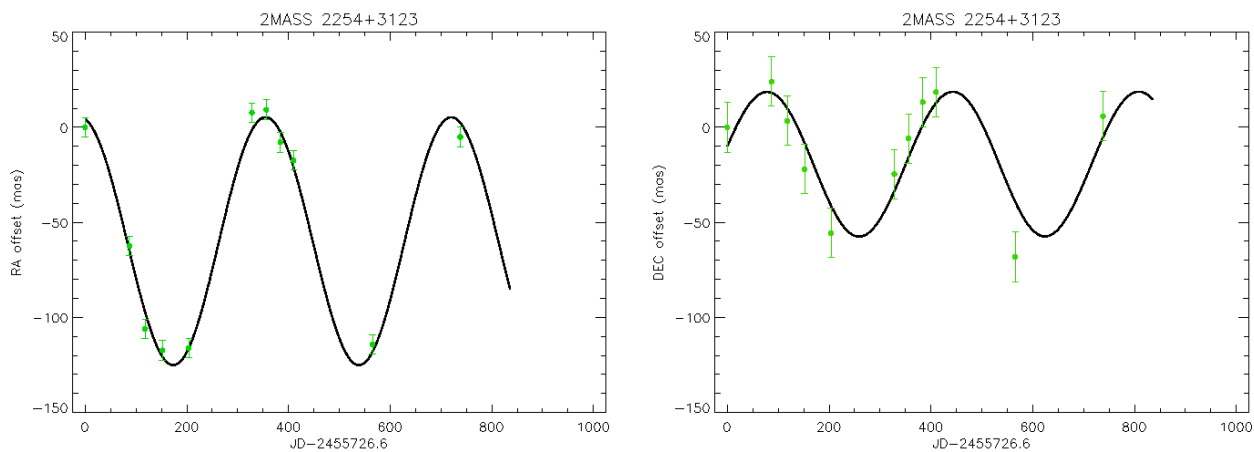


Figure 3.7: Stellar paths for the object 2MASS J22541892+3123498.

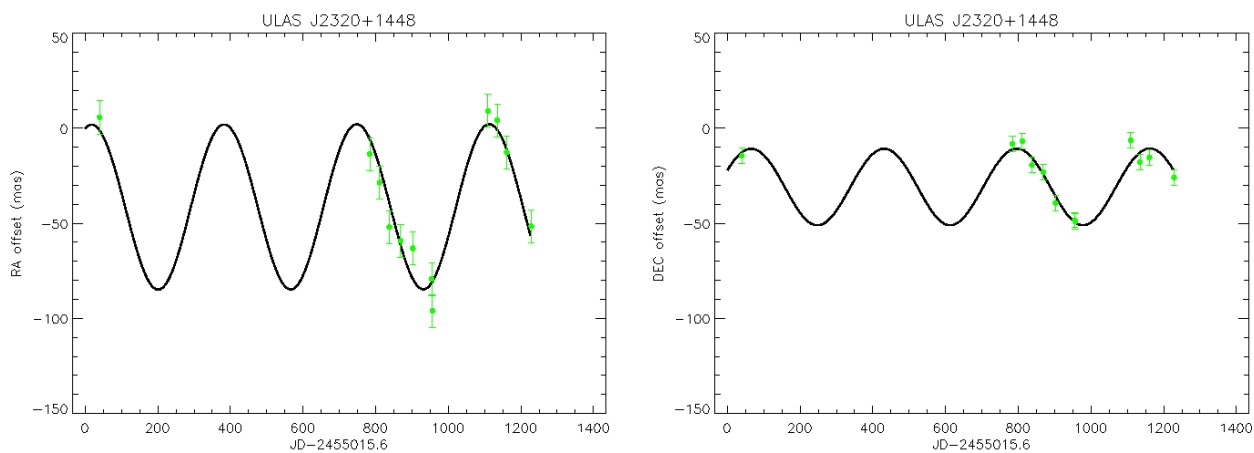


Figure 3.8: Stellar paths for the object ULAS J232035.28+144829.8. The first epoch is an archival Omega-2000 observation.

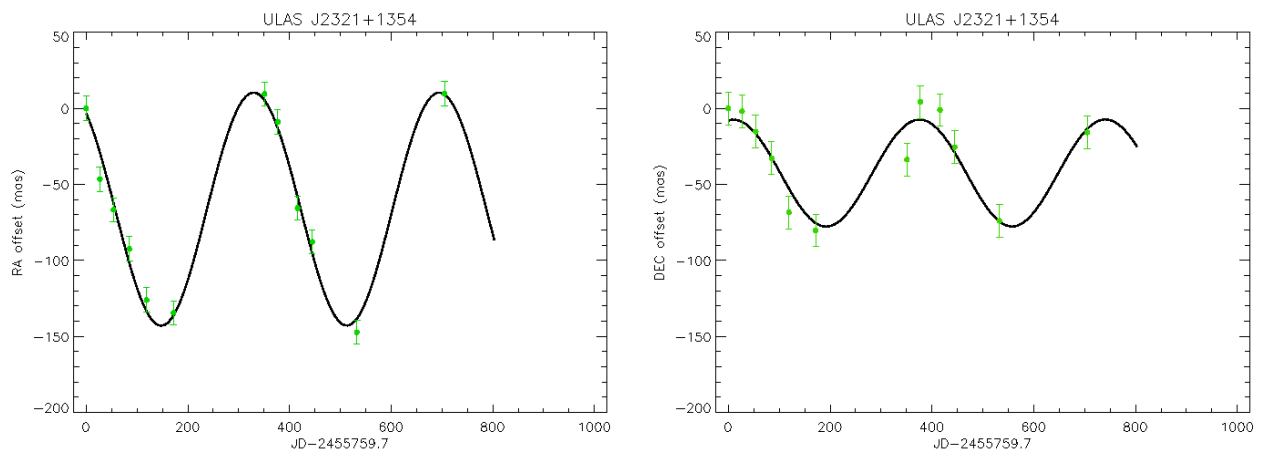


Figure 3.9: Stellar paths for the object ULAS J232123.7+1354454.

NEW CONSTRAINTS ON THE FORMATION AND SETTLING OF DUST IN THE ATMOSPHERES OF YOUNG M AND L DWARFS*

4.1 INTRODUCTION

Brown dwarfs contract and cool down with time (Burrows et al. 1997b; Baraffe et al. 1998b). Therefore, young brown dwarfs can have larger radii and higher luminosities than older and more massive brown dwarfs despite an identical effective temperature. The lower surface gravity of young objects ($g \propto M/R^2$) can be directly accessed by observation and can be used to break the degeneracy. Low surface gravity results in peculiar spectral characteristics, as explained in Chapter 1.2.2.

In this Chapter, we present a homogeneous set of seven medium-resolution ($R \sim 1500-1700$) spectra of M9.5-L3 dwarfs, all classified at optical wavelengths. Our sample is composed of the M9.5 object DENIS-P J124514.1-442907 (also called TWA 29; hereafter DENIS J1245) a member of TW-Hydrae (5-10 Myr), and the L0 dwarf Cha J1305-7739 (Jayawardhana & Ivanov 2006; hereafter Cha 1305), one of the least massive objects of the Chameleon II cluster. We also present the spectra of five L dwarfs with features indicative of low surface gravity ($L\gamma$ dwarfs) in the optical, identified by Cruz et al. (2009b). These objects are the two $L0\gamma$ dwarfs EROS J0032-4405 (Goldman et al. 2010; hereafter EROS J0032) and 2MASS J22134491-2136079 (Cruz et al. 2009b; hereafter 2M2213), the $L2\gamma$ dwarf 2MASSJ232252.99-615127.5 (Cruz et al. 2009b; hereafter 2M2322), and the two $L3\gamma$ dwarfs 2MASS J212650.40-814029.3 (Cruz et al. 2009b; hereafter 2M2126) and 2MASSJ220813.63+292121.5 (Cruz et al. 2009b; hereafter 2M2208).

We aim to use the spectra to confirm the low surface gravities of the objects in the near-infrared and to test the ability of the BT-Settl models to correctly handle the formation and gravitational settling of dust under reduced surface gravity conditions. These spectra enrich the scarce sample of empirical near-infrared

[†]This chapter is adapted from the paper: Manjavacas, E.; Bonnefoy, M.; Schlieder, J. E.; Allard, F.; Rojo, P.; Goldman, B.; Chauvin, G.; Homeier, D.; Lodieu, N.; Henning, 2014, *Astronomy & Astrophysics*. Vol. 564, pp. 21.

medium-resolution spectra of young late-type objects beyond the M-L transition, especially for spectral type L3. We describe our observations and the associated data reduction in Section 4.2. We present an empirical analysis of the spectral features in order to derive near-infrared spectral types and confirm the young age of our targets in Section 5.3. In Section 4.4, we describe the comparison of the atmospheric models to the observed spectra. We discuss these comparisons and derive updated target properties in Section 4.5.

4.2 OBSERVATIONS AND DATA REDUCTION

Our targets were observed with the Infrared Spectrometer And Array Camera (ISAAC, Moorwood et al. 1998) mounted on the Very Large Telescope (VLT) at the UT3 telescope. The instrument was operated in low-resolution mode with the 0.3'' slit at central wavelengths 1.25 μm , 1.65 μm , and 2.2 μm . This setup provides spectra with resolving powers of ~ 1700 , 1600, and 1500 from 1.1–1.4 μm (J band), 1.42–1.82 μm (H band), and 1.82–2.5 μm (K band). Nodding and small jittering of the source along the slit were performed to correct bad pixels and to subtract the sky and bias contributions. Sources at high airmasses were observed with the slit aligned with the parallactic angle to mitigate differential flux losses.

We observed DENIS 1245 on April 6 and April 21, 2010. We took 6×120 s exposures in the J band, and 6×90 s exposures in the H and K bands. We moved the star along the slit between two positions separated by 20 arcseconds following an ABBA strategy. We applied additional small offsets (5'') around the two source positions between each exposure to efficiently filter out nonlinear and hotpixels at the data reduction step. We followed a similar strategy for the remaining targets. Data integration times and the number of exposures are reported in Table 4.1. Early-type stars were observed soon after the science target at similar airmass to ensure a proper removal of telluric features. These observations are also summarized in Table 4.1. Calibrations were obtained during the day following the observations: flat fields, wavelength calibration frames, and frames with a star moving along the slit in low- and medium-resolution to compute the spectral curvature.

Data were reduced using the 6.1.3 version of the ISAAC pipeline (Devillard et al. 1999; Silva & Peron 2004) provided by the *European Southern Observatory*. The pipeline identifies pairs of sky-object frames and subtracts them. The calibration in wavelength and the slit curvature distortion were performed using exposures with the Xenon and Argon lamps. The slit curvature was modeled with a bivariate 2-d polynomial. The dispersion relation was computed by matching a Xenon and/or Argon atlas with the corrected spectra. The pipeline divides the raw images by the flat field, corrects for badpixels and distortion, and reconstructs the combined sky-subtracted 2D spectra from a shift of the nodded images. The object flux is extracted in each spectral channel to build the final spectrum.

Data on the objects and associated telluric standard stars were reduced in a similar way. Telluric standard star spectra were divided by a blackbody with a temperature that corresponded to their spectral type

(Theodossiou & Danezis 1991a). The He and H lines were interpolated in the resulting spectra using a low-order Legendre polynomial fit of the pseudocontinuum around the line. This produced the final estimate of the combined atmospheric and instrumental transmission. We obtained the final J, H, and K band spectra of the science targets by dividing them by this transmission.

We created 1.1-2.5 μm flux-calibrated spectra of the objects using the following procedure. The J, H, and K band ISAAC spectra were convolved with the filter transmission curves. The resulting spectra were integrated. We applied the same procedure to a flux calibrated spectrum of Vega (Mountain et al. 1985; Hayes 1985). We then searched for the normalization factor of the ISAAC spectra that could produce a contrast ratio between the integrated flux of the science target and Vega, which corresponds to the J, H, and K_s -band photometry of the objects taken from 2MASS (Cutri et al. 2003; Allers et al. 2006a).

4.3 EMPIRICAL ANALYSIS

In this section, we compare the spectral properties of our sample to those of brown dwarfs and companions found in the literature to confirm features indicative of young age and we also assign near-infrared spectral types for the targets. We select the best of the fit spectrum using χ^2 minimization as well as visual inspection over all of the wavelengths.

For that purpose, we used template spectra of young M- and L-type companions (see the description in Appendix 4.A), late-M and early-L brown dwarfs from star forming regions and young nearby associations (R from ~ 120 to ~ 11500 ; Gorlova et al. 2003; Slesnick et al. 2004; Allers et al. 2007; Lodieu et al. 2008; Allers et al. 2009, 2010; Rice et al. 2010; Allers & Liu 2013; Bonnefoy et al. 2013a; Manara et al. 2013a), young field L dwarfs (R ~ 1500 ; Kirkpatrick et al. 2006; Allers & Liu 2013; Liu et al. 2013), and MLT field dwarfs (R ~ 2000 ; McLean et al. 2003; Cushing et al. 2011). We also compared our spectra to low resolution templates (R ~ 120) of the SpeX Prism Spectral Library¹. Prior to any comparison, the spectrum of Cha J1305 was dereddened by $A_V = 3$ mag (Allers et al. 2006a) using the Fitzpatrick (1999) extinction curve with an interstellar extinction parameter $R(V)=3.1$. We assumed $A_V = 0$ for the remaining targets.

4.3.1 AN AGE-SEQUENCE OF M9.5 DWARFS

The spectrum of DENIS-P J124514.1-442907 complements an age sequence of medium-resolution spectra of optically classified M9.5 dwarfs. In Figures 4.1, 4.2, and 4.3, we show the J band, H band, and K band, respectively with a resolution of R ~ 1500 in the H and K band and of R ~ 1700 in the J band. This resolution is sufficient to study atomic and molecular lines. The age-sequence is composed of spectra of members of the Taurus (KPNO Tau 4; Briceño et al. 2002), Chameleon I (OTS 44; Oasa et al. 1999; Luhman et al. 2004), and Upper Scorpius (UScoCTIO 108B; Béjar et al. 2008) star forming regions. We also overlay

¹<http://pono.ucsd.edu/~adam/browndwarfs/spexprism/>

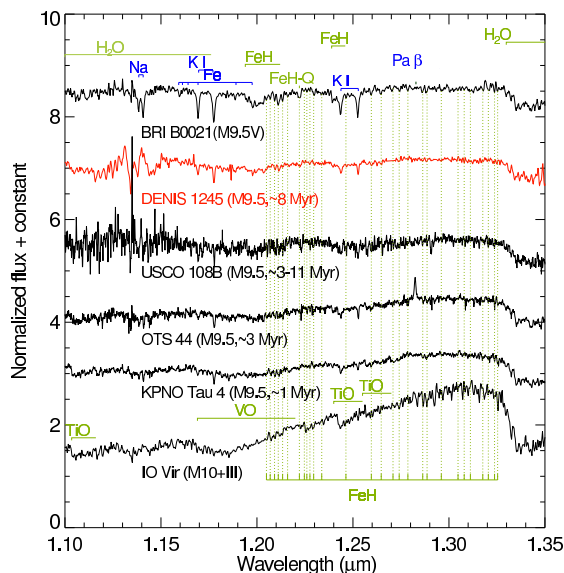


Figure 4.1: We plot the spectra of six M9.5 objects with the same optical spectral type, but different ages, i.e., gravity. We can appreciate the evolution of the spectral features with age in the J band. The most remarkable spectral features are the appearance of alkali lines at older ages.

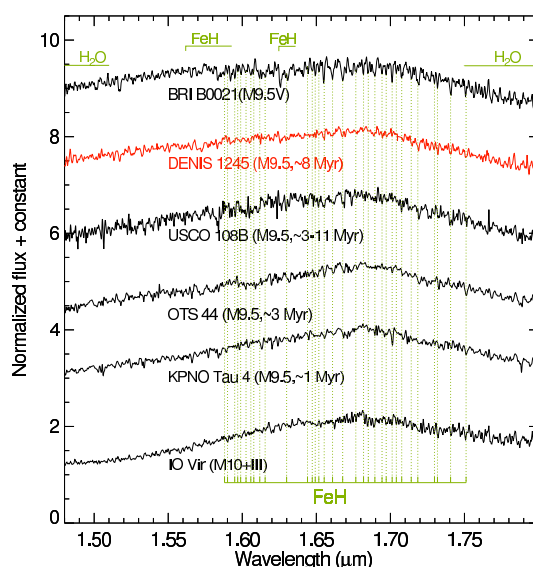


Figure 4.2: Same plot as Fig. 4.1. Here we appreciate how the H band becomes more triangular when we move to younger BDs.

Table 4.1: Observing log: λ_{ref} is the central wavelength of the band, DIT is the integration time in each position of the slit, and NDIR is the number of exposures.

Name	Date	λ_{ref} (μm)	DIT (s)	NINT	Seeing ($''$)	Airmass	Notes
DENISJ1245	April 4, 2010	1.25	120	6	1.30	1.20	
DENISJ1245	April 21, 2010	1.25	120	6	0.80	1.07	
DENISJ1245	April 21, 2010	1.65	90	6	0.70	1.06	
DENISJ1245	April 21, 2010	2.20	90	6	0.55	1.06	
HIP 064550	April 4, 2010	1.25	5	2	1.15	1.20	G1.5V Telluric Standard
HIP 055667	April 21, 2010	1.25	5	2	0.70	1.07	B2IV-V Telluric Standard
HIP 055667	April 21, 2010	1.65	5	2	0.70	1.07	B2IV-V Telluric Standard
HIP 055667	April 21, 2010	2.20	5	2	0.60	1.07	B2IV-V Telluric Standard
EROS J0032	July 6, 2010	1.25	180	6	1.30	1.07	
EROS J0032	July 15, 2010	1.65	120	6	0.85	1.07	
EROS J0032	July 15, 2010	2.20	120	6	0.85	1.07	
EROS J0032	July 25, 2010	1.25	180	6	0.70	1.10	
HIP 004722	July 6, 2010	1.25	5	2	-	1.08	G3V Telluric Standard
HIP 111085	July 15, 2010	1.65	5	2	1.02	1.16	B9V Telluric Standard
HIP 111085	July 15, 2010	2.20	5	2	1.04	1.16	B9V Telluric Standard
HIP 003356	July 25, 2010	1.25	5	2	0.80	1.07	B9.5V Telluric Standard
Cha 1305	April 6, 2010	1.65	200	6	0.90	1.90	
Cha 1305	April 21, 2010	1.25	240	8	0.60	1.67	
Cha 1305	April 21, 2010	1.65	200	6	0.50	1.66	
Cha 1305	April 21, 2010	2.20	180	10	0.80	1.70	
HIP 059830	April 6, 2010	1.65	5	2	0.80	1.97	B3V Telluric Standard
HIP 072671	April 21, 2010	1.25	5	2	-	1.60	B8V Telluric Standard
HIP 072671	April 21, 2010	1.65	5	2	0.59	1.56	B8V Telluric Standard
HIP 072671	April 21, 2010	2.20	5	2	0.75	1.56	B8V Telluric Standard
2M2322	June 9, 2010	1.25	240	6	1.00	1.35	
2M2322	June 9, 2010	1.65	120	10	0.80	1.28	
2M2322	June 9, 2010	2.20	120	10	1.00	1.26	
HIP 117661	June 9, 2010	1.25	5	2	0.70	1.40	B9V Telluric Standard
HIP 117661	June 9, 2010	1.65	5	2	0.90	1.39	B9V Telluric Standard
HIP 117661	June 9, 2010	2.20	5	2	1.00	1.33	B9V Telluric Standard
2M2126	April 21, 2010	1.65	180	6	0.60	2.02	
2M2126	April 21, 2010	2.20	180	4	0.60	1.99	
2M2126	June 7, 2010	1.25	180	12	0.90	1.84	
HIP 112781	April 21, 2010	1.65	5	2	1.10	2.08	B6IV Telluric Standard
HIP 112781	April 21, 2010	2.20	5	2	0.80	2.03	B6IV Telluric Standard
HIP 099400	June 7, 2010	1.25	5	2	0.80	1.73	B2IV Telluric Standard
2M2208	June 9, 2010	1.25	180	12	0.80	1.90	
2M2208	June 7, 2010	1.65	180	6	0.80	1.70	
2M2208	June 7, 2010	2.20	180	9	0.90	1.72	
HIP 112235	June 9, 2010	1.25	5	2	0.70	1.97	B9V Telluric Standard
HIP 112235	June 7, 2010	1.65	5	2	0.95	1.73	B9V Telluric Standard
HIP 112235	June 7, 2010	2.20	5	2	0.80	1.74	B9V Telluric Standard
2M2213	August 6, 2013	1.25	180	8	2.07	1.10	
2M2213	August 6, 2013	1.65	110	2	1.97	1.21	
2M2213	August 6, 2013	2.20	150	2	...	1.22	
HIP 114656	August 6, 2013	1.25	5	2	2.27	1.04	B9V Telluric Standard
HIP 114656	August 6, 2013	1.65	5	2	1.71	1.05	B9V Telluric Standard
HIP 114656	August 6, 2013	2.20	5	4	...	1.11	B9V Telluric Standard

the spectrum of the M10III Mira IO Virginis (Rayner et al. 2009) as an example of an extremely low surface gravity atmospheres. This sequence further highlights age-sensitive and gravity-sensitive features

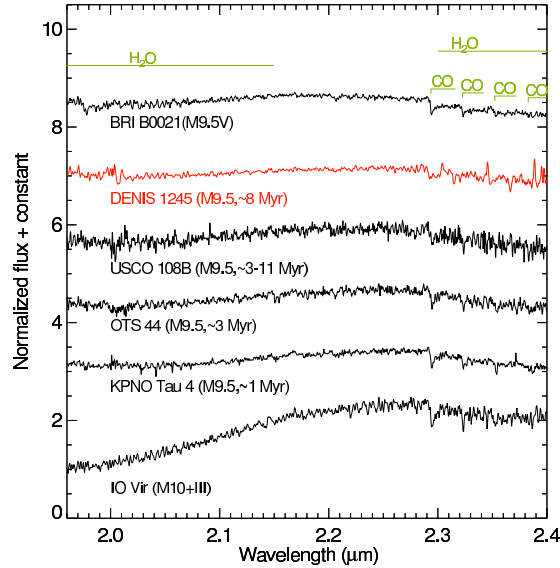


Figure 4.3: Similar plot to Fig. 4.1 and 4.2 in the K band.

reported in the literature: the increase of the alkali line depths (K I, Na I), an increase in the strength of the FeH absorptions at 1.20 and 1.24 μm , and of the H₂O band (1.7-2.25 μm). The sequence also confirms the decrease of the VO band strength from 1.17 to 1.22 μm and that the J band slope becomes bluer when the age increases, as shown by Kirkpatrick et al. (2006) (see Fig. 4.1). The other main feature that changes is the progressive appearance of the triangular H band profile when the age decreases, which corresponds to the water absorption profile (Fig. 4.2). We used these characteristic features to confirm the young age and/or low surface gravity of the L γ field dwarfs in our sample.

4.3.2 YOUNG FIELD L-DWARFS?

In this section, we discuss the best-fit spectra for each L-dwarf of our sample. Among the sample of L dwarfs, the Chameleon member Cha J1305-7739 shows clear features indicative of low surface gravity. This is in agreement with the age of the source. The remaining L dwarfs of our sample do not have assigned membership to young moving groups or clusters, and, hence, lack well-determined ages. We therefore tried to identify features in the near-infrared typical of low surface gravity objects that would confirm the analysis derived by Cruz et al. (2009b) in the optical. Plots that show the best matches can be found in the Appendix 4.B, and the most remarkable result is shown in Figure 4.4.

The near-infrared spectrum of the L0 γ dwarf EROS J0032 has spectral features midway between the medium-resolution ($R \sim 2000$) NASA Infrared Telescope Facility (IRTF) spectrum (Cushing et al. 2011) of the L1 field dwarf 2MASS J02081833+2542533 and of the M9.5 companion UScoCTIO 108B (Bonfey et al. 2013a). The object EROS J0032 has a plateau from 1.59-1.69 μm characteristic of field dwarfs, but a

more triangular shape in the H band, and weaker FeH, and K I lines in the J band. Conversely, it has deeper K I lines (1.169, 1.177, 1.243, 1.253 μm) and FeH bands at 1.2 μm and 1.624 μm than its companion. The 1.1-1.8 μm spectrum of the L0 \pm 1 companion to the Upper Scorpius star GSC 06214-00210 (Ireland et al. 2011; Bowler et al. 2011) perfectly reproduces the pseudocontinuum shape of EROS J0032. The companion has nonetheless slightly weaker FeH and K I absorptions. The near-infrared spectral slope of EROS J0032 is redder than the slope of the L0 field dwarf standard 2MASS J03454316+2540233 (McLean et al. 2003; Kirkpatrick et al. 2010). This can be attributed to reduced CIA of H₂ (Borysow et al. 1997; Kirkpatrick et al. 2006), and, therefore, low surface gravity. The object EROS J0032 also has reduced FeH lines at 1.2 μm and a more triangular H band shape than the standard. Nevertheless, the two spectra have comparable K I line depths. The Spectrograph for INtegral Field Observations in the near-infrared (SINFONI) spectrum of the L0 γ benchmark 2MASS J01415823-4633574 (Bonnetfoy et al. 2013a) has a more triangular H band shape, weaker FeH absorptions, and K I lines than the object. Allers & Liu (2013) and Marocco et al. (2013a) also found an indication of low surface gravity in near-infrared spectra of EROS J0032. The lower-resolution spectrum (R \sim 100) of EROS J0032 of Allers & Liu (2013) perfectly matches our ISAAC spectrum. Allers & Liu (2013) assign the same gravity class for this target as for AB Pic b, a \sim 30 Myr old low-mass L0 (Bonnetfoy et al. 2013a) companion. Here, we conclude that EROS J0032 only shows *moderate* signs of low surface gravity.

The object EROS J0032 and the second L0 γ dwarf of our sample 2M2213 have comparable near-infrared spectral slopes. Nevertheless, we find that 2M2213 has a H band shape, K I and FeH line depths midway between those of EROS J0032 and UScoCTIO 108B. Therefore, this comparison suggests that 2M2213 has a lower surface gravity and is younger age than EROS J0032, but is older than the assumed age of Upper Scorpius (\sim 5-11 Myr; Preibisch & Zinnecker 1999; Slesnick et al. 2008; Pecaute et al. 2012). Marocco et al. (2013a) also obtained a medium-resolution near-infrared spectrum of this object, and reach similar conclusions. They classify it as a L2pec based on the good match with the near-infrared spectrum of a field L2 standard. Nevertheless, such a comparison can not be done for young objects (Luhman et al. 2004), as it can lead to later spectral type estimates. To conclude, we find that our spectrum perfectly matches the low-resolution (R \sim 100) spectrum of 2M2213 obtained by Allers & Liu (2013).

In Figure 4.4 we show that the spectrum of the L2 γ dwarf 2M2322 is reproduced by the spectrum (Bonnetfoy et al. 2013a) of the moderately old L4.5+L4.5 binary companion GJ417 B (age from 80 to 890 Myr, Kirkpatrick et al. 2001; Allers et al. 2010). But the object exhibits weaker FeH absorption, and K I lines than its companion. The pseudocontinuum shape of 2M2322 from 1.95 to 2.5 μm , and from 1.45 to 1.6 μm is midway between the one of GJ 417 B and of the 5-11 Myr old L4 planetary mass companion 1RXS J160929.1-210524b (Lafrenière et al. 2008b, 2010b). All three objects have similar near-infrared spectral slopes. The object 2M2322 also has a slightly redder spectral slope, more triangular H band, and bumpy pseudocontinuum in the K band than the L2 field dwarf standard Kelu-1 AB (Cushing et al. 2011; Kirkpatrick et al. 2010). All of these comparisons provide evidence that this object has a low surface gravity. As a by-product, the companion suggests that 1RXS J160929.1-210524b has a spectral type L2.

The 1.1-2.5 μm pseudo-continuum of 2M2126 is well reproduced by the spectrum of the young (\sim 20-300 Myr Zapatero Osorio et al. 2010) L3 γ companion G 196-3B (Rebolo et al. 1995) gathered by Allers

& Liu (2013). The depth of alkali-lines and of the FeH absorption at $1.2 \mu\text{m}$ are similar for the two objects. Nevertheless, the water-band absorptions from $1.33\text{-}1.35 \mu\text{m}$ and $1.45\text{-}1.6 \mu\text{m}$ are deeper in the companion spectrum. The spectral slope from $1.2\text{-}1.33 \mu\text{m}$ is also redder in the spectrum of G 196-3B. We also find a good match with the spectrum of the brown dwarf companion CD-35 2722B (Wahhaj et al. 2011), classified as L3 by Allers & Liu (2013). The object CD-35 2722 B forms a coeval system with CD-35 2722 A, a member of the 75-150 Myr old AB Doradus association. We then conclude that 2M2126 is a young object, with indications of reduced surface gravity, and features in the near-infrared consistent with its optical class L3 γ determined by Cruz et al. (2009b).

The second L3 γ dwarf of the sample, 2M2208, has an identical spectrum to 2M2126. Both objects show comparable K I and FeH line depths in the J band, and a similar gravity-sensitive slope from 1.45 to $2.29 \mu\text{m}$. Nevertheless, this object has a bluer $1.1\text{-}2.5 \mu\text{m}$ slope than 2M2126 (and therefore G196-3B). The blue slope likely arises from an improper scaling of the J, H, K band spectra due to uncertainty in the photometry. Indeed, the $1.1\text{-}1.35 \mu\text{m}$ portion of the spectrum has a slightly higher flux than the low-resolution ($R\approx 100$) spectrum of the source obtained by Allers & Liu (2013), but a similar pseudocontinuum otherwise. The slope is better reproduced by the spectrum of GJ417 B (Kirkpatrick et al. 2001; Bonnefoy et al. 2013a) and by an IRTF spectrum of the L3 field dwarf 2MASS J15065441+1321060 (Reid et al. 2000; Cushing et al. 2011). But the KI and FeH lines are weaker in the spectrum of 2M2208 than in the spectra of these two objects. Therefore, the analysis confirms that 2M2208 shows signature characteristics of young L3-L5 objects, and a spectral type similar to that of 2M2126.

4.3.3 INDICES AND EQUIVALENT WIDTHS

To further assess the age, surface gravity, and spectral classes of our targets, we computed spectral indices and equivalent widths that quantify the evolution of the main absorption features.

We first used spectral indices measuring the strength of the main water bands. These indices were selected independently by Bonnefoy et al. (2013a) and/or Allers & Liu (2013) from Allers et al. (2007) – H_2O , Slesnick et al. (2004) – $H_2O\text{-}1$ and $H_2O\text{-}2$, and McLean et al. (2003) – H_2OD . They are known to show a clear trend with the spectral type, and to be only weakly sensitive to the age or to the gravity class (γ , β). We computed them on the compilation of near-infrared spectra of young M3-M9.5 dwarf members of star forming regions (1-11 Myr) and young nearby associations (age <50 Myr) classified in the optical. We also derived them for young L γ , L β dwarfs, and companion spectra provided by Allers & Liu (2013) and Bonnefoy et al. (2013a), and for field dwarfs obtained by McLean et al. (2003) and Cushing et al. (2011). We degrade the resolution of all the spectra to $R\sim 100$, which is our lowest resolution. Results are shown in Figure 4.5. We reajusted a third-order polynomial function on these trends (Table 4.2), as in Allers & Liu (2013), and use them to derive spectral type estimates (Table 4.3). We calculated the errors in the spectral type as the root mean square (rms). We estimated the final near-infrared spectral types, obtaining the mean of the different estimates from the indices weighted by the associated error, and their errors, as the standard deviation. These estimates are all consistent with the optical spectral types. They are also consistent with the matches found in Section 4.3.2.

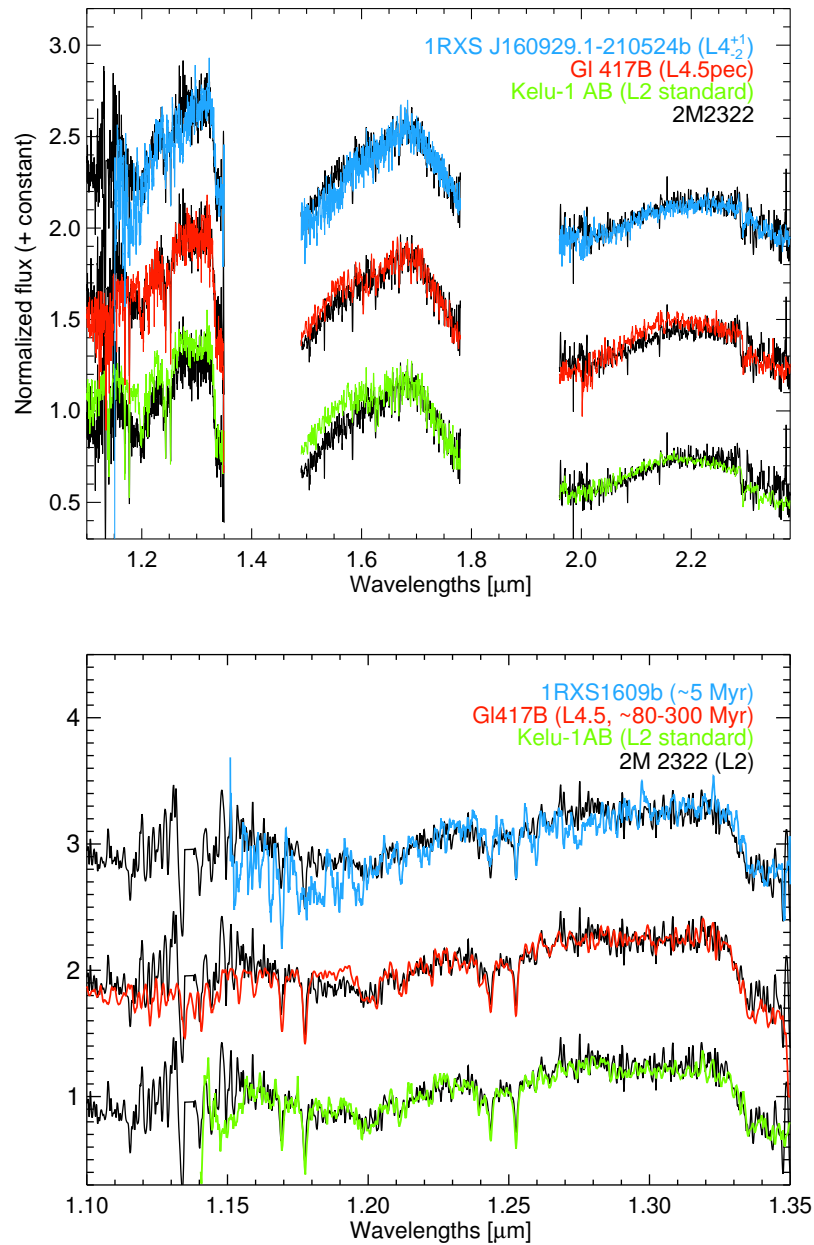


Figure 4.4: In the plot at the top, we show the comparison of the 1.1-2.38 μm spectrum of the L2 γ dwarf 2M2322 to the L2 optical standard (Kelu-1 AB Ruiz et al. 1997; Cushing et al. 2011), of the young L4.5 binary companion GJ 417B (Kirkpatrick et al. 2001; Bonnefoy et al. 2013a), the planetary mass companion 1RXS J160929.1-210524b (Lafrenière et al. 2008b, 2010b). In the plot at the bottom, we show the J band in a higher detail.

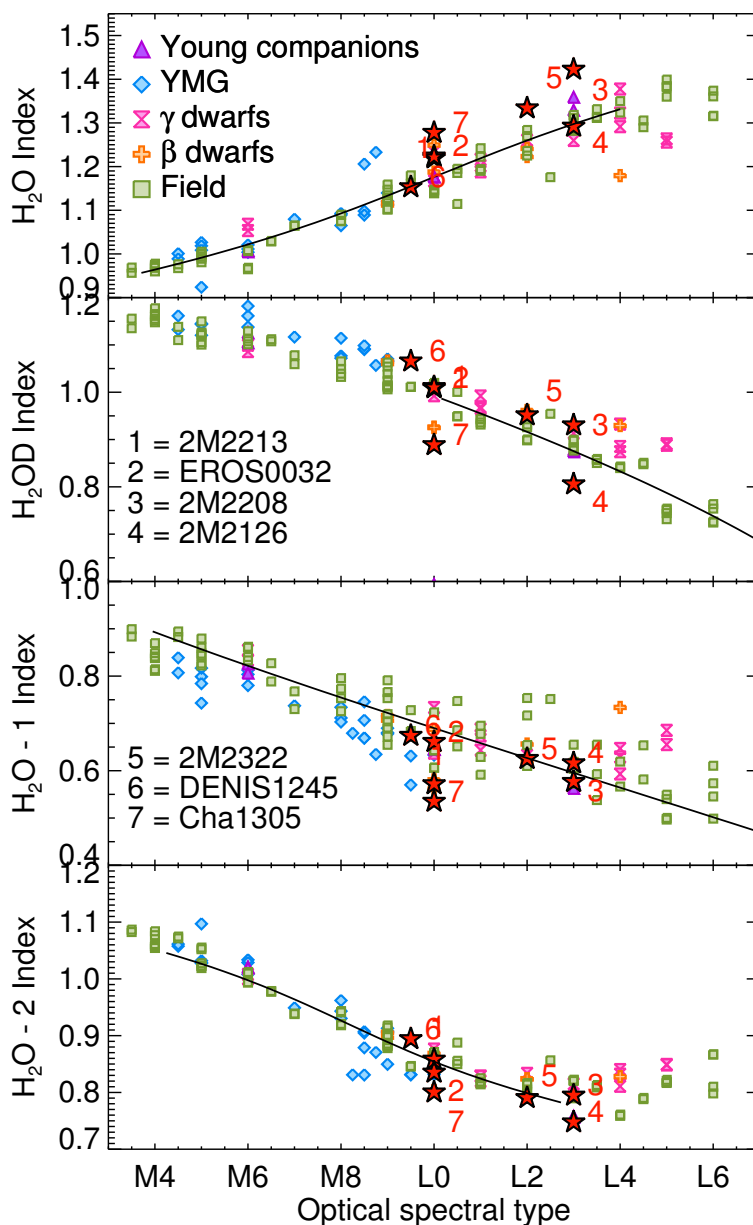


Figure 4.5: Spectral indices used for the spectral type estimation of the NIR spectral type. Our targets are represented by red stars and are numerated from 1 to 6: 1 = 2M2213, 2 = EROS J0032, 3 = 2M2208, 4 = 2M2126, 5 = 2M2322, 6 = DENIS 1245 and 7 = Cha1305. The black lines represent the three degree polynomial fit to the field brown dwarfs. We report the index values for objects classified in the optical that are members of young clusters, star forming regions, or nearby associations (YMG), and for dwarfs with low (γ) and intermediate (β) gravity classes (Kirkpatrick 2005).

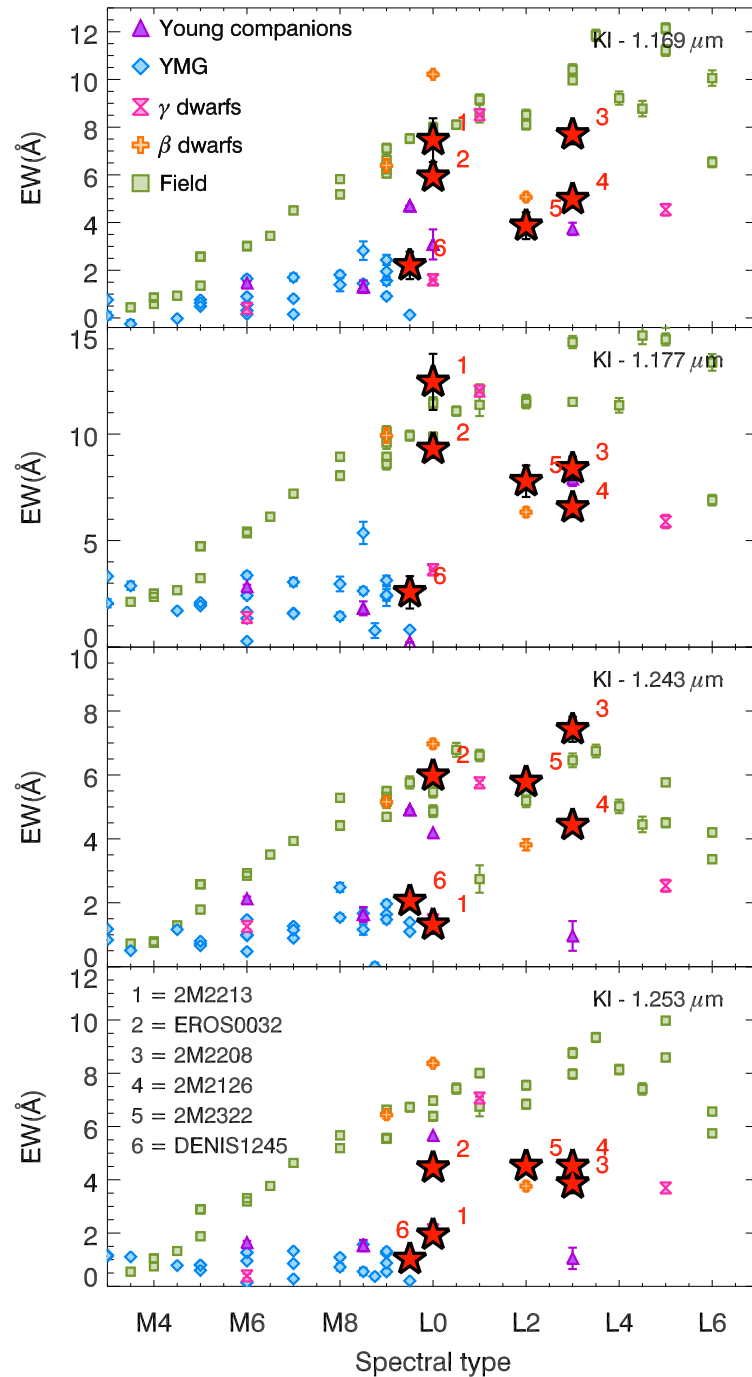


Figure 4.6: Equivalent widths for the K I lines at $1.169 \mu\text{m}$, $1.177 \mu\text{m}$, $1.243 \mu\text{m}$, and $1.253 \mu\text{m}$ for our targets (red stars) and reference objects.

Table 4.2: Coefficient of the polynomial fit derived from index values computed on field dwarf spectra and shown in Figure 4.5

Index definition	References	SpT	Coefficients of Polynomial Fits				RMS Sp. type
			a	b	c	d	
$H_2O = \frac{\langle F_{\lambda} \rangle_{[1.550, 1.560]}}{\langle F_{\lambda} \rangle_{[1.492, 1.502]}}$	Allers et al. (2007)	M4-L4	-199.72	487.93	-394.58	111.66	1.0
$H_2OD = \frac{\langle F_{\lambda} \rangle_{[1.951, 1.977]}}{\langle F_{\lambda} \rangle_{[2.062, 2.088]}}$	McLean et al. (2003)	L0-L6	20.16	10.28	-24.13	3.48	1.0
$H_2O - 1 = \frac{\langle F_{\lambda} \rangle_{[1.335, 1.345]}}{\langle F_{\lambda} \rangle_{[1.295, 1.305]}}$	Slesnick et al. (2004)	M4-L6	29.42	-17.94	-24.98	14.73	0.5
$H_2O - 2 = \frac{\langle F_{\lambda} \rangle_{[2.035, 2.045]}}{\langle F_{\lambda} \rangle_{[2.145, 2.155]}}$	Slesnick et al. (2004)	M4-L3	306.25	-917.19	965.74	-348.88	1.0

Table 4.3: Estimation of the near-infrared spectral types based on spectral indices

Name	Opt SpT	Reference	Empirical SpT	Index SpT				NIR SpT
				H_2O	H_2OD	$H_2O - 1$	$H_2O - 2$	
DE J1245	M9.5	1	M9	M9.5±1.0	M8.0±1.0	L0.5±0.5	M9.0±1.0	M9.5±1.0
EROS J0032	L0 γ	2,6	L1	L1.0±1.0	L0.0±1.0	L1.0±0.5	L0.5±1.0	L0.5±0.5
2M J2213	L0 γ	8	L0	L1.0±1.0	M9.5±1.0	L3.5±0.5	L0.0±1.0	L2.0±1.5
Cha J1305	L0	3,7	L1	L2.5±1.0	L2.5±1.0	L5.0±0.5	L2.0±1.0	L3.5±1.5
2M J2322	L2 γ	4, 8	L2	L4.0±1.0	L1.0±1.0	L2.0±0.5	L2.5±1.0	L2.0±1.0
2M J2126	L3 γ	4, 8	L3	L3.0±1.0	L5.5±1.0	L2.0±0.5	L4.5±1.0	L3.0±1.5
2M J2208	L3 γ	5, 8	L1	L7.0±1.0	L2.0±1.0	L3.5±0.5	L2.0±1.0	L3.0±2.0

[1] - Looper et al. (2007); [2] - Reid et al. (2008b); [3] - Allers et al. (2006a); [4] - Reid et al. (2008b); [5] - Allen et al. (2007); [6] - Allers & Liu (2007); [7] - Alcalá et al. (2008); [8] - Cruz et al. (2009b);

The equivalent widths of the gravity-sensitive K I lines at 1.169 μm , 1.177 μm , 1.243 μm , and 1.253 μm of our objects are reported in Table 4.4. They were computed following the method developed by Sembach & Savage (1992). We used the same reference wavelengths for the fit of the pseudocontinuum and for the line as Allers & Liu (2013). In Fig. 4.6, we show the equivalent widths of these lines as for our targets and reference objects. The trends are similar to those found by Bonnefoy et al. (2013a) and Allers & Liu (2013). For all four cases, EROS J0032 has an equivalent widths close to those of field L0 dwarf analogues. The remaining field L γ dwarfs have lower equivalent widths in some, but not all of the diagrams. This confirms the conclusions derived in Section 4.3.2. The object DENISJ1245 has equivalent widths comparable as late-M dwarf members of the \sim 8 Myr old TW Hydrae and Upper Scorpius. This is consistent with the membership of this object to the TW Hydrae association (see Looper et al. 2007 and Section 4.5.2.1). We calculate the KI_J index for medium-resolution spectra degraded at $R \sim 700$. We find similar results and trends (Figure 4.7) in the KI_J index defined by Allers & Liu (2013), and measure the depth of the K I doublet at 1.243-1.253 μm . The spectrum of Cha J1305 was too noisy to derive equivalent widths and KI_J index values.

We also computed the FeH_J and $H - cont$ indices defined by Allers & Liu (2013). These indices measure

Table 4.4: Age-sensitive indices and equivalent widths

Object	FeH _J (a)	KI _J (a)	H – cont (a)	EW - K I 1.169 μm (Å)	EW - K I 1.177 μm (Å)	EW - K I 1.243 μm (Å)	EW - K I 1.253 μm (Å)
DE J1245	1.091 ± 0.005	1.058 ± 0.002	0.992 ± 0.001	2.20 ± 0.57	2.57 ± 0.76	2.05 ± 0.13	1.02 ± 0.12
EROS J0032	1.200 ± 0.003	1.096 ± 0.005	0.925 ± 0.001	5.92 ± 0.31	9.30 ± 0.41	5.97 ± 0.17	4.46 ± 0.16
2M J2213	1.134 ± 0.004	1.034 ± 0.004	0.958 ± 0.002	7.45 ± 0.92	12.45 ± 1.31	1.31 ± 0.28	1.94 ± 0.25
2M J2322	1.144 ± 0.009	1.112 ± 0.003	0.935 ± 0.001	3.86 ± 0.56	7.78 ± 0.74	5.78 ± 0.21	4.51 ± 0.19
2M J2126	1.183 ± 0.010	1.061 ± 0.003	0.949 ± 0.001	4.98 ± 0.34	6.55 ± 0.46	4.43 ± 0.22	4.52 ± 0.20
2M J2208	1.118 ± 0.010	1.063 ± 0.003	0.930 ± 0.001	7.69 ± 0.41	8.39 ± 0.55	7.43 ± 0.39	3.86 ± 0.36

(a) Computed using the code developed by Allers & Liu (2013).

the strength of the gravity sensitive FeH feature at 1.2 μm and the shape of the H band continuum, respectively. We calculate the FeH_J index using medium-resolution spectra degraded at $R \sim 700$. Nonetheless, we use all the spectra smoothed to $R \sim 100$ to calculate the $H - cont$ index, as the H band is broad enough not to be significantly affected by the spectral resolution. The index values are reported for the targets in Table 4.4 and compared to other objects in Fig. 4.7. All the objects, except EROS J0032 have index compatible with the trends of objects from young moving groups and γ and β dwarfs. This further indicates that EROS J0032 is the object with the highest surface gravity and/or the oldest age of the sample.

4.4 SPECTRAL SYNTHESIS

In the following sections, we compare the dereddened near-infrared spectra of our objects to predictions from BT-Settl atmospheric models (Allard et al. 2003, 2007, 2011). The models have already been tested on near-infrared spectra of young M5.5-L0 objects by Bonnefoy et al. (2013a). We compare the new ISAAC spectra to derive the atmospheric parameters (T_{eff} , $\log g$) of the objects and to reveal nonreproducibilities of the models for later spectral types. Flux in synthetic spectra are provided per cm^2 of the stellar surface. They therefore need to be scaled back, using the distance modulus, to absolute flux. The models are described in Allard et al. (2011), Allard et al. (2012a), and Allard et al. (2012c). We summarize their most relevant characteristics below.

We used the 2010 and 2013 prerelease of these models². The comparative analysis of the results provided by these two versions enables us to judge the pertinence of new physics incorporated. With this approach,

²The 2013 prerelease of the models corresponds to the final and stable version of the 2012 model grid (called BT-Settl 2012; used in Bonnefoy et al. (2013c,a,b)) where some synthetic spectra were recomputed following the discovery of errors in the model code. Upgrades in the 2012 grid were released progressively on the *Star, Brown Dwarf & Planet Simulator* web server (<http://phoenix.ens-lyon.fr/Grids/BT-Settl/CIFIST2011/RESTARTS/>) until September 2013. Therefore, we decided to call the most recent version of the models used in this study *BT-Settl 2013*, even if a new version of the BT-Settl models may be released on the web server by the end of 2013.

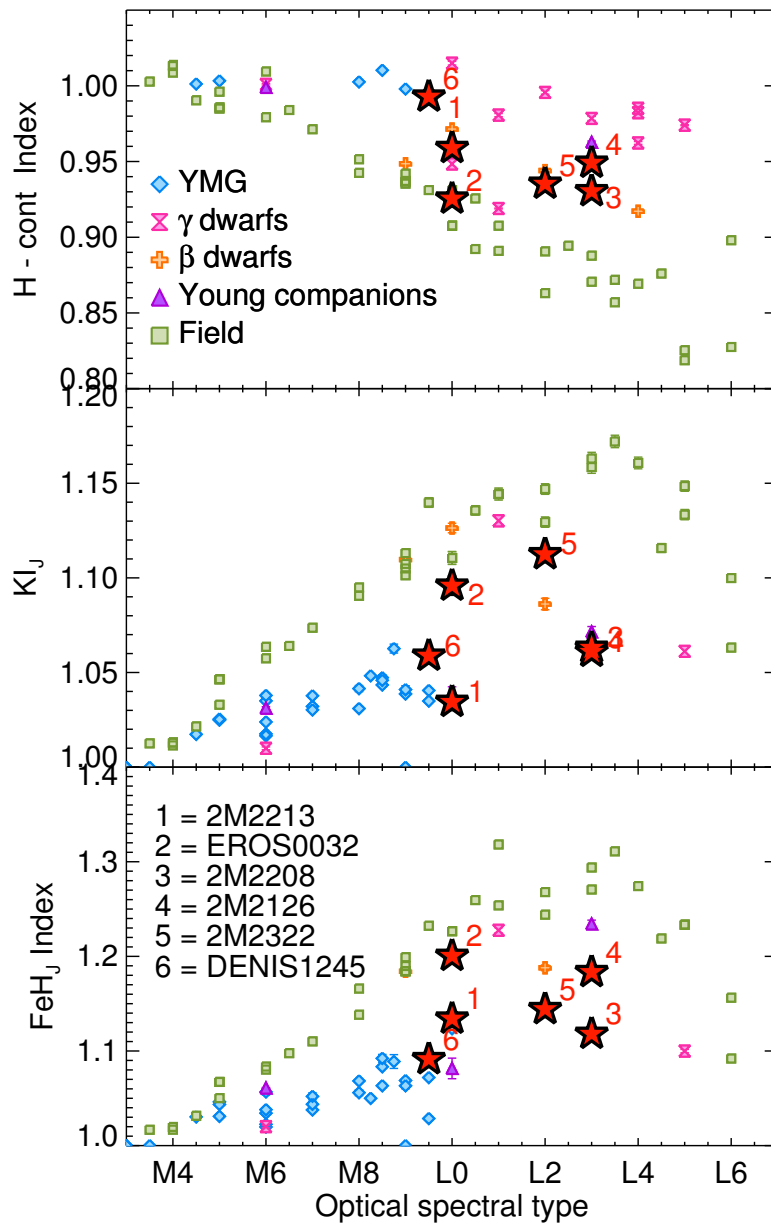


Figure 4.7: FeH, KI_J, and H band age-sensitive indices.

we also avoid relying only on the most recent version of the models, which remain to be tested, contrary to the BT-Settl 2010 models (e.g. [Bonnetfoy et al. 2013a](#)). In the 2013 pre-release of the BT-Settl models ([Allard et al. 2011](#) hereafter BT-Settl 2013), the cloud model was improved with a dynamical determination of the supersaturation, the implementation of a grain size-dependent forward scattering, and by accounting for grain nucleation based on cosmic rays studies ([Tanaka 2005](#)). The BT-Settl 2010 models rely on the reference solar abundances of [Asplund et al. \(2009\)](#). Conversely, the BT-Settl 2013 models are based on the CIFIST photospheric solar abundances of [Caffau et al. \(2011\)](#). Therefore, the 2013 solar metallicity models have atmospheres slightly enriched with C, O compared to the 2010 models, e.g., in elements involved in the formation of the main molecular absorbers in the near-infrared (CO, H₂O) and of dust grains (e.g., Forsterite - Mg₂SiO₄, Enstatite - MgSiO₃), which either contribute to the atmospheric opacity or deplete the gas phase from elements.

We selected subgrids of synthetic spectra with $1000 \text{ K} \leq T_{eff} \leq 3000 \text{ K}$, $3.0 \leq \log g \leq 5.5$ (≥ 3.5 below 2000 K), and $[M/H]=0$. An alternative subgrid of the BT-Settl 2013 models ($1000 \text{ K} \leq T_{eff} \leq 3000 \text{ K}$, $3.5 \leq \log g \leq 5.5$) with $M/H=+0.5$ dex was also used to explore the effect of the metallicity on the determination of $\log g$ and T_{eff} . The spacing of the model grid is 100 K and 0.5 dex in $\log g$.

4.4.1 NEAR-INFRARED SPECTRA

The BT-Settl 2010 and the 2013 synthetic spectra were smoothed to the resolution of ISAAC. The models were then reinterpolated on the ISAAC wavelength grid. Spectra were normalized in the following wavelength intervals 1.1-1.35 μm (J), 1.46-1.80 μm (H), 2.02-2.42 μm (K), and 1.1-2.42 μm (JHK), and compared in these intervals using least-squares. Results from the fit were always checked visually. This often revealed inappropriate fitting solutions induced by the remaining uncertainties in the models. Fits with the BT-Settl 2010 model spectra were, in particular, affected by a numerical noise introduced by the limited original wavelength sampling of the models ([Bonnetfoy et al. 2013a](#)). The fits with the BT-Settl 2013 models were more affected by the nonsimultaneous fit of the water bands longward 1.33 μm and by the improper modeling of the H band shape. Atmospheric parameters corresponding to the best fit models are reported in [Table 5.9](#). The parameters T_{eff} , $\log g$, and M/H have minimum uncertainties of 100 K, 0.5 dex, and 0.5 dex respectively. These errors correspond to the sampling of the atmospheric parameters of the model grids. We show the best fit synthetic spectra in [Figures 4.8 to 4.11](#).

BT-Settl models reproduce the shape of the pseudocontinuum and of the prominent narrow atomic (K I, Na I) and molecular (CO) lines of the objects when each band is fitted independently from each other. We recover the nonreproducibility from 1.6 to 1.7 μm and from 1.195-1.205 μm quoted in [Bonnetfoy et al. \(2013a\)](#) and, it is at least partially, due to missing FeH opacities. The ability to reproduce the data is worse in the case of EROS J0032. The spectrum of this object has features more typical of mature field dwarfs ([Section 5.3](#)). This miss-match is consistent with the conclusions of [Bonnetfoy et al. \(2013a\)](#), who find a similar departure of the models at these wavelengths in field L-dwarf spectra.

The surface gravity of Cha1305 and DENIS J1245 found with BT-Settl 2010 falls in the range expected

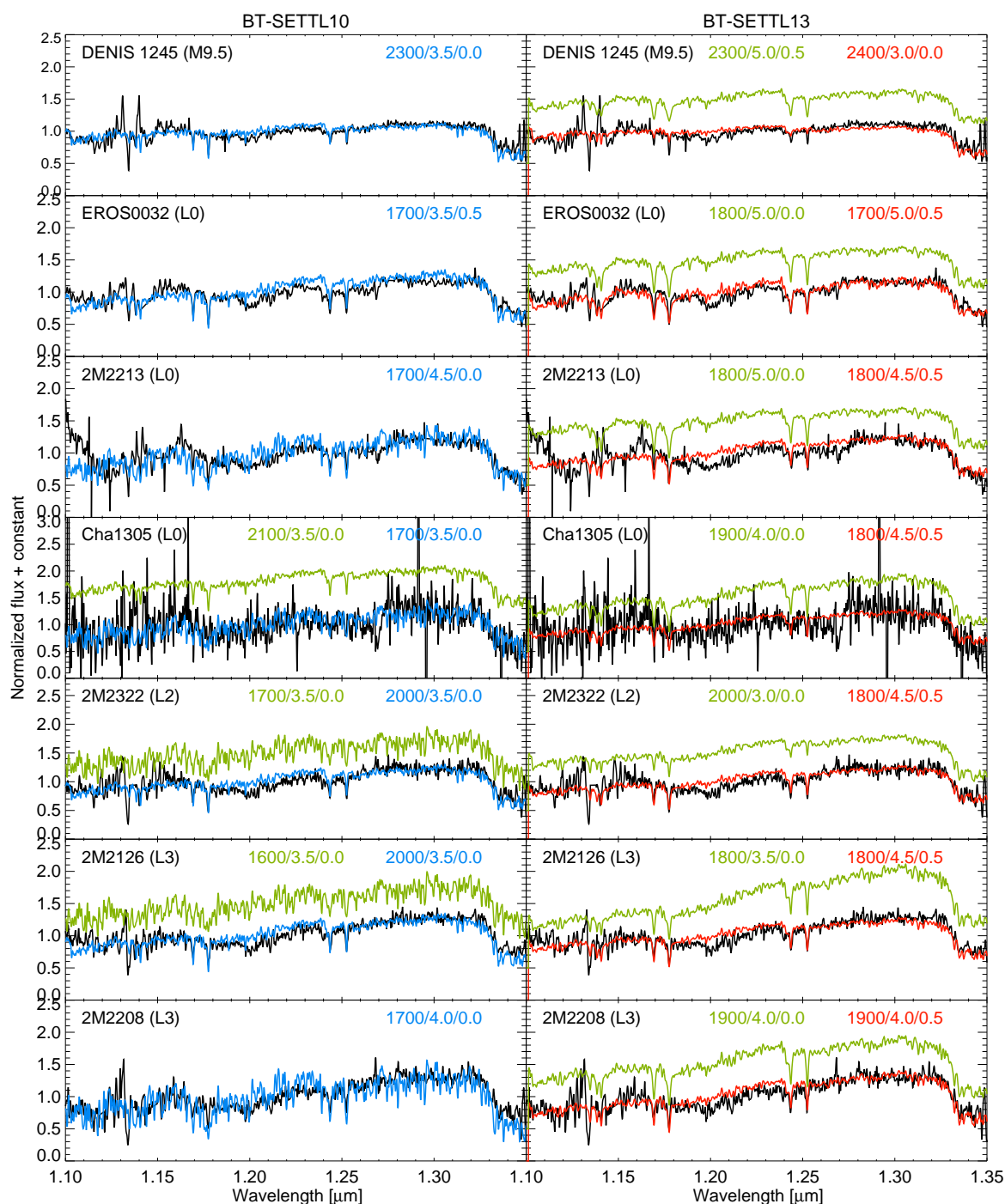


Figure 4.8: Visual comparison of the best fit BT-Settl 2010 (left panel, blue) and BT-Settl 2013 (right panel, red) synthetic spectra to the six new ISAAC spectra of young M9.5-L3 dwarfs in the J band (1.1-1.35 μm). All spectra have been normalized over the wavelength interval. Alternative solutions are shown in light green and are shifted by +0.3 to +0.5 flux normalized units for clarity.

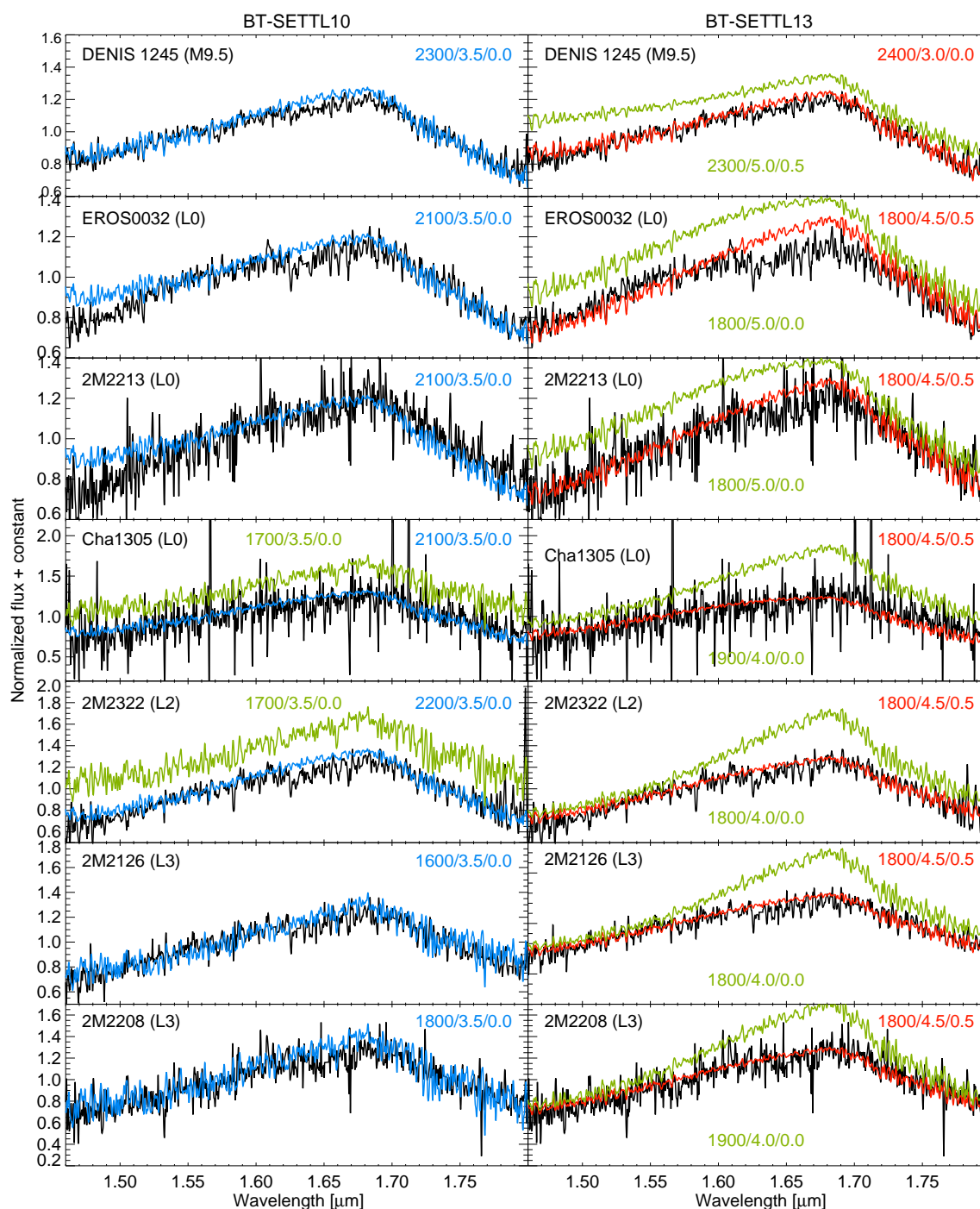


Figure 4.9: Same as Figure 4.8, but in the H band (1.46-1.8 μm).

from evolutionary models for 1-10 Myr objects. It also corresponds, within error bars, to the one determined for late-M/early-L targets from Chameleon and TW Hydrae by Bonnefoy et al. (2013a) based on the same analysis tools and models. The BT-Settl 2013 models fit a higher surface gravity and metallicity

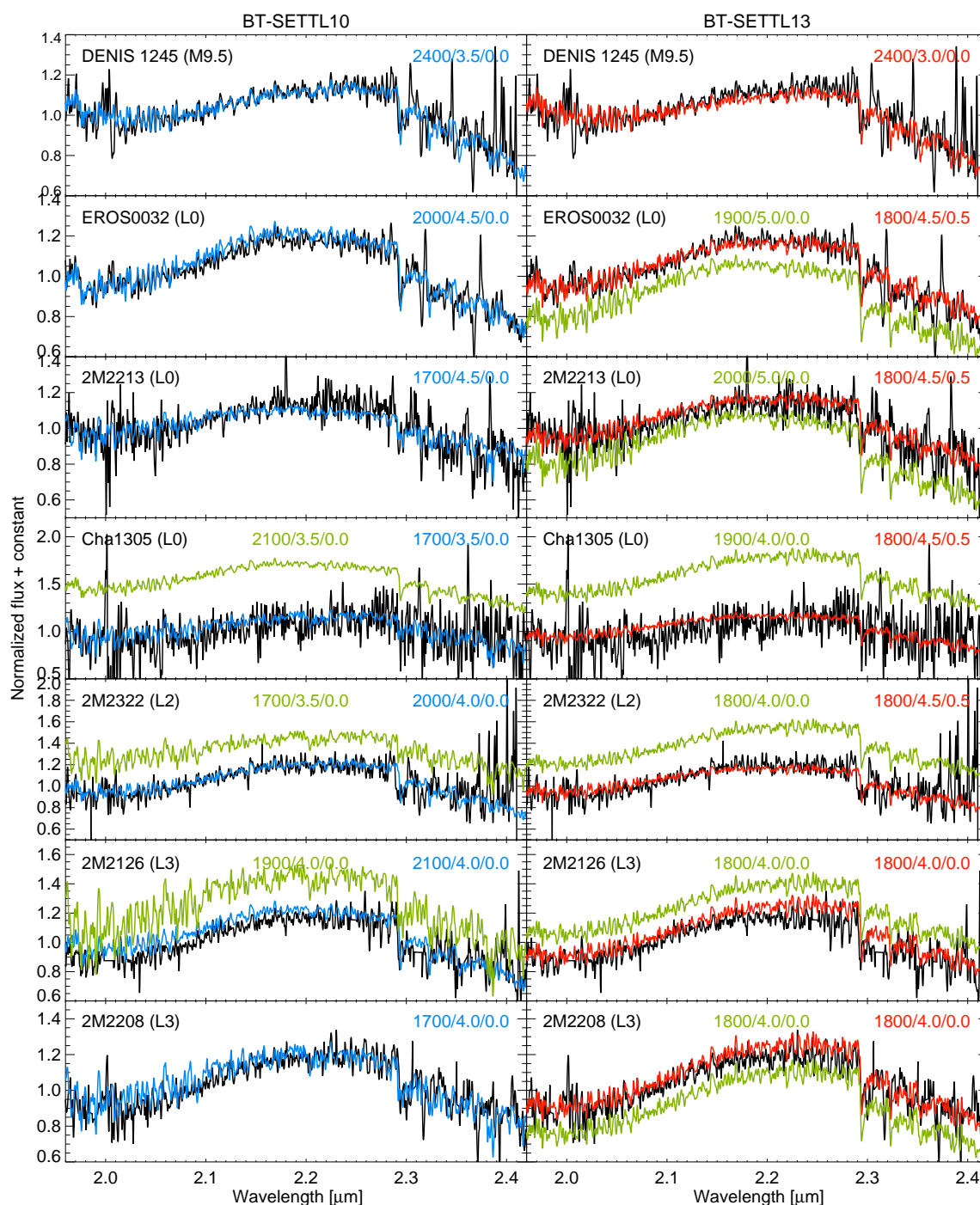


Figure 4.10: Same as Figure 4.8, but in the K band (1.96-2.42 μm).

to the spectrum of Cha1305. The two parameters are known to have counteracting effects on the atmospheric pressure at a given optical depth (see Mohanty et al. 2007) and dust content in the atmosphere. They can then induce opposite variations of the main spectroscopic features (Looper et al. 2008b). There-

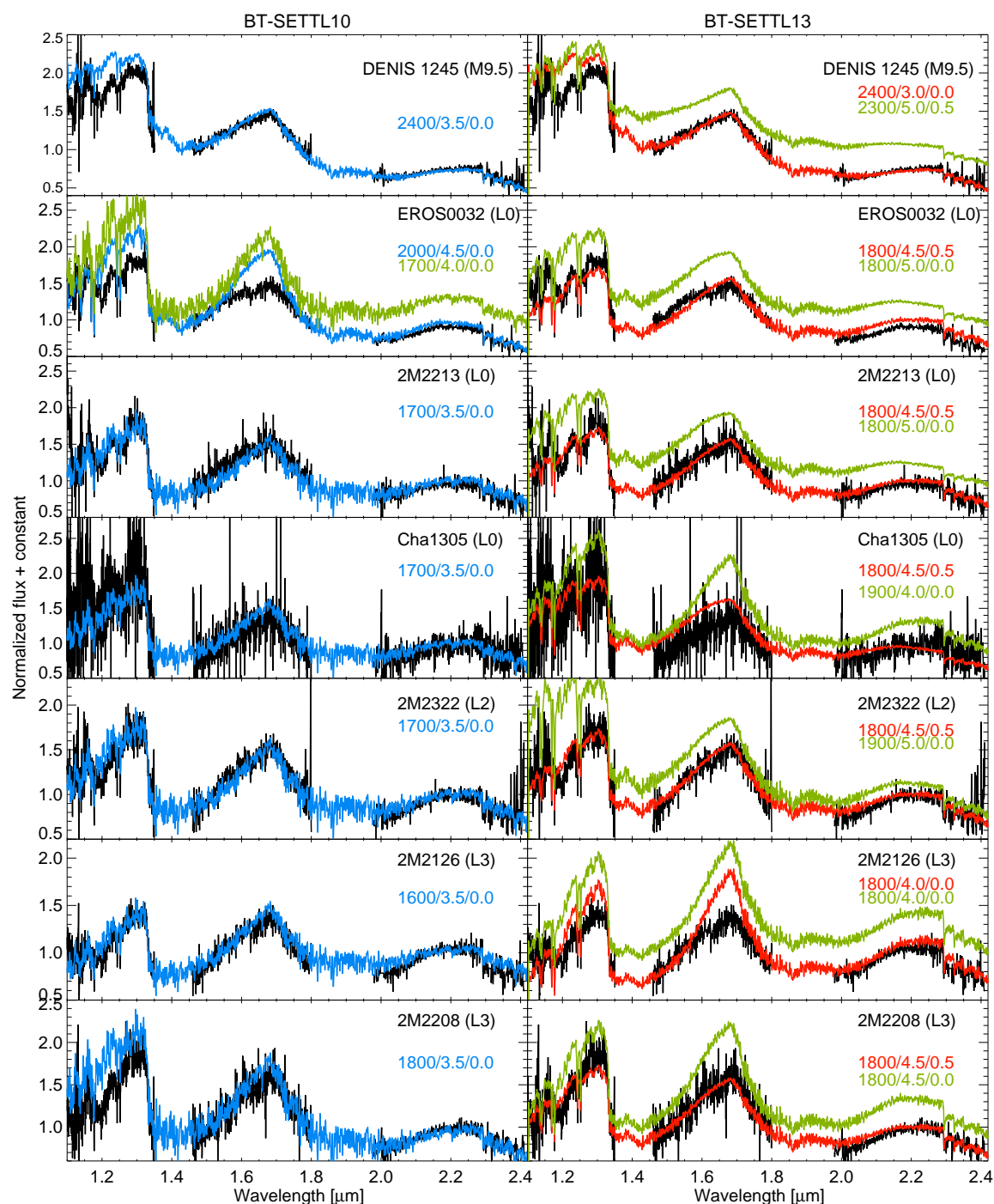


Figure 4.11: Same as Figure 4.8, but for the whole near-infrared spectrum (1.1-2.42 μm).

fore, the higher surface gravity found for Cha1305 is likely caused by the degenerate effect of metallicity. We find an alternative solution with a lower surface gravity for this object at solar metallicity (see Figure 4.11), which provides a good fit of the 1.1-2.5 μm spectrum, but fails to reproduce the shape of the

Table 4.5: Atmospheric parameters corresponding to the best fit spectra or synthetic fluxes for our seven targets. We give $T_{eff}/\log g/[M/H]$.

Model	Band	DENIS J1245	EROS J0032	2M2213	Cha 1305	2M 2322	2M 2126	2M 2208
BT-Settl 2010	J	2300/3.5/0.0	2100/3.5/0.0	1700/4.5/0.0	1700/3.5/0.0	2000/3.5/0.0	2000/3.5/0.0	1700/4.0/0.0
BT-Settl 2010	H	2300/3.5/0.0	2100/3.5/0.0	1700/4.5/0.0	2100/3.5/0.0	2200/3.5/0.0	1600/3.5/0.0	1800/3.5/0.0
BT-Settl 2010	K	2400/3.5/0.0	2000/4.5/0.0	1700/4.5/0.0	1700/3.5/0.0	2000/4.0/0.0	2100/4.0/0.0	1700/4.0/0.0
BT-Settl 2010	JHK	2400/3.5/0.0	2000/4.5/0.0	1700/3.5/0.0	1700/3.5/0.0	1700/3.5/0.0	1600/3.5/0.0	1800/3.5/0.0
BT-Settl 2010	SED	2200/3.5/0.0	2000/4.5/0.0	2000/3.0/0.0	...	1800/3.5/0.5	1800/3.5/0.0	1800/4.0/0.0
BT-Settl 2013	J	2400/3.0/0.0	1700/5.0/0.5	1800/4.5/0.5	1800/4.5/0.5	1800/4.5/0.5	1800/4.5/0.5	1900/4.0/0.5
BT-Settl 2013	H	2400/3.0/0.0	1800/4.5/0.5	1800/4.5/0.5	1800/4.5/0.5	1800/4.5/0.5	1800/4.5/0.5	1800/4.5/0.5
BT-Settl 2013	K	2400/3.0/0.0	1800/4.5/0.5	1800/4.5/0.5	1800/4.5/0.5	1800/4.5/0.5	1800/4.0/0.0	1800/4.0/0.0
BT-Settl 2013	JHK	2400/3.0/0.0	1800/4.5/0.5	1800/4.5/0.5	1800/4.5/0.5	1800/4.5/0.5	1800/4.0/0.0	1800/4.5/0.0
BT-Settl 2013	SED	2100/3.0/0.0	1900/4.0/0.5	1800/4.5/0.0	...	1800/3.5/0.5	1800/3.5/0.0	1800/4.0/0.0

pseudocontinuum in the H band.

The fit of the J, H, and K band spectra do not reveal a clear correlation between the spectral type and the temperature when the 2010 release of the models is used. The best fit temperatures can vary by up to 500 K from band to band. The 1.1-2.5 μm spectra are also fitted by models at lower temperatures, with differences of 500 K. The spread in effective temperature is reduced to 200 K with the 2013 models. Nevertheless, the solutions found fitting the 1.1-2.5 μm spectrum of the objects provides a reasonable fit in the individual bands with both models.

The reduced scatter in effective temperatures found with the 2013 release of the models also reflects the overall better quality of the fit provided by these models. The BT-Settl 2010 models reproduce better the spectra than the 2013 models when solarmetallicity models are considered. These behaviors are closely related to the dust that is allowed to form and is sustained in the atmospheres of both models. We discuss these differences in Section 4.5.1.

We decided to further test the models by comparing their predictions to the 1-5 μm spectral energy distributions of the objects.

4.4.2 SPECTRAL ENERGY DISTRIBUTIONS

We built the spectral energy distributions (SED) of the sources using published photometry from the 2MASS (J, H, K bands; $\lambda_{ref} = 1.235, 1.662, \text{ and } 2.159 \mu\text{m}$; Cutri et al. 2003) and WISE (W1, $\lambda_{ref} = 3.4 \mu\text{m}$; W2, $\lambda_{ref} = 4.6 \mu\text{m}$; Cutri & et al. 2012) sky surveys. The sources also have W3 ($\lambda_{ref} = 12 \mu\text{m}$) and W4 ($\lambda_{ref} = 22 \mu\text{m}$) WISE photometry. Nevertheless, we refrained from accounting for this photometry in the fit since the sources were not detected at a good S/N (> 8) in the WISE images. We excluded Cha 1305 from this analysis since the SED of this source has a strong excess (Allers et al. 2006b). The optical photometry, available for some objects, is not included in the fit because the models are known to

be inaccurate at these wavelengths (see Bonnefoy et al. 2013a).

The infrared photometry was converted to fluxes using tabulated zero points (Cohen et al. 2003a; Jarrett et al. 2011).

We generated synthetic fluxes from the BT-Settl 2010 and 2013 model grids in the passbands corresponding to the available photometry of the sources. The synthetic fluxes (F_λ) are provided per square centimeters of the stellar surface. The synthetic SEDs were then normalized to the object apparent fluxes by scaling a dilution factor that minimized the χ^2 of the fit. This dilution factor corresponds to R^2/d^2 , in which R and d are the radius and distance of the source, respectively.

The best-fit atmospheric parameters corresponded to the minimum χ^2 of the fit found for all possible combinations of atmospheric parameters in the grid of models. These parameters are reported in Table 5.9. The corresponding spectra are shown in Figure 4.12. χ^2 maps indicate that for most of the objects the fit is sensitive to T_{eff} only. We estimate errors of $^{+300}_{-100}$ K for DENIS 1245, and ± 100 K for the remaining targets with the BT-Settl 2013 models. We also find errors of $^{+100}_{-500}$ K for 2M2213 and 2M2322, and ± 200 K otherwise for the BT-Settl 2013 models. These errors are based on 5σ contours in the χ^2 maps. Both models yield similar effective temperatures (± 200 K). This is not surprising since differences between the models are expected to vanish at the spectral resolution corresponding to the broadband filters considered here. This also indicates that the errors are conservative.

Semiempirical radii R can be derived for the objects with known distances d from the normalization factor R^2/d^2 used to scale the model SED to the flux of the object. This is the case for EROS J0032 and DENIS 1245 (see Section 4.5.2). We therefore derive $R = 0.9 \pm 0.2 R_{Jup}$ for EROS J0032 and $R = 2.4 \pm 0.6 R_{Jup}$ for DENIS 1245 from the two sets of models. We compare these values to predictions from evolutionary models in Section 4.5.2.

The SED fit confirms the effective temperatures found from the near-infrared spectra. Two objects (2M2322, and 2M2126) have best-fit temperatures which disagree with those found from the fit of the BT-Settl 2010 models to the 1.1-2.5 μm spectra. We selected a subgrid of synthetic spectra corresponding to the set of atmospheric parameters producing the best fit of the SED within a 5σ confidence level. We identified the spectrum from this sub-grid producing the best fit of the 1.1-2.5 μm spectra of the targets, and displayed them in Figure 4.13. The best fits are found for low surface gravities, therefore further confirming results from the empirical analysis. Nevertheless, the comparison demonstrates that the models do not successfully reproduce the global spectral slope at these wavelengths as well as the pseudocontinuum in the H band. We reach similar conclusions for DENIS 1245, whose fit also indicates a mismatch of the overall spectral slope by the models if reduced (3σ) errors are considered on the temperature derived from the SED. We discuss possible explanations for the nonreproducibility of the models in the following section.

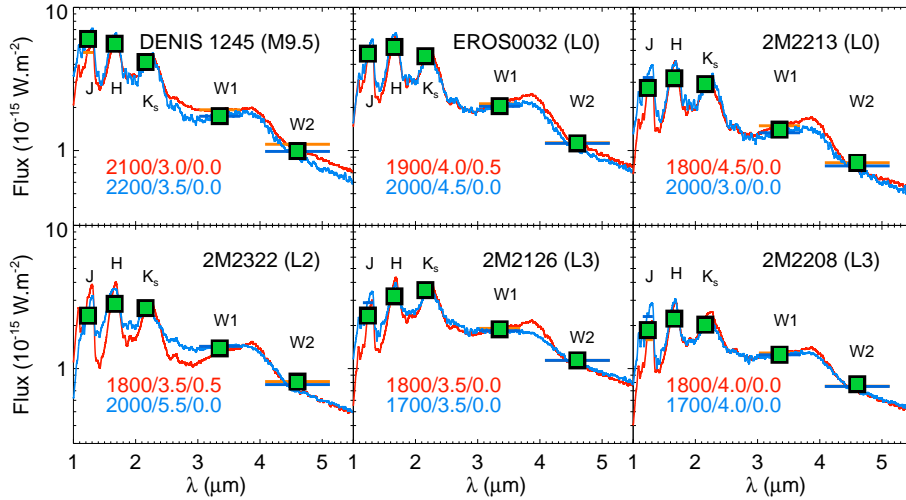


Figure 4.12: Fit of the spectral energy distribution of five sources of the target sample (green squares) without noticeable excess emission by BT-Settl 2010 (blue) and BT-Settl 2013 (red) synthetic fluxes (laying bars). The corresponding best-fit spectra are overlaid.

4.5 DISCUSSION

4.5.1 BEHAVIOR OF ATMOSPHERIC MODELS

The atmospheric models yield atmospheric parameters that are mostly consistent with our empirical analysis. All of the L_{γ} objects have surface gravities expected for young objects. The BT-Settl 2013 models converge toward an overall higher surface gravity for EROS J0032.

Surprisingly, all spectra but that of DENIS 1245 are well reproduced by a single BT-Settl 2013 synthetic spectrum with $T_{eff}=1800$ K, $\log g = 4.5$, and $M/H = +0.5$. Models at higher metallicity used in this analysis had not been extensively tested and suffer from increased numerical instability due to the dust content in these atmospheres that is several times greater. Nonconvergent models can indeed have an anomalous dust content, which can sometimes produce spectra that match the observations well. We found nonetheless that a neighboring spectra with $T_{eff} = 1700$ K and $\log g = 4.5$ is affected by this problem. Therefore, it is possible that our temperature estimate could be biased by 100 K given our inability to check if a convergent model at these T_{eff} 's can provide a better fit. We also verified that the features of the model spectrum at $T_{eff} = 1800$ K are coherent with those found in model spectra for other neighboring T_{eff} and $\log g$.

The near-infrared spectral slopes, and therefore results from the fits of the ISAAC spectra, are mostly tied to the dust content in the atmosphere. Solutions at high metallicity can then be interpreted as if the 2013 solar metallicity models were not forming enough dust in the atmosphere compared to the 2010 models.

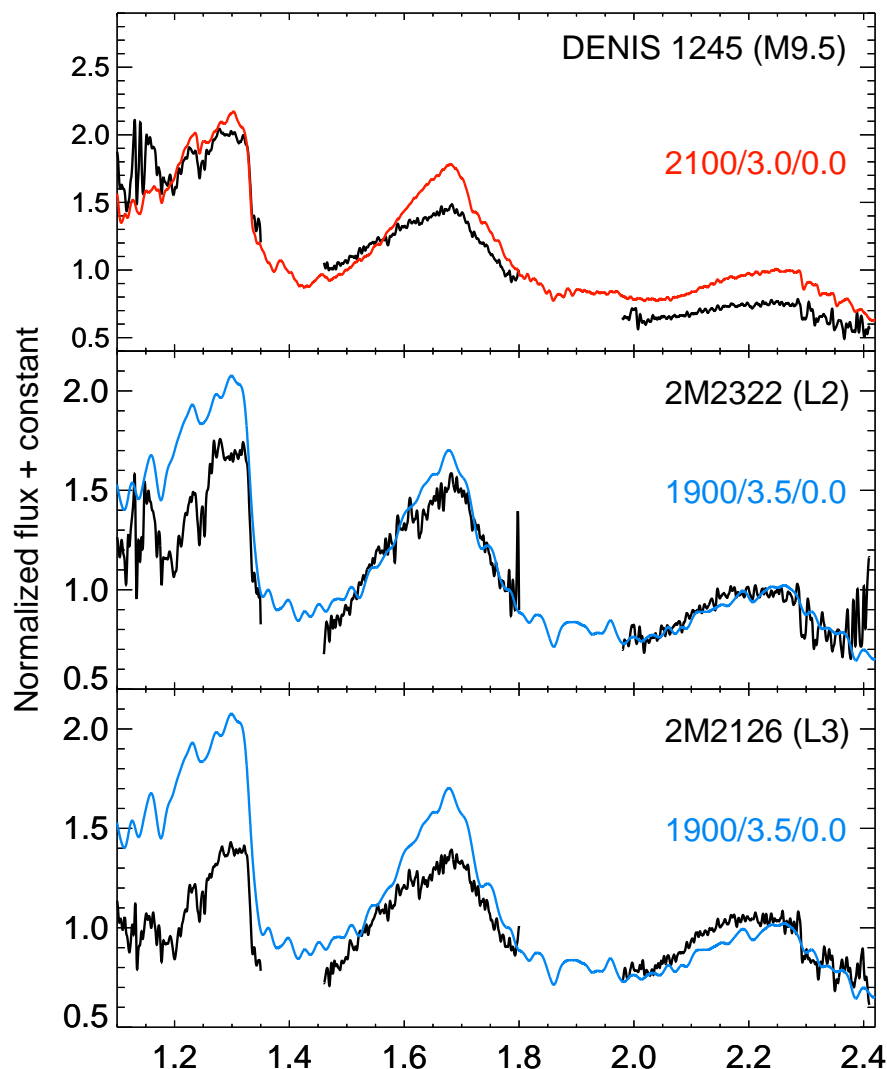


Figure 4.13: ISAAC spectra (black) smoothed at $R=300$ compared to best-fit BT-Settl 2010 (blue) and for BT-Settl 2013 (red) spectra with previously determined effective temperature inferred from the SED fit for objects for which an independent fit of the $1.1\text{-}2.5\ \mu\text{m}$ does not yield the same effective temperature.

This lack of dust could also explain why the models do not reproduce the shape of the pseudocontinuum in the H band well. The mismatch found in the BT-Settl 2010 models (Figure 4.13) is also indicative of a lack of dust grains at high altitude/low optical depths in the cloud model. The problem may be solved with an ongoing revision of the models. The current version of the code uses a mixing length parameter (which parametrizes the vertical size of the convection cells) of 2 throughout the regime from M dwarfs to brown dwarfs. The new RHD simulations rather indicate that this parameter should be set to lower values. In addition, the grain growth in the 2013 models was artificially suppressed, as it was linked to the assumed

Table 4.6: Adopted atmospheric parameters and bolometric luminosity

Object	T_{eff} [K]	$\log g$	$\log_{10}(L/L_{\odot})$ (a)
DENIS J1245	2200 ± 200	3.0 ± 0.5	-3.02 ± 0.21
EROS J0032	1900 ± 200	4.5 ± 0.5	-3.93 ± 0.11
2M 2203	1800 ± 100	4.0 ± 0.5	...
Cha 1305	1800 ± 100	4.0 ± 0.5	-3.13 ± 0.08
2M 2322	1800 ± 100	4.0 ± 0.5	...
2M 2126	1800 ± 100	4.0 ± 0.5	...
2M 2208	1800 ± 100	4.0 ± 0.5	...

(a) Recomputed based on the bolometric corrections of young M9.5 and L0 dwarfs reported in Todorov et al. (2010).

availability of nucleation seeds. The next version of the models will treat growth by coagulation in a more consistent fashion and could, in principle, produce thicker clouds.

The fit of the SED is less influenced by localized errors in the models because of the extended spectral coverage and the lower resolution of the fit, set by the narrowest filter. If we assume that the SED fits are more reliable, we confirm the quick drop of the effective temperature at the M/L transition discovered for young optically-classified dwarfs (GSC 08047-00232 B, OTS 44, KPNO-Tau 4) by Bonnefoy et al. (2013a). The effective temperature remains nearly constant for the L0-L3 γ dwarfs of the sample. These temperatures are close to those of other young L-type low-mass companions AB Pic b (Bonnefoy et al. 2010), 1RXS1609b (Lafrenière et al. 2008b, 2010b), GJ 417 B (Bonnefoy et al. 2013a), β Pictoris b (Bonnefoy et al. 2013c), G196-3B (Zapatero Osorio et al. 2010), and CD-35 2722B (Wahhaj et al. 2011). This further suggests that β Pictoris b is an early-L dwarf.

4.5.2 REVISED PROPERTIES

We combine results from our analysis of the SED and the 1.1-2.5 μm ISAAC spectra to derive final estimates for the objects and we report them in Table 4.6. We prioritized the solutions derived from the SED fit with the BT-Settl 2013 models for the final estimate of the T_{eff} . The values of the surface gravity correspond to the most frequent solutions found from the fit of the J, H, K, and JHK band spectra. The error bars were derived on a case-by-case basis from the dispersion of the atmospheric parameters.

These new parameters and complementary material found in the literature are used to rediscuss the properties of DENIS J1245, EROS J0032, Cha 1305, and 2M2213.

Table 4.7: Physical properties of the objects with known distance and age.

Object	Age (Myr)	M from L/L _⊙ (a) (M _{Jup})	M from T _{eff} (a) (M _{Jup})
DENIS 1245	10 ⁺¹⁰ ₋₇	16 ⁺¹⁹ ₋₇	16 ⁺⁹ ₋₁₀
Cha1305	4 ± 2	12 ⁺³ ₋₄	7 ± 2
EROS J0032	30 ⁺²⁰ ₋₁₀ ?	12 ± 2	13 ⁺¹⁵ ₋₁
EROS J0032	120 ± 20 ?	30 ± 6	33 ± 7
EROS J0032	21 ⁺⁴ ₋₁₃	11 ⁺¹ ₋₄	13 ⁺² ₋₄

(a) Derived from the evolutionary models of [Chabrier et al. \(2000\)](#).

4.5.2.1 DENIS-P J124514.1-442907 (TWA 29)

The object DENIS-P J124514.1-442907 was identified as a probable member of the TW Hydrae association ([Kastner et al. 1997](#)) by [Looper et al. \(2007\)](#). Membership was initially based on estimated distance, sky position relative to known association members, proper-motions, H α emission, and features indicative of low surface gravity in low-resolution (R~120), near-infrared (0.94-2.5 μ m) and medium-resolution (R~1800), red-optical spectra of the source. [Looper et al.](#) derived spectral types M9.5 and M9pec, respectively, from their optical and near-infrared spectra. [Manara et al. \(2013b\)](#) derived a comparable range of spectral types (M7.2-L0.8) by calculating spectral indices in an 0.58-2.4 μ m medium-resolution (R~3500) spectrum of DENIS J1245. These spectral type estimates are in agreement with our value (Table 4.3).

The membership of DENIS J1245 in the TW Hydrae association was revisited by both [Schneider et al. \(2012\)](#) and [Weinberger et al. \(2013a\)](#). [Schneider et al.](#) used revised proper motion measurements to assess the membership in the context of other proposed members and found that membership was highly likely, despite the lack of a measured parallax at the time. [Weinberger et al.](#) measured a parallax and new proper motions from dedicated, multi-epoch photometry and found that the overall kinematics and Galactic position of the brown dwarf were consistent with the distribution of other higher-mass members of the association.

We used the online BANYAN tool of [Malo et al. \(2013\)](#) to calculate a membership probability based on the position, proper motion, and measured parallax. The Bayesian analysis provides a 95% probability of the brown dwarf being a member of the TW Hydrae association based only on the available kinematics (i.e., not considering the evidence for youth). We also use the methods of [Lépine & Simon \(2009\)](#) and [Schlieder et al. \(2010, 2012\)](#) to constrain group membership. We calculated ϕ , the angle between the source proper motion vector and that expected for the average motion of kinematic moving group members at its position, and d_{kin} , the source's distance assuming it is a group member. We checked these values for each of the young, kinematic groups described in [Torres et al. \(2008\)](#). We found ϕ for DENIS J1245 was smallest when calculated for both the β Pictoris moving group and the TW Hydrae association, $\sim 5.5^\circ$.

This angle is typically $\lesssim 10^\circ$ for well established group members. The d_{kin} predicted for both moving groups was also very similar, ~ 95 pc, and generally consistent with the 79 ± 13 pc distance measured by Weinberger et al. (2013a). However, the Galactic XYZ distances of the brown dwarf are most consistent with other members the TW Hydrae association, particularly the positive Z distance. These results are consistent with previous kinematic studies, and when combined with previous evidence for youth and the spectral features indicative of verylow surface gravity in our ISAAC spectrum, indicate DENIS J1245 is a very strong candidate for TWA membership. Designation as a true member will require an accurate RV measurement.

Witte et al. (2011) compared their DRIFT-PHOENIX model spectra to the near-infrared spectrum ofLooper et al. (2007) to derive $T_{eff}=1900$ K, $\log g = 4.5$ and $[M/H] = 0.0$. Our estimates of these physical parameters are consistent with these values if we consider a 100 K error on their measurements, corresponding to the sampling in effective temperature of their model template grid. Nevertheless, they disagree with the temperature derived from the fit of the 1.1-2.5 μm only. Our estimates of the effective temperature (from the SED, or the spectra) are in good agreement with the temperature ($T_{eff} = 2300$ K) derived from the extension (Briceño et al. 2002) of the spectral type temperature conversion scale of Luhman (1999) and Luhman et al. (2003). We derive a mass of $16_{-10}^{+9} M_{Jup}$ for DENIS J1245 by comparing our temperature (reported in Table 4.6) to predictions of the DUSTY evolutionary models (Chabrier et al. 2000) for an age of 10_{-7}^{+10} Myr (Barrado y Navascués 2006).

We used the parallax measurement of Weinberger et al. (2013b) and the BC_K for young M9.5 dwarfs derived by Todorov et al. (2010) to estimate the bolometric luminosity (Table 4.7) of the source. This luminosity corresponds to a predicted mass consistent with that derived from T_{eff} (see Table 4.7). We thus confirm that to date, DENIS J1245 is the lowest mass isolated object proposed to be a member of the TW Hydrae association. The semiempirical radius derived in Section 4.4.2 is consistent with evolutionary model predictions (Chabrier et al. 2000) for the estimated age of the object.

4.5.2.2 EROS-MP J0032-4405

The object EROS-MP J0032-4405 was discovered by Goldman et al. (2010). Martín et al. (1999) adopted a spectral type of L0 from the analysis of an optical spectrum and identified strong Li 6708 Å absorption. The detection of Li constrained the mass to $M \leq 50 M_{Jup}$ and the age to be younger than ~ 0.5 Gyr. Goldman et al. (2010) used NG-Dusty models to estimate a temperature of $T_{eff} = 1850 \pm 150$ K, comparable to our estimate from SED fitting. Cruz et al. (2009b) classified this object as verylow gravity L0 γ type and estimated a spectroscopic distance of $d_{sp}=41 \pm 5$ pc. Allers & Liu (2013) also presented a low-resolution near-infrared spectrum and used their index based methods to classify it as L0 VL-G (very low gravity). Accurate proper motions and a parallax of 38.4 ± 4.8 mas were presented in Faherty et al. (2012b).

Our index based analysis of our ISAAC spectrum provided a spectral type consistent with the L0 determined by Cruz et al. (2009b) and Allers & Liu (2013). However, the gravity sensitive spectral features in our medium-resolution spectrum provide a slightly different view of the brown dwarf's age. Figures 5

and 6 show that the gravity sensitive K I lines and FeH band in the J -band and the shape of the H -band continuum are consistent with a surface gravity that is only slightly weaker than typical field brown dwarfs of similar spectral type. These features are more suggestive of an intermediate surface gravity and thus an older age than the previous optical and near-infrared spectra. Since our knowledge of how dust and low-surface gravity affect individual spectral features and overall spectral morphology at different wavelengths and spectral resolutions is incomplete, it is difficult to assess this discrepancy. As shown for two proposed L-type members of the AB Doradus moving group in Allers & Liu (2013), even the spectra of brown dwarfs at the same purported age and temperature exhibit features consistent with different surface gravities.

Cruz et al. (2009b) showed that the sky position of EROS J0032 and many other young, field dwarfs were coincident with known members of young kinematic groups. To follow up these preliminary suggestions, we followed the same procedures as described for DENIS J1245 to investigate possible membership of EROS J0032 in kinematic moving groups. Using only the available proper motions and parallax, the Malo et al. (2013) online tool provides $\sim 92\%$ membership probability in the Tucana/Horologium association (Tuc/Hor), $\sim 8\%$ membership probability in the AB Doradus moving group (AB Dor), and $\sim 1\%$ probability in the β Pictoris moving group (β Pic) and the field. However, the potential membership of EROS J0032 in a young moving group hinges on its radial velocity (RV).

We illustrate this in Fig. 4.14, where we show projections of the six-dimensional Galactic kinematics³ of EROS J0032 for a range of possible RVs ($[-30, 30]$ km s⁻¹). The figure reveals that the kinematics of the brown dwarf are a relatively good match to both the Tuc/Hor and β Pic groups for RVs between ~ 5 -10 km s⁻¹. The object EROS J0032 is also close to the AB Dor group distribution for RVs ~ 15 -20 km s⁻¹, but remains a $>4\sigma$ outlier in the (UV) plane. EROS J0032 is consistent with the (XYZ) of any of these groups. To complete the kinematic analysis, we also calculated $\phi = 5.3^\circ$, $\phi = 0.9^\circ$, $\phi = 19.5^\circ$ when comparing the brown dwarf's proper motions to the Tuc/Hor, AB Dor, and β Pic groups, respectively. The d_{kin} 's calculated for the groups are also very comparable: 32 pc for Tuc/Hor, 37 pc for AB Dor, and 26 pc for β Pic. All of these distances are broadly consistent with the measured parallax distance of 26.0 ± 3.3 pc, but the match to β Pic is the best. Thus, we conclude that the kinematics of EROS J0032 are most suggestive of possible membership in either the Tuc/Hor or β Pic groups, but without a measured RV, definitive membership cannot be assigned.

For completeness, we estimate the mass of EROS J0032 by comparing our derived effective temperature to DUSTY evolutionary model predictions for two different age ranges: 20 - 40 Myr for possible Tuc/Hor or β Pic membership and 130 ± 20 Myr for possible AB Dor membership (Zuckerman et al. 2001; Barenfeld et al. 2013). If the brown dwarf is a member of β Pic, its mass is comparable to those of directly imaged planets (see Table 4.7).

³ $UVWXYZ$, where U , V , and W are Galactic velocities and X , Y , and Z are Galactic distances. U and X are positive toward the Galactic center, V and Y are positive in the direction of the Sun's motion around the Galaxy, and W and Z are positive toward the north Galactic pole. The sun lies at $(UVWXYZ) = (0,0,0,0,0)$.

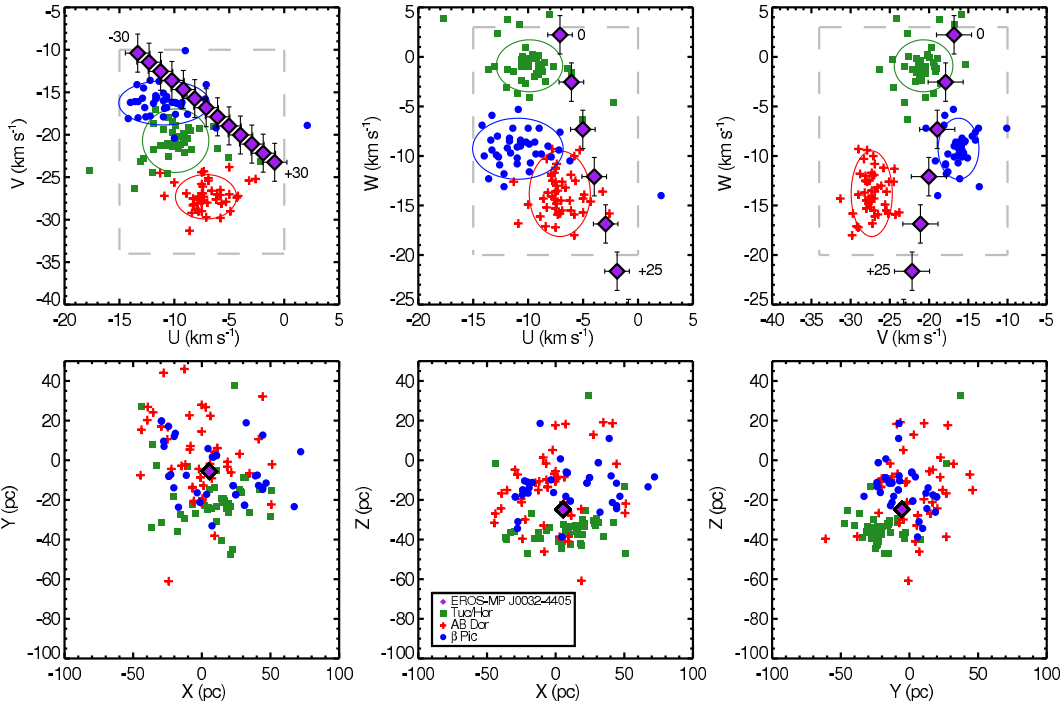


Figure 4.14: Projections of the 6D Galactic kinematics of EROS J0032 compared to the young Tucana/Horologium, AB Doradus, and β Pictoris kinematic groups. EROS J0032 is presented by a violet diamond with associated error bars. The multiple points represent different possible values of the radial velocity (RV), ranging from -30 km s^{-1} to $+30 \text{ km s}^{-1}$ in increments of 5 km s^{-1} . The young kinematic groups are designated in the figure legend. Top panels: Projections in (UVW) Galactic velocity. The colored ellipses designate the 2σ dispersion of the average velocities of each group from Malo et al. (2013). EROS J0032 is most consistent with the Tuc/Hor and β Pic groups for RVs between ~ 5 and 10 km s^{-1} . Bottom panels: Projections of the (XYZ) Galactic distance. EROS J0032 is consistent with the distributions of all three young groups. For reference, we also plot the Galactic velocity space occupied by most young stars in the solar neighborhood as a dashed, grey box (Zuckerman & Song 2004).

4.5.2.3 CHA J130540.8-773958

Our new effective temperature determination for Cha J1305 falls in the same range as the temperatures of 1-3 Myr old M9.5-L0 objects OTS 44 (Luhman et al. 2004), KPNO Tau 4 (Briceño et al. 2002), and Cha J110913-773444 (Luhman et al. 2005b). This is consistent with the observed similarities between the spectrum of OTS 44 and the low-resolution ($R \sim 300$) near-infrared spectrum of Cha 1305 presented by Allers et al. (2007). The optical spectral type ($L0 \pm 2$) derived by Jayawardhana & Ivanov (2006) is also consistent with the near-infrared spectral type.

We recomputed the luminosity of Cha 1305 and report it in Table 4.7. This luminosity is based on the BC_K of young L0 dwarfs (Todorov et al. 2010), the K band magnitude of the source, corrected for an $A_V = 3$ mag (Allers et al. 2007; Spezzi et al. 2008), and an associated distance of $178 \pm 18 \text{ pc}$ for the Chameleon

II star forming cloud (Whittet et al. 1997). We compared the temperature and luminosity of Cha J1305 to Chabrier et al. (2000) evolutionary tracks and retrieved a mass of 5-15 M_{Jup} for a Chameleon II age of 4 ± 2 Myr (Spezzi et al. 2008). This mass is consistent with the previous mass estimate presented by Allers et al. (2007).

4.5.2.4 2MASS J22134491-2136079

2MASS J22134491-2136079 was identified as a peculiar L0 type object with probable low gravity features (Cruz et al. 2007). This gravity classification was based on the strength of VO bands and alkali doublets in the optical. However, H α emission was not detected. Kirkpatrick et al. (2008) estimated an age of less than ~ 100 Myr via visual comparison to the optical spectra of other brown dwarfs with known ages. Kirkpatrick et al. (2008) considered the estimated age and sky position of 2M 2213 to suggest that it is a possible member of the β Pictoris moving group. Cruz et al. (2009b) estimated a distance of 54 ± 7 pc using the M_J -Spectral type relation from Cruz et al. (2003). Allers & Liu (2013) classified 2M 2213 as spectral type L0 with very low surface gravity from a low-resolution ($R \sim 100$) IRTF/SpEx spectrum. This classification is at odds with the L2pec near-infrared spectral type of Marocco et al. (2013a), likely because Marocco et al. (2013a) only compare the spectrum of the source to those of mature field dwarfs.

We report here the first estimate of the temperature of the object using atmospheric models, and find atmospheric parameters that confirm the low surface gravity of the object. To further investigate possible young kinematic group membership, we use the proper motions measured by Faherty et al. (2009a) to apply the same tests of group membership used for DENIS 1245 and EROS J0032. The BANYAN Bayesian analysis tool provides ambiguous probabilities for group membership: $\sim 30\%$ β Pictoris, $\sim 20\%$ Tuc/Hor, and $\sim 50\%$ field. The angle ϕ is also $< 10^\circ$ for many of the kinematic groups discussed in Torres et al. (2008). The photometric distance estimated by Cruz et al. (2009b) could be used to potentially rule out membership in several groups, but a parallax measurement is preferred given the young age of 2M 2213. Thus, the currently available data do not allow for constraints on 2M 2213's possible kinematic group membership. The topic should be revisited once RV and parallax measurements are available for this young brown dwarf.

4.6 CONCLUSIONS

We obtained and analyzed seven VLT/ISAAC medium-resolution ($R \sim 1500$ -1700) spectra of M9.5-L3 dwarfs classified at optical wavelengths and showing indications of low surface gravity. We built an age sequence of M9.5 objects that allow us to pinpoint age-sensitive and gravity-sensitive features at medium-resolving powers. The comparison of our spectra to those of young reference brown dwarfs and their companions, and of mature field dwarfs confirm that our objects have peculiar features in the near-infrared indicative of low surface gravities and young ages. We also confirm the youth of our objects by calculating the equivalent widths of their KI lines and comparing these values per spectral type with the

values obtained for young reference brown dwarfs and companions and mature field dwarfs. We derived near-infrared spectral types based on dedicated spectral indices. These spectral types are in agreement with the optical classification, and confirm the coherence of the classification method. The analysis revealed that the L2 γ object 2MASS J2322 provides a good match to the spectrum of the young planetary mass companion 1RXS J160929.1-210524b.

The spectra and SEDs of the objects can be reproduced by the 2010 and 2013 BT-Settl atmospheric models. The 2013 release of the models simultaneously fit the spectra and the SED for the same temperatures at all wavelengths. L0-L3 γ dwarfs have nearly equal temperatures at around 1800 K. Nevertheless, we identify that:

- the 2010 models do not reproduce the 1.1-2.5 μm spectral slope of some L2-L3 objects.
- the H band shape is not well reproduced by the BT-Settl 2013 models at solar metallicity. The problem disappears when new, but not well-tested, models at super-solar metallicity are used, but these models remain mostly untested.

Currently, all these discrepancies point out a lack of dust in the cloud models. The next version of the BT-Settl models will modify the treatment of the vertical mixing and of grain growth processes. These new models are expected to produce thicker clouds, and may solve the issues revealed by the ISAAC spectra.

The spectra of the objects will help to confirm the membership of photometrically-selected candidates in star-forming regions. Within the next few years, surveys on the next generation of planet imaging instruments such as the Spectro-Polarimetric High-contrast Exoplanet REsearch (SPHERE) at VLT, the Gemini Planet Imager (GPI) at Gemini South, the Subaru Coronagraphic Extreme AO Project (ScEXAO) at Subaru, and the Large Binocular Telescope mid-infrared camera (LMIRCam) at LBT should provide a sample of a few dozen young companions. Several planets similar to β Pictoris b should be unearthed and fall in the same temperature range as our objects. Therefore, our spectra will serve as precious benchmarks for the characterization of the physical and atmospheric properties of these companions.

Note added in proof: While this work was in peer review, [Gagné et al. \(2013\)](#) published a revised version of the BANYAN tool (BANYAN II) and presented a detailed analysis of two of our targets. Using BANYAN II, they found a 93.3% probability that DENIS-P J124514.1-442907 (TWA 29) is a member of the TW Hydrae association and a 91.8% probability that EROS-MP J0032-4405 is a member of the β Pictoris moving group. These new results are consistent with ours as presented in section 4.5.2.

4.A PROPERTIES OF THE SPECTRA OF YOUNG COMPANIONS

We summarize in Table 4.8 the main characteristics of the spectra of young companions found in the literature and used in our empirical analysis. We did not report proposed spectral classes for these companions given the inhomogeneous classification scheme adopted in the literature.

Table 4.8: Characteristics of the young companions spectra

Name	Age (Myr)	λ_{min} (μm)	λ_{max} (μm)	R	Reference ^a
2MASS J12073346-3932539 A	8	1.1	2.5	1500-2000	1
AB Pic b	30	1.1	2.5	1500-2000	1, 2
CT Cha b	1-3	1.1	2.5	1500-2000	1
DH Tau b	1-3	1.1	2.5	1500-2000	1
G1 417 B	80-250	1.1	2.5	1500-2000	1
GSC 08047-00232 B	30	1.1	2.5	1500-2000	1
HR7329 B	12	1.1	2.5	1500-2000	1
TWA 5B	8	1.1	2.5	1500-2000	1
TWA 22A	12	1.1	2.5	1500-2000	1
TWA 22B	12	1.1	2.5	1500-2000	1
USCO CTIO 108B	3-11	1.1	2.5	1500-2000	1
1RXS J235133.3+312720 B	50-150	0.8	2.5	250-1200	3
2MASS J01225093-2439505 B	10-120	1.48	2.38	3800	4
GSC 06214-00210 b	3-11	1.1	1.8	3800	5
HD203030 b	130-400	2.0	2.6	2000	6
1RXS J160929.1-210524 b	3-11	1.15	2.4	6000-1300	7, 8
2MASS J12073346-3932539 b	8	1.1	2.5	1500-2000	9
CD-35 2722 B	100	1.15	2.40	5000-6000	10
G196-3B	100	1.1	2.4	2000	11
GQ Lup b	1-3	1.1	2.5	2000-4000	12
GQ Lup b	1-3	1.164	2.4	5000	13
HN Peg b	100-500	0.65	2.56	75	14
HR8799 b	30	1.48	2.36	60	15
HR8799 c	30	1.965	2.381	4000	16
SDSSJ224953.47+004404.6AB	100	0.8	2.5	150	17
TWA 8B	8	0.8	2.42	2000	11
TWA 11C	8	0.95	2.42	2000	11
AB Dor C	75-175	1.48	2.5	1500	18

^aReferences: 1, Bonnefoy et al. (2013a); 2, Bonnefoy et al. (2010); 3, Bowler et al. (2012); 4, Bowler et al. (2013); 5, Bowler et al. (2011); 6, Metchev & Hillenbrand (2006); 7, Lafrenière et al. (2008b); 8, Lafrenière et al. (2010b); 9, Patience et al. (2010); 10, Wahhaj et al. (2011); 11, Allers & Liu (2013); 12, Seifahrt et al. (2007); 13, Lavigne et al. (2009); 14, Luhman et al. (2007); 15, Barman et al. (2011); 16, Konopacky et al. (2013); 17, Allers et al. (2010); 18, Close et al. (2007).

4.B BEST MATCHES OF EROS J0032, 2M 2213, 2M 2126, AND 2M 2208 WITH LIBRARY SPECTRA.

We present the result of the best matches after performing the empirical comparison of EROS J0032, 2M 2213, 2M 2126, and 2M 2208 spectra with library spectra in Section 4.3.2.

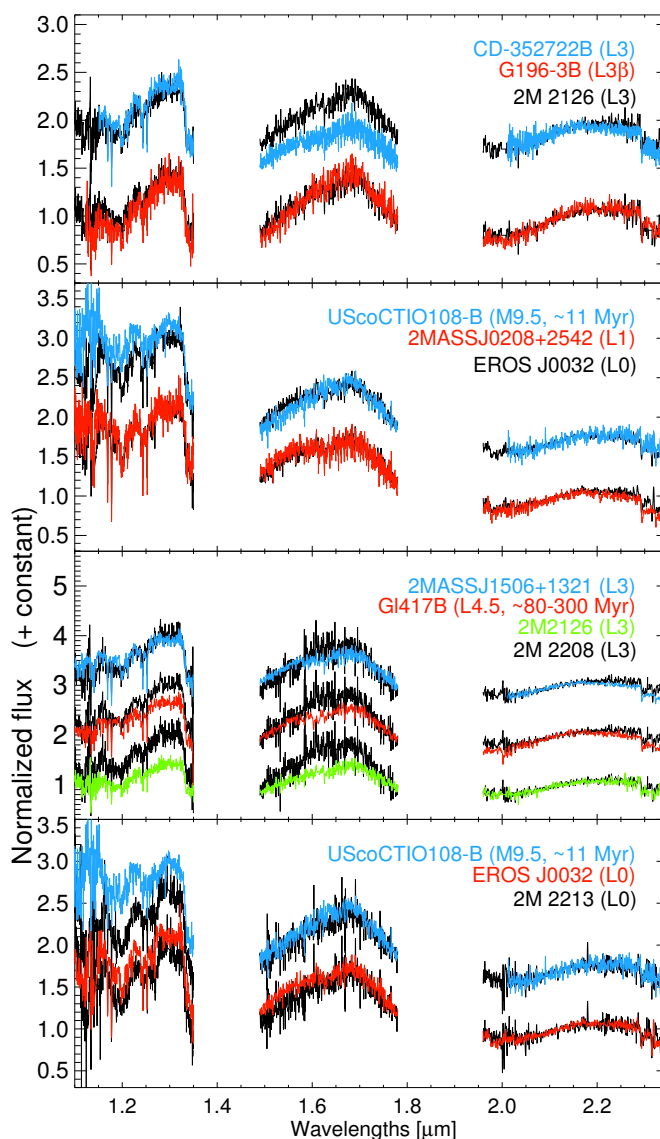


Figure 4.15: Best matches of the 1.1-2.38 μm spectra of EROS J0032, 2M 2213, 2M 2126, and 2M 2208 with library spectra.

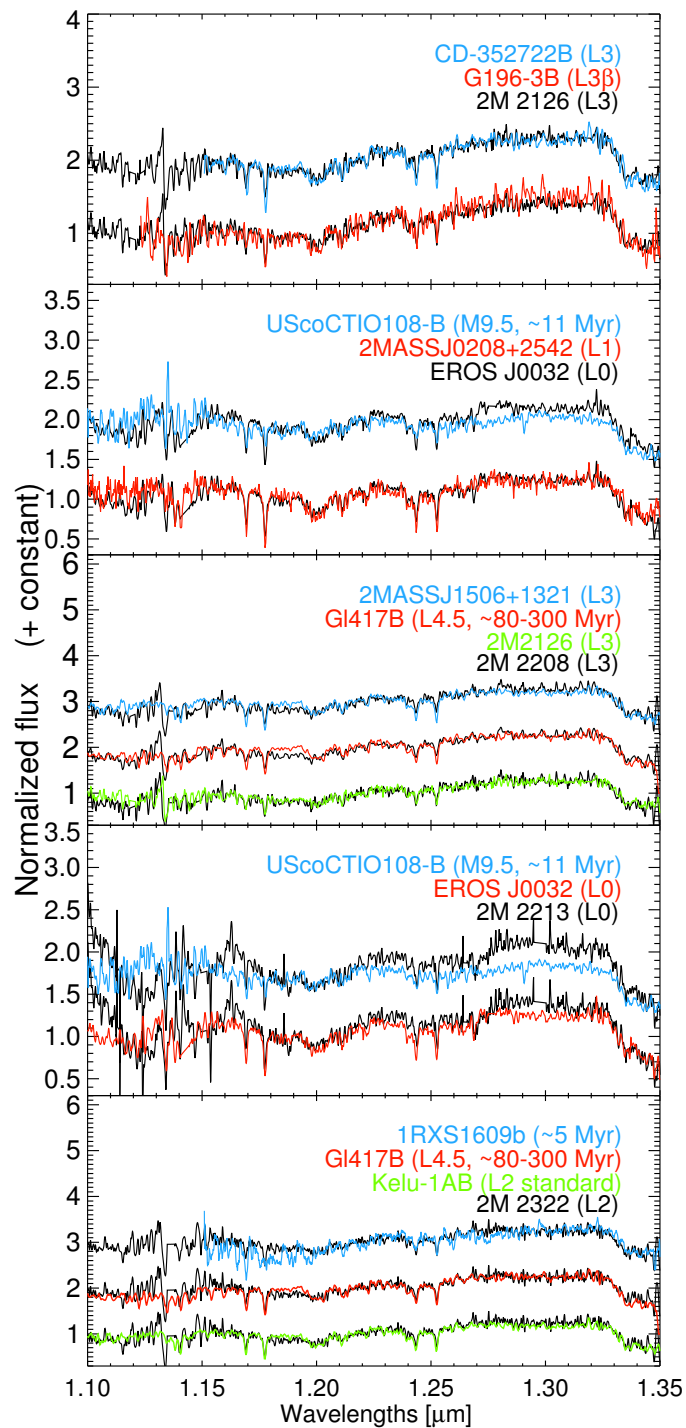


Figure 4.16: J band of best matches of the spectra of EROS J0032, 2M 2213, 2M 2126, and 2M 2208 with library spectra.

HUNTING FOR BROWN DWARF BINARIES WITH X-SHOOTER*

5.1 INTRODUCTION

Stars are believed to be born in nurseries of several objects. After childhood they leave their birth place and settle on the main sequence. A majority of stars remain in binary or hierarchical systems. Multiplicity provides constraints on fundamental parameters, such as dynamical masses, essential to test atmospheric models. It is well known that the binary fraction decreases when decreasing mass. For L- and T- brown dwarfs, the binary fraction is estimated of about 20% (see Section 1.2.3).

Burgasser *et al.* (2007) claimed that due to limitations of high resolution imaging methods, we are missing brown dwarf binary systems with separations smaller than ~ 3 au. Binary systems with smaller separations than ~ 3 au can be only found either using radial velocity methods, searching for overluminous targets or studying the peculiar spectral characteristics of their spectra.

Brown dwarfs with different classification in the optical and in the near-infrared or with peculiar spectra are potential candidates to be brown dwarf binary systems. In this Chapter, we aim to find unresolved brown dwarf binary systems in a sample of 22 objects that satisfied at least one of the criteria to be potential brown dwarf binary systems.

In Section 5.2 we detail the selection procedure for the candidates in our sample and we explain how the observations were performed, and the data reduction procedure. In Section 5.3 we perform an empirical analysis to search for L plus T, L plus L and T plus T unresolved brown

*This chapter is adapted from the paper: Manjavacas, E.; Goldman, B; Alcalá, J. M.; Zapatero-Osorio, M. R.; Béjar, V. J. S.; Homeier, D.; Bonnefoy, M.; Smart, R. L.; Henning, T.; Allard, F., 2014, submitted to *Astronomy & Astrophysics*.

dwarfs binary systems. We also compare our objects with trigonometric distances in a color magnitude diagram (CMD) with the L, L-T and T brown dwarfs published by Dupuy & Liu (2012a). Color-magnitude plots help to discover unresolved binaries and young brown dwarfs. We also calculate spectral indices following the method described in Burgasser et al. (2006, 2010) and Bardalez Gagliuffi et al. (2014a) to search for close binaries. In Section 5.4 we measure the equivalent width of alkali lines in the optical and in the near infrared for our objects and objects from the literature as a comparison. In Section 5.5 we test the BT-Settl 2014 atmospheric models investigating whether they reproduce our spectra over the optical and the near-infrared. In Section 5.6 we discuss the properties of the most remarkable objects of our sample. In Section 5.7 we update the binary fraction of very low mass objects. Finally, in Section 5.8 we summarize our results.

5.2 THE SAMPLE, OBSERVATIONS AND DATA REDUCTION

5.2.1 SAMPLE SELECTION

We selected a sample of 22 brown dwarfs found in the literature with optical spectral types between L3 and T7 which have discrepant optical and near-infrared classification, or, peculiar spectra. Optical subtypes are typically earlier than the near infrared subtypes. These objects are candidates for unresolved binaries. Furthermore, to calibrate our results and confirm the reliability of our method, we added some known brown dwarfs systems, LHS 102B (Golimowski et al. 2004a), formed by a L4.5 plus a L4.5, and SDSS J042348.56-041403.4 (Burgasser et al. 2005), formed by a L6±1 and a T2±1. Our list of targets and their physical properties taken from the literature are compiled in Table 5.1.

5.2.2 OBSERVATIONS AND DATA REDUCTION

Our targets were observed using X-Shooter (Wideband ultraviolet-infrared single target spectrograph) on the Very Large Telescope (VLT) between October 2009 and June 2010. X-Shooter covers a wavelength range between 300-2500 nm. The instrument is separated into three arms: UVB (300-550 nm), optical (550-1000 nm) and near-infrared (1000-2500 nm). It was operated in echelle slit nod mode, using the 1.6" slit for the UVB arm, and the 1.5" slit for the optical and the near-infrared arms. This setup provides resolutions of ~3300 in the UVB and NIR, and ~5400 in the VIS. We obtained an average signal to noise of ~30. Observations were performed at the parallactic angle to mitigate the effect of differential chromatic refraction. We moved the object along the slit between two positions following an ABBA pattern with a size of 6 arcsec.

Table 5.1: List of observed targets. Magnitudes are given in 2MASS system, except for object Gl 229B.

#	Name	J [mag]	H [mag]	K [mag]	d_{trig} (pc)	SpT OPT	SpT NIR	Remarks	Reference
1	LHS 102B	13.11±0.02	12.06±0.02	11.39±0.02	13.2±0.7	L5	L4.5	Binary	1, 2
2	2MASS J00361617+1821104	12.47±0.02	11.59±0.03	11.06±0.02	8.8±0.1	L3.5	L4	NR [a], V [b]	3, 4, 36
3	2MASS J00531899-3631102	14.45±0.02	13.48±0.03	12.94±0.02		L3.5	L4		5, 6
4	SIMP 01365662+0933473	13.46±0.03	12.77±0.03	12.56±0.02	6.0±0.1		T2.5		7, 8
5	2MASS J01443536-0716142	14.19±0.02	13.01±0.02	12.27±0.02		L5		Red	9, 10
6	2MASS J02182913-3133230	14.73±0.04	13.81±0.04	13.15±0.04		L3	L5.5		5,11
7	DENIS-P J0255.0-4700	13.25±0.02	12.20±0.02	11.56±0.02	4.9±0.1	L8	L9		12, 13, 35
8	2MASS J02572581-3105523	14.67±0.03	13.52±0.03	12.88±0.03	10.0±0.7	L8	L8.5		4, 5, 14
9	2MASS J03480772-6022270	15.32±0.05	15.56±0.14	15.60±0.02	7.9±0.2		T7		15, 16
10	2MASS J03552337+1133437	14.05±0.02	12.53±0.03	11.53±0.02	9.1±0.1	L5	L3	Y [d]	1, 17, 18, 19, 20, 37
11	SDSS J0423485-041403	14.47±0.02	13.46±0.03	12.93±0.03	13.9±2.1	L7.5	T0	Binary	1, 21, 33
12	2MASS J04390101-2353083	14.41±0.02	13.41±0.02	12.82±0.02	9.1±0.3	L6.5			11, 19
13	2MASS J04532647-1751543	15.14±0.03	14.06±0.03	13.47±0.03		L3pec		Y ? [d]	11, 14
14	2MASS J05002100+0330501	13.67±0.02	12.68±0.02	12.06±0.02		L4	L4		1, 22
15	2MASS J05395200-0059019	14.03±0.03	13.10±0.02	12.53±0.02	12.2±4.5	L5	L5	NR [a], V [b]	1, 4, 24
16	2MASS J06244595-4521548	14.48±0.02	13.34±0.02	12.59±0.02	11.9±0.6	L5pec	L5		1, 23
17	Gl 229B	13.97±0.03	14.38±0.03	14.55±0.03	5.8±0.4		T7pec	MP [c], Y [d]	33, 34, 35
18	2MASS J10043929-3335189	14.48±0.04	13.49±0.04	12.92±0.02	17.0±1.6	L4	L5		25, 26
19	2MASS J11263991-5003550	14.00±0.03	13.28±0.03	12.83±0.03		L4.5	L6.5	Blue L	27, 28, 29
20	2MASS J13411160-3052505	14.61±0.03	13.72±0.03	13.08±0.02		L2pec	L3		22
21	2MASS J18283572-4849046	15.18±0.05	14.91±0.06	15.18±0.14	11.9±1.1		T5.5		23, 31
22	2MASS J21513839-4853542	15.73±0.07	15.17±0.09	15.43±0.18	16.7±1.1		T4		30

[1] Reid et al. (2008b); [2] Burgasser et al. (2007); [3] Dahn et al. (2002b); [4] Schneider et al. (2014); [5] Marocco et al. (2013b); [6] Martín et al. (2010); [7] Artigau et al. (2006); [8] Radigan et al. (2013); [9] Burgasser et al. (2011); [10] Liebert et al. (2003); [11] Liebert et al. (2003); [12] Cruz et al. (2003); [13] Castro et al. (2013); [14] Kirkpatrick et al. (2008); [15] Burgasser et al. (2003); [16] Parker & Tinney (2013); [17] Cruz et al. (2009b); [18] Allers & Liu (2013); [19] Faherty et al. (2013); [20] Gagné et al. (2013); [21] Antonova et al. (2013); [22] Antonova et al. (2013); [23] Faherty et al. (2012c); [24] Leggett et al. (2000); [25] Andrei et al. (2011); [26] Gizis (2002); [27] Folkes et al. (2007); [28] Faherty et al. (2009b); [29] Burgasser et al. (2008); [30] Ellis et al. (2005); [31] Burgasser et al. (2004); [32] Vrba et al. (2004b); [33] Nakajima et al. (1995); [34] Oppenheimer et al. (2001); [35] Costa et al. (2006); [36] Gelino et al. (2002); [37] Zapatero Osorio et al. (2014); [a] NR: Not resolved binary; [b] V: variability found; [c] MP: Metal poor; [d] Y: young.

Flux detected in the UVB arm was extremely low, therefore we chose do not use spectra taken in this range. Telluric standards were observed before or after every target at a close airmass (± 0.1 with respect to the targets). Telluric standard stars are provided in Table 5.11. Bias, darks and flats were taken every night. Arc frames were taken on alternate days. The observing log is reported in Table 5.11.

The spectra were reduced using the ESO X-Shooter pipeline version 1.3.7 (Vernet et al. 2011). In the reduction cascade, the pipeline deletes the non-linear pixels and subtracts bias in the optical or dark frames in the near-infrared. It generates a guess order from a format-check frame, a reference list of arc line and a reference spectral format table. It refines the guess order table into an order table from an order definition frame obtained by illuminating the X-Shooter pinhole with a continuum lamp. The master flat frame and the order tables tracing the flat edges are created. Finally, the pipeline determines the instrumental response and science data are reduced in slit nodding mode.

In the case of the data taken in the near infrared, the pipeline did not produce satisfactory response functions. In this case, we used the spectrum of the telluric star of the corresponding science target observed in the same night to obtain the response function. We removed cosmetics and cosmic rays from the telluric stars, as well as the H and He absorption lines on their spectra, using a Legendre polynomial fit of the pseudo-continuum around the line. We then derived a response function by dividing the non-flux calibrated clean spectrum of the telluric standard by a black body synthetic spectrum with the same temperature as the telluric star (Theodossiou & Danezis 1991b). Finally, to calibrate in response, we used the package *noao.onedspec.telluric* from the software *Image Reduction and Analysis Facility*, (IRAF). More details on data reduction and flux calibration, as well as correction for telluric bands, are described in Alcalá et al. (2014).

To make sure that the flux in the whole near-infrared spectra was correctly scaled, we calibrated the flux of our near-infrared spectra using fluxes given by 2MASS (Two Micron All Sky Survey). We convolved our near-infrared spectra with J, H and K filter transmission curves of 2MASS. The resulting spectra were integrated. We calculated the flux for our targets corresponding to the J, H and K bands using 2MASS magnitudes (Cohen et al. 2003b). Finally, we calculated the scaling factor for J, H and K bands and multiplied our near-infrared spectra in J, H and K filters to have the same flux as given by 2MASS. We scaled flux from the optical spectra to be consistent with the flux in the near-infrared. In the overlapping wavelengths of the optical and near-infrared spectra, we calculated a scaling factor, which is the median of the flux in the overlapping wavelengths of the near-infrared spectra, divided by the median of the flux in the overlapping wavelengths of the optical spectra. The reduced spectra are shown in Fig. 5.1¹. Wavelengths largely affected by telluric absorption are removed from the figure, as well as the

¹These spectra are available in my personal webpage: www.mpia.de/homes/manjavacas/MPIA.html

optical part for object G1229B, because it is contaminated by the flux of its companion and the optical of 2M0144 because it is noisy.

5.3 EMPIRICAL ANALYSIS

5.3.1 FINDING L PLUS T BROWN DWARF BINARIES

Spectra of L plus T brown dwarf binary systems have been widely studied in the past years (Burgasser et al. 2007, 2010; Bardalez Gagliuffi et al. 2014a). The combined spectra of these type of binary systems are expected to show peculiar characteristics, as they are a mix of two quite different spectra, with different atomic and molecular absorptions (Cushing et al. 2005).

Burgasser et al. (2010) described differences of L plus T binary systems in comparison with single template brown dwarf spectra: in general, spectra of L plus T binary systems show bluer spectral energy distribution in the near-infrared, and in particular, some spectral features vary, like the CH₄ and H₂O features at 1.1 μm which are deeper for binaries and the CH₄ feature at 1.6 μm is stronger in comparison to the 2.2 μm CH₄ band. Using such differences, Burgasser et al. (2006, 2010) and Bardalez Gagliuffi et al. (2014a), defined spectral indices which help to detect L plus T brown dwarf binaries. These indices are specified in Table 5.2. In Table 5.3 and Table 5.4 the regions that select potential L plus T brown dwarfs binary systems are defined. Objects found in between four and eight selection regions are considered weak L plus T binary candidates, and objects found in eight or more selection regions are considered strong candidates.

By calculating these indices we select those objects in our sample that are candidates L plus T binary systems. The result is shown in Figures 5.2, 5.3 and 5.4. These indices selected two strong binary candidates: object SDSS J0423485-041403 [hereafter SD0423] was selected by nine indices and object DENIS-P J0255.0-4700 [hereafter DE0255] was selected by eight indices. We also find four weak candidates: object 2MASS J01365662+0933473 [hereafter SIMP0136] is selected by six indices, and object 2MASS J13411160-3052505 [hereafter 2M1341], object 2MASS J00531899-3631102 [hereafter 2M0053] and object 2MASS J02572581-3105523 [hereafter 2M0257] are selected by five indices.

The next step in the empirical analysis consists on comparing our spectra with libraries of well characterized brown dwarf template spectra. First, we degrade the resolution of our X-Shooter spectra to the resolution of each template. Then we re-interpolate the library of brown dwarf template spectra and X-Shooter spectra to the same grid.

As template brown dwarf spectra we use McLean et al. (2003) and Cushing et al. (2011) spectra,

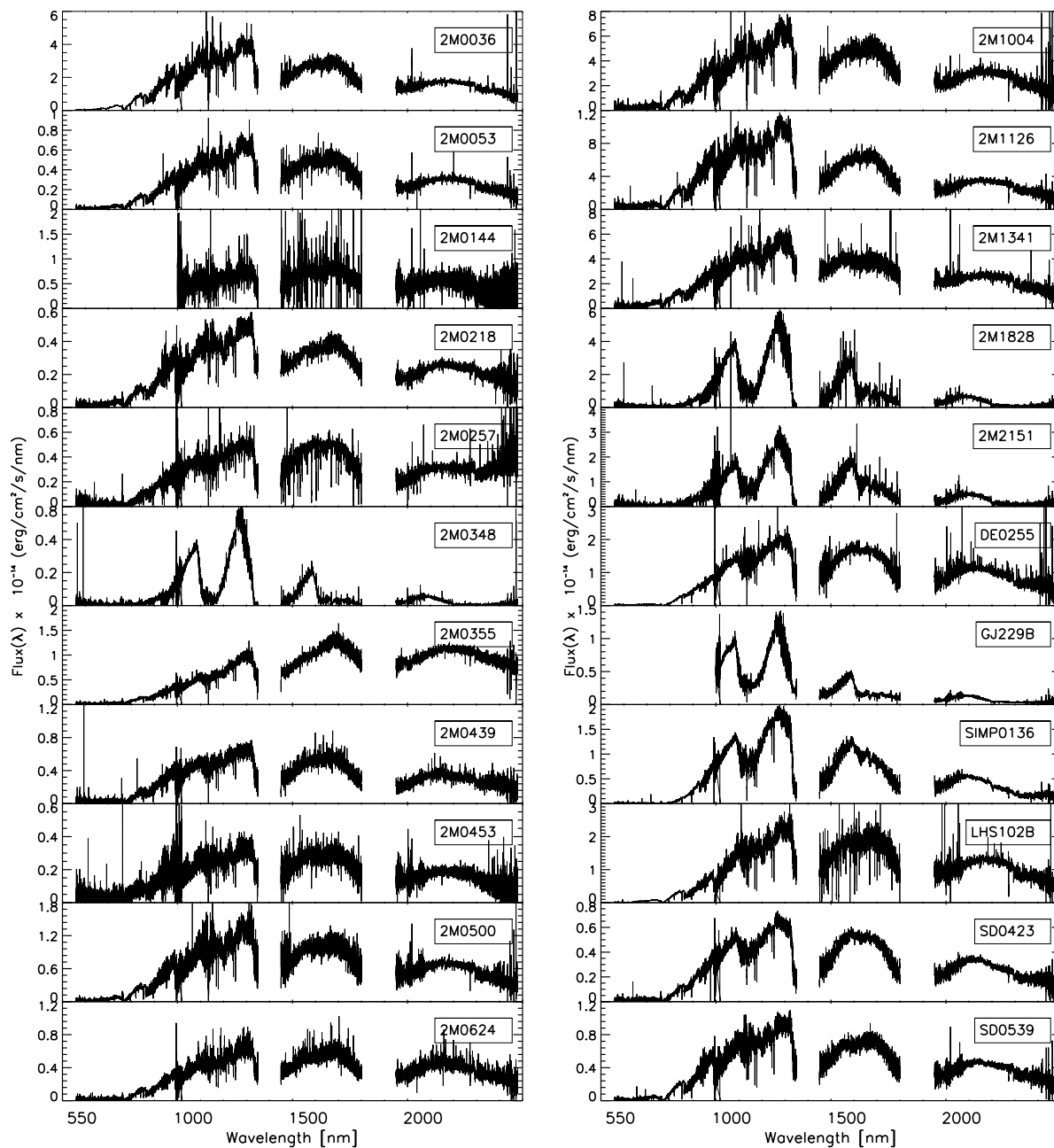


Figure 5.1: Spectra of our 22 targets after reduction. Wavelengths largely affected by telluric absorption are removed from the figure, as well as the optical part for object GJ229B, because it is contaminated by the flux of its companion and the optical part of 2M0144 because it is noisy.

with a resolution of $R \sim 2000$, and SpeX Prism Spectral Library spectra², with a resolution of $R \sim 120$. In total we consider 462 spectra from SpeX Spectral Library, plus 14 from Cushing et al. (2011) library and 47 spectra from McLean et al. (2003) library.

In our analysis we search for the best matches to single template spectra from the SpeX library, Cushing et al. (2011) and McLean et al. (2003) libraries and to combinations of two template spectra from those libraries. Before comparing our X-Shooter spectra to combination of two template spectra coming from the libraries, we calibrate their fluxes to the same distance using the absolute magnitude-color relation published by Dupuy & Liu (2012a). To identify the best matches to our spectra, we use a χ^2 approach as explained in Cushing et al. (2008), as well as visual inspection. We test if the fit to a binary template is significantly better than the fit to a single template using a one-sided F-test statistic. We use as the distribution statistic ratio:

$$\eta_{SB} = \frac{\min(\chi_{single}^2).df_{binary}}{\min(\chi_{binary}^2).df_{single}} \quad (5.1)$$

where $\min(\chi_{single}^2)$ and $\min(\chi_{binary}^2)$ are the minimum χ^2 for the best match to a single or to a composite template, and df_{binary} and df_{single} are the degrees of freedom for the binary template fit and the single template fit. The degrees of freedom are the number of data points used in the fit ($n = 24751$) minus one to account the scaling between our spectra and the template spectra. To rule out the null hypothesis, meaning that the candidate is not a binary with a 99% confidence level, we require $\eta_{SB} > 1.03$. The F-statistic rejected one of our candidates, namely: SIMP0136.

We show the best matches to our X-Shooter spectra in Appendix 5.B. In Table 5.5 we show the best matches of our brown dwarf binary system candidates selected by the indices.

5.3.2 FINDING L PLUS L OR T PLUS T BROWN DWARF BINARIES

Spectroscopic identification of brown dwarf L plus L and T plus T binaries pairs has not been as developed as that for L plus T binaries. Differences within L or T brown dwarfs of different sub-types reside mainly in smooth changes of the spectral energy distribution. Therefore the search for binaries with similar spectral types is challenging.

Before comparing to the set of libraries following the same method as in Section 5.3.1, we first test the efficiency of this method to search for L plus L and T plus T binaries using synthetic binaries. To this aim we have chosen several L and T single and not peculiar brown dwarfs

²<http://pono.ucsd.edu/~adam/browndwarfs/spexprism/>

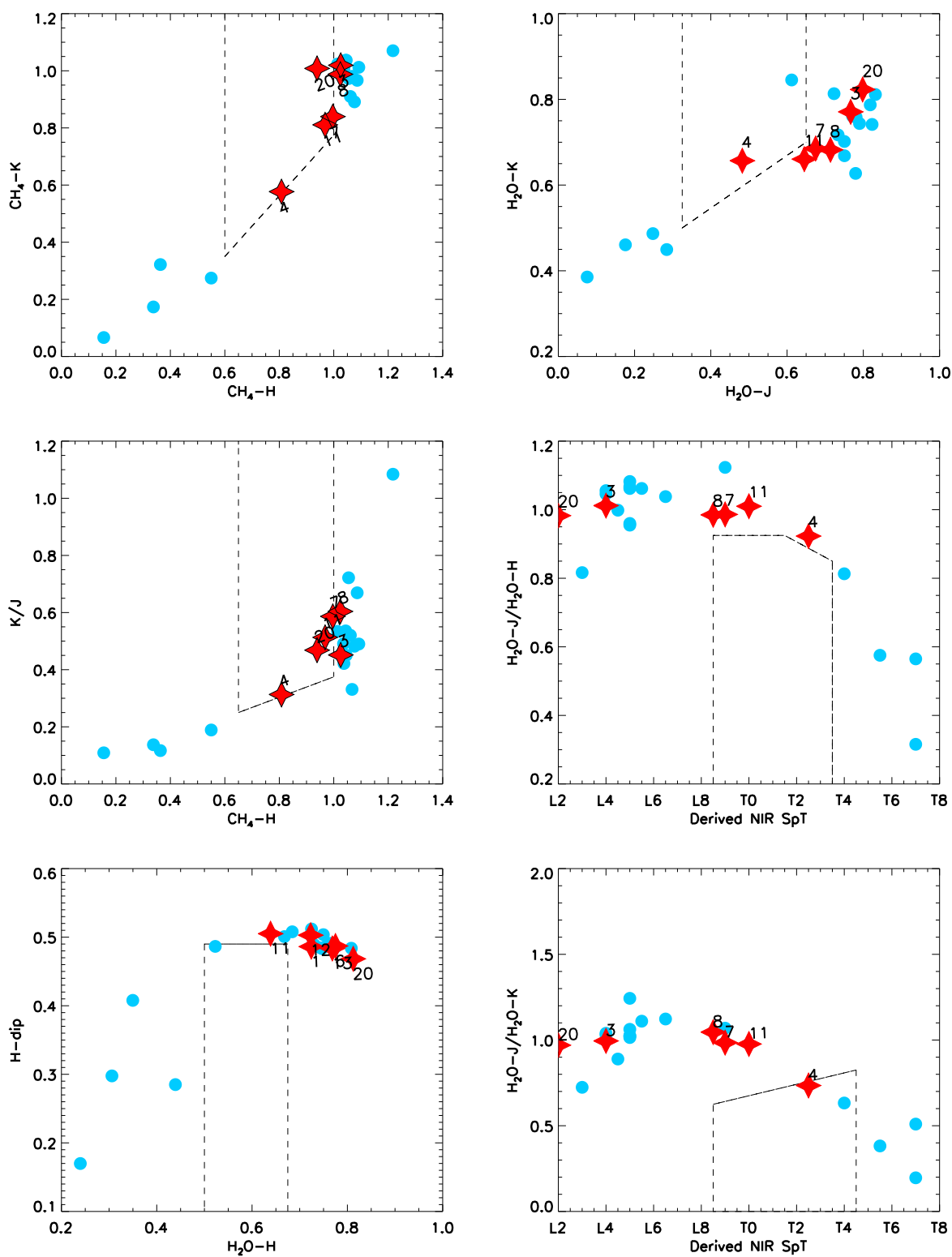


Figure 5.2: Spectral index selection. Numbers 1-22 correspond to our objects. The boxes shown with dashed lines mark the areas where the selection criteria of Table 5.2 are valid. The red stars represent objects satisfying more than four such criteria.

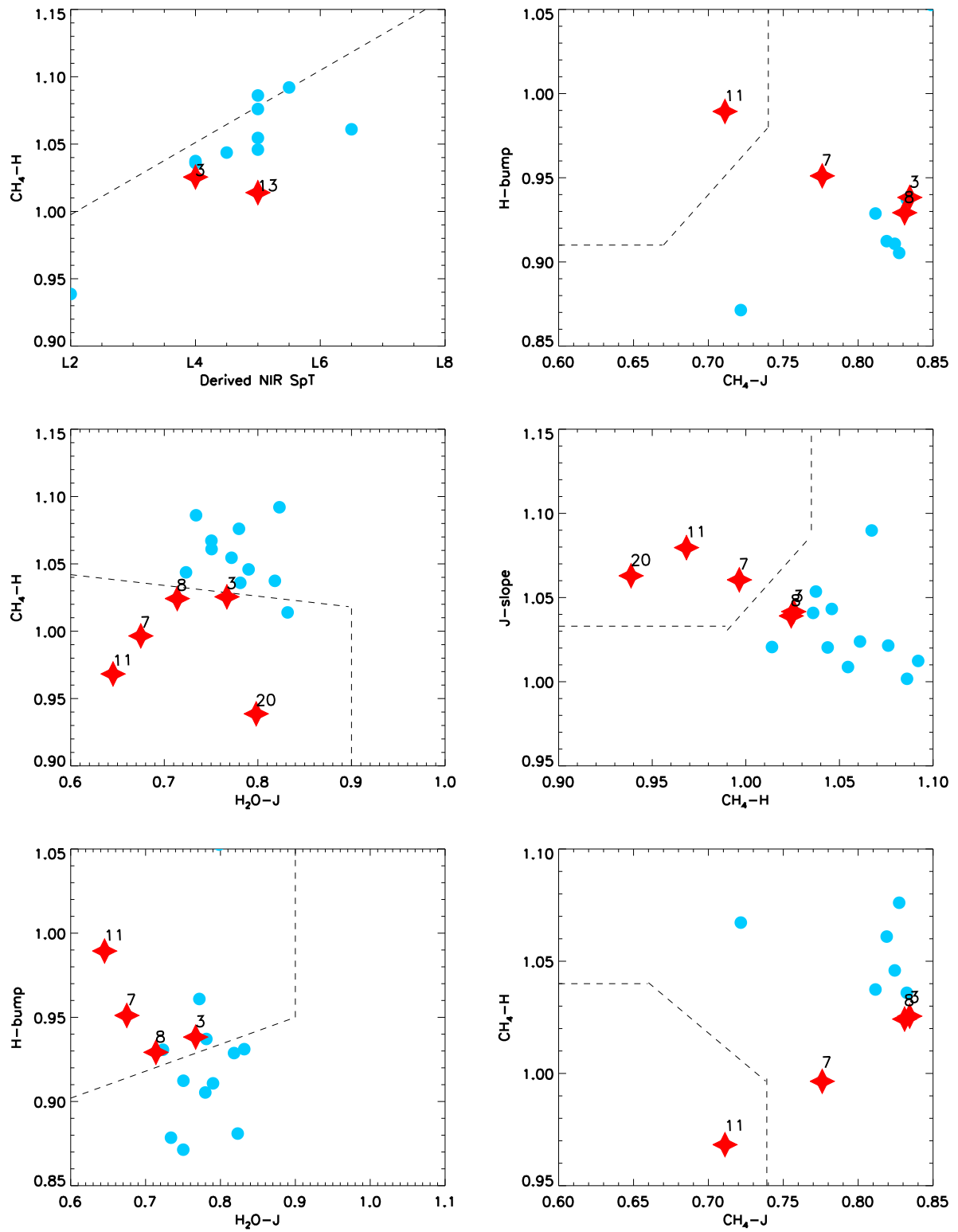


Figure 5.3: Spectral index selection.

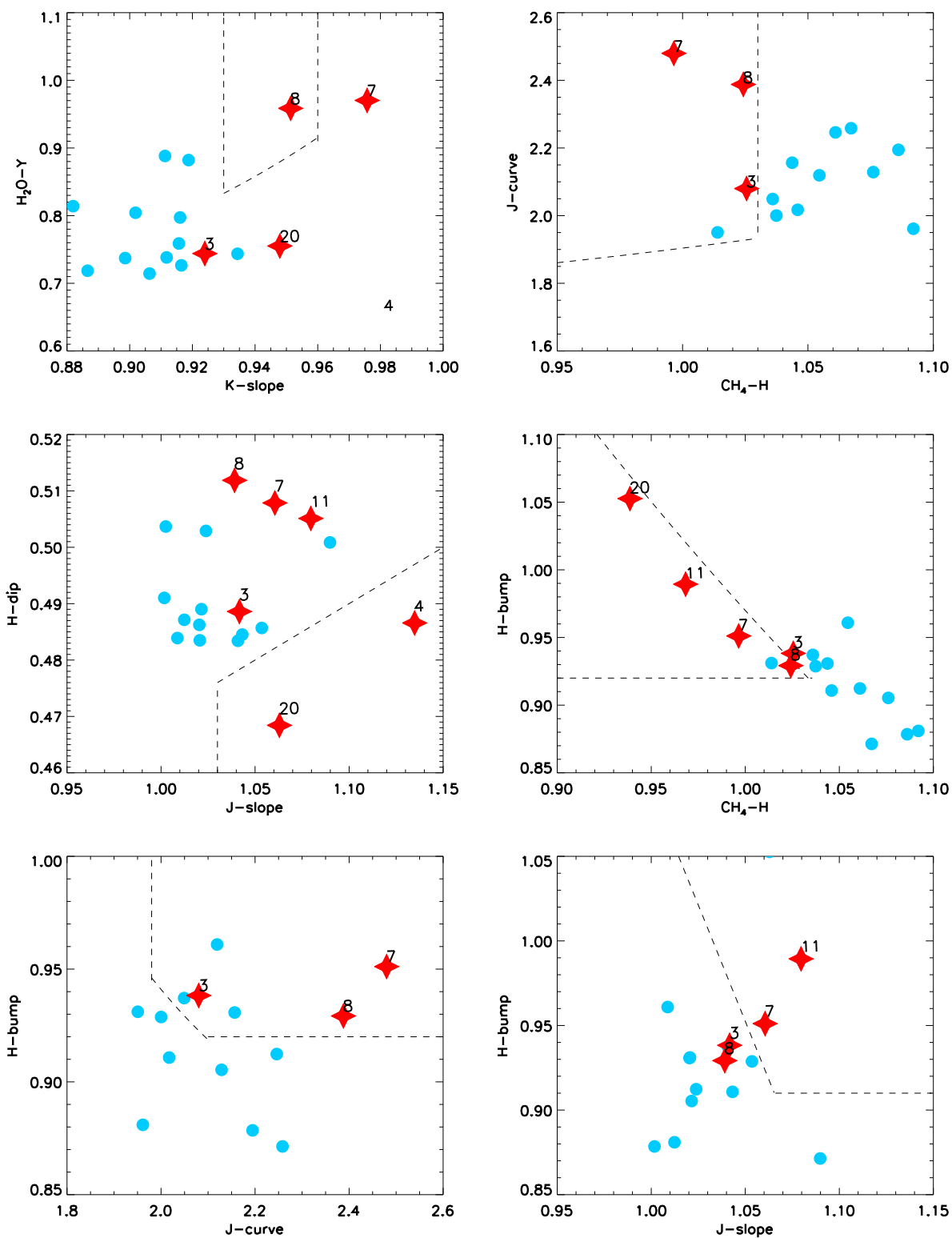


Figure 5.4: Spectral index selection.

Table 5.2: Spectral indices to select L plus T brown dwarf binary candidates.

Index	Numerator Range (a)	Denominator Range (a)	Feature	Reference
H ₂ O-J	1140-1165	1260-1285	1150 nm H ₂ O	1
CH ₄ -J	1315-1340	1260-1285	1320 nm CH ₄	1
H ₂ O-H	1480-1520	1560-1600	1400 nm H ₂ O	1
CH ₄ -H	1635-1675	1560-1600	1650 nm CH ₄	1
H ₂ O-K	1975-1995	2080-2100	1900 nm H ₂ O	1
CH ₄ -K	2215-2255	2080-2120	2200 nm CH ₄	1
K/J	2060-2100	1250-1290	$J - K$ color	1
H-dip	1610-1640	1560-1590 + 1660-1690 (b)	1650 nm CH ₄	2
K-slope	2.06-2.10	2.10-2.14	K-band shape/ CIA H ₂	3
J-slope	1.27-1.30	1.30-1.33	1.28 μ m flux peak shape	4
J-curve	1.04-1.07+1.26-1.29 (c)	1.14-1.17	Curvature across J-band	4
H-bump	1.54-1.57	1.66-1.69	Slope across H-band peak	4
$H_2O - Y$	1.04-1.07	1.14-1.17	1.15 μ mH ₂ O	4
Derived NIR SpT			Near infrared spectral type (d)	1

(a) Wavelength range in nm over which flux density is integrated; (b) Denominator is the sum of the flux in the two wavelength ranges; (c) Numerator is the sum of the two ranges; (d) Near infrared spectral type derived using comparison to SpeX spectra.

References: [1] - Burgasser et al. (2006), [2] - Burgasser et al. (2010), [3] - Burgasser et al. (2002a), [4] - Bardalez Gagliuffi et al. (2014a).

Table 5.3: Index criteria for the selection of potential brown dwarf binary systems

Ordinate	Abscissa	Inflection Points
H ₂ O-J	H ₂ O-K	(0.325,0.5),(0.65,0.7)
CH ₄ -H	CH ₄ -K	(0.6,0.35),(1,0.775)
CH ₄ -H	K/J	(0.65,0.25),(1,0.375)
H ₂ O-H	H-dip	(0.5,0.49),(0.875,0.49)
Spex SpT	H ₂ O-J/H ₂ O-H	(L8.5,0.925),(T1.5,0.925),(T3,0.85)
Spex SpT	H ₂ O-J/CH ₄ -K	(L8.5,0.625),(T4.5,0.825)

Table 5.4: Delimiters for selection regions of potential brown dwarf binary systems

Abscissa	Ordinate	Limits
SpT	CH ₄ -H	Best fit curve: $y = -4.3 \times 10^{-4}x^2 + 0.0253x + 0.7178$
H ₂ O-J	CH ₄ -H	Intersection of: $-0.08x + 1.09$ and $x = 0.90$
H ₂ O-J	H-bump	Intersection of: $y = 0.16x + 0.806$ and $x = 0.90$
CH ₄ -J	CH ₄ -H	Intersection of: $y = -0.56x + 1.41$ and $y = 1.04$
CH ₄ -J	H-bump	Intersection of: $y = 1.00x + 0.24$, $x = 0.74$ and $y = 0.91$
CH ₄ -H	J-slope	Intersection of: $y = 1.250x - 0.207$, $x = 1.03$ and $y = 1.03$
CH ₄ -H	J-curve	Best fit curve: $y = 1.245x^2 - 1.565x + 2.224$
CH ₄ -H	H-bump	Best fit curve: $y = 1.36x^2 - 4.26x + 3.89$
J-slope	H-dip	Intersection of $y = 0.20x + 0.27$ and $x = 1.03$
J-slope	H-bump	Intersection of: $y = -2.75x + 3.84$ and $y = 0.91$
K-slope	H ₂ O-Y	Best fit curve: $y = 12.036x^2 - 20.000x + 8.973$
J-curve	H-bump	Best fit curve: $y = 0.269x^2 - 1.326x + 2.479$

Table 5.5: Best matches to objects selected as binary candidates by spectral indices

Binary candidate	Single best match spectrum	Composite best match spectrum
SD0423	SDSSJ105213.51+442255.7 (T0.5)	2MASS15150083+4847416 (L6) + SDSS125453.90-012247.4 (T2)
DE0255	SDSS085234.90+472035.0 (L9.5)	SDSS103931.35+325625.5 (T1) + SDSS163030.53+434404.0 (L7)
SIMP0136	SDSS152103.24+013142 (T2)	DENIS-PJ225210-173013 (L7.5, bin) + SDSSJ000013+255418 (T4.5)
2M1341	GJ1048B (L1)	SDSS 175805.46+463311.9 (T6.5) + GJ1048B (L1)
2M0257	SDSSJ083806.16+195304.4 (L4.5)	SDSSJ024256.98+212319.6 (L4) + SDSS2044749.61-071818.3 (T0)
2M0053	2MASSJ17461199+5034036 (L5)	SDSSJ120602+281328 (T3) + Kelu-1 (L3p)

Table 5.6: Best matches to the synthetic artificial L plus L and T plus T binary systems

Artificial binary	Single best match spectrum
2M1303-4445 (L6) + DE2200-3038 (L0)	2MASS0345432+254023 (L1) 2MASS2130446-084520 (L1.5)
SD1113+3430 (L3) + DE2200-3038 (L0)	2MASS2130446-084520 (L1.5) HD89744B (L early)
SD1219+3128 (L8) + SD1113+3430 (L3)	DENIS-PJ1228-1547 (L6±2) 2MASSJ14283132+5923354 (L4)
2M1553+1532 (T7) + 2M11220-3512 (T2)	SDSSJ120602+281328 (T3) SDSS175032+175903 (T3.5)
SD0151+1244 (T1) + 2M0407+1514 (T5)	SDSSJ102109-030420 (T3) SDSS143945+304220 (T2.5)

spectra from the SpeX library. Then, we calibrated their fluxes to the same distance, using the absolute magnitude-color relation published by Dupuy & Liu (2012a). We combined different pairs of L brown dwarfs spectra with L brown dwarf and different pairs of T brown dwarfs spectra with T brown dwarfs, creating L plus L and T plus T synthetic spectra of binaries. These L plus L and T plus T brown dwarf binary pairs that can be found in the first column in Table 5.6.

We compared these artificial binary pairs to single SpeX templates and composites of two SpeX template spectra. Our objective is to test whether synthetic L plus L and T plus T binaries can be identified by comparing to spectral library spectra. Figures with the best matches are shown in Appendix 5.C. In the second column of Table 5.6 we summarize best matches to artificial L plus L and T plus T binary systems.

From this analysis, we conclude that L plus L and T plus T brown dwarfs binaries are not straightforward to detect just by comparing with single or composite spectral libraries. Therefore, additional data will be necessary to find these binaries, i.e. parallaxes, high resolution imaging or high resolution spectra. From our 22 object sample, distances for 15 objects are available in the literature, with precision around 10%. Color-magnitude diagrams (CMD) showing $J - K$ in the MKO (Mauna Kea Observatory) photometric system versus absolute magnitude in the J band are presented for these objects (Fig. 5.5). In this Figure, we plot the color-absolute magnitude relationship by Dupuy & Liu (2012a). The two known binaries in our sample stand out over objects with their same spectral types and other one, the young object 2M0355 is much redder as objects of its same spectral type because of its youth. For the rest of the objects we cannot draw clear conclusions as there are no clear outliers.

Table 5.7: Best matches to the rest of our objects that are presumably single brown dwarfs.

Name	Best match	Library
LHS 102B	SDSS 083506.16+195304.4 (L4.5)	SpeX
2MASS J00361617+1821104	2MASS 02081833+2542533 (L1)	Cushing et al. (2011)
2MASS J01443536-0716142	2MASS 22244381-0158521 (L4.5)	Cushing et al. (2011)
2MASS J02182913-3133230	Kelu-1 (L2)	Cushing et al. (2011)
2MASS J04390101-2353083	2MASS 15150083+4847416 (L6)	Cushing et al. (2011)
2MASS J04532647-1751543	2MASS 15150083+4847416 (L6)	Cushing et al. (2011)
2MASS J05002100+0330501	2MASS 15065441+1321060 (L3)	Cushing et al. (2011)
2MASS J05395200-0059019	2MASS 18131803+5101246 (L5)	SpeX
2MASS J10043929-3335189	2MASS 11463449+2230527AB (L3)	Cushing et al. (2011)

In Table 5.7 we report the best matches of the spectra of our objects to those of spectral libraries McLean et al. (2003), Cushing et al. (2011) and SpeX libraries. We show best matches in Appendix 5.C. In Table 5.7 we do not include those objects for which we did not find a match to spectra from spectral libraries. For objects 2M0348 (T7), Gl229B (T7), 2M1828 (T5.5) and 2M2151 (T4) the lack of acceptable matches is probably due to the lack of late T template spectra in these libraries. Objects 2M0624 (L5:) and 2M1126 (L6.5:) have peculiar spectra, so we do not expect to find an acceptable match. Object 2M0355 (object 10) is a young brown dwarf (Faherty et al. 2012c; Allers & Liu 2013; Gagné et al. 2013; Zapatero Osorio et al. 2014) with a likely age of ~ 100 Myr, therefore we do not expect to find a spectrum in these spectral libraries that reproduce this object’s observations.

5.4 EQUIVALENT WIDTHS

We measured the equivalent width of a variety of alkali lines with sufficient signal-to-noise in our spectra. The measured lines are: RbI (794.8 nm), NaI (818.3 nm), NaI (819.5 nm) and CsI (852.0 nm) in the optical, and KI (1253 nm) in the near infrared. In Figure 5.6 we plot, in the optical, the equivalent widths for RbI (794.8 nm) and CsI (852.0 nm) objects from Chiu et al. (2006); Golimowski et al. (2004b); Knapp et al. (2004) and Lodieu et al. (2014, submitted) versus their spectral types. In the near infrared, we plot equivalent widths of the KI line at 1253 nm for our objects. We overplot also field objects (Cushing et al. 2005; McLean et al. 2003), that belong to TW Hydrae Association (TWA), young companions (Allers & Liu 2007; Bonnefoy et al. 2014), young β -dwarfs and γ -dwarfs as a comparison (Allers & Liu 2007). We

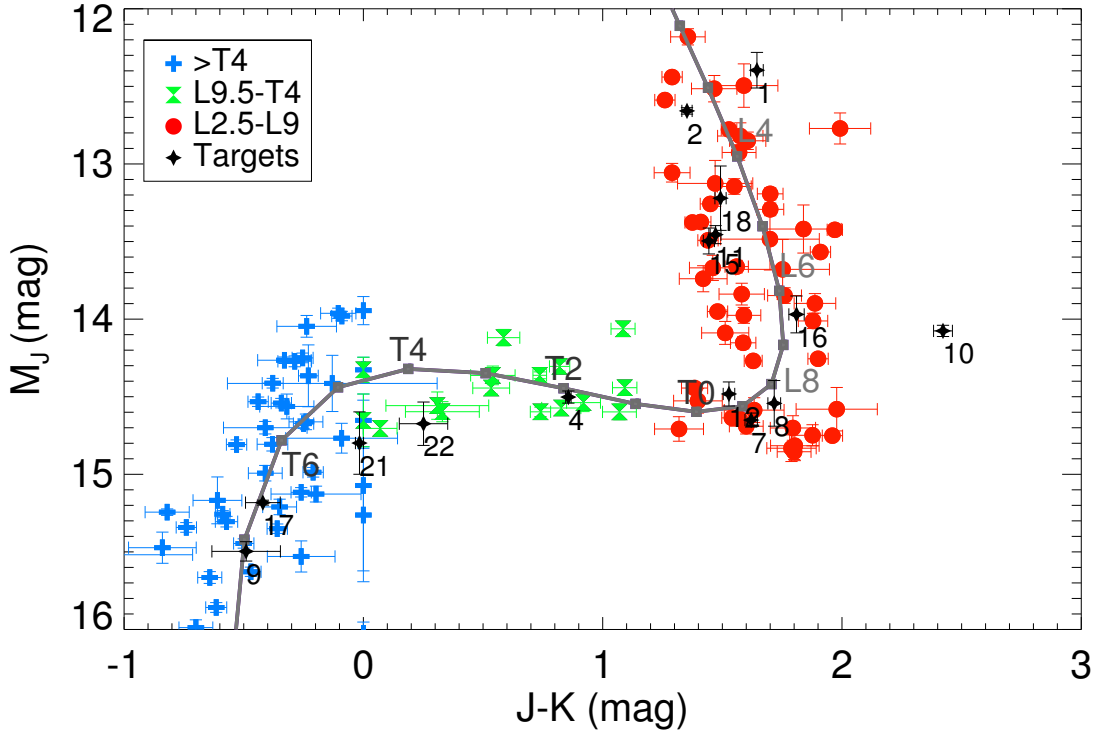


Figure 5.5: Color-magnitude diagram showing brown dwarfs with measured parallaxes from Dupuy & Liu (2012a) together with our targets (black). Objects have the same numbers as in Table 5.1. We overplot the color-absolute magnitude relationship from Dupuy & Liu (2012a).

degraded all spectra in the near infrared to a resolution $R \sim 700$, which is the lowest resolution of all the spectra for which we calculate KI (1253 nm) equivalent width. The binary candidates are represented with black symbols.

In the optical, we observe the disappearance of the alkali elements, because of the depletion of alkali atoms into dust condensates. The apparent strength of the Na I subordinate lines decreases with spectra types from the early Ls through the T dwarfs. The equivalent width of CsI (852.0 nm) increases from L0 to L9 and it is maximum for the early T brown dwarfs, and it weakens progressively from the early to the late T brown dwarfs. In the near infrared (see Figure 5.7), the equivalent width of the KI (1253 nm) has two peaks at around L4 and T4, with a minimum at about L8. This might reflect that as for the potassium, we see different atmospheric layers for the various subtypes (Faherty et al. 2014). Object 2M0355 (object 10), has weaker alkali lines in the optical and in the near infrared, as it is a young object (Faherty et al. 2012c; Allers & Liu 2007; Zapatero Osorio et al. 2014). We report the equivalent widths of the alkali lines for every target in Table 5.8. We do not report the equivalent widths for those alkali lines that were

not detected in some of the targets.

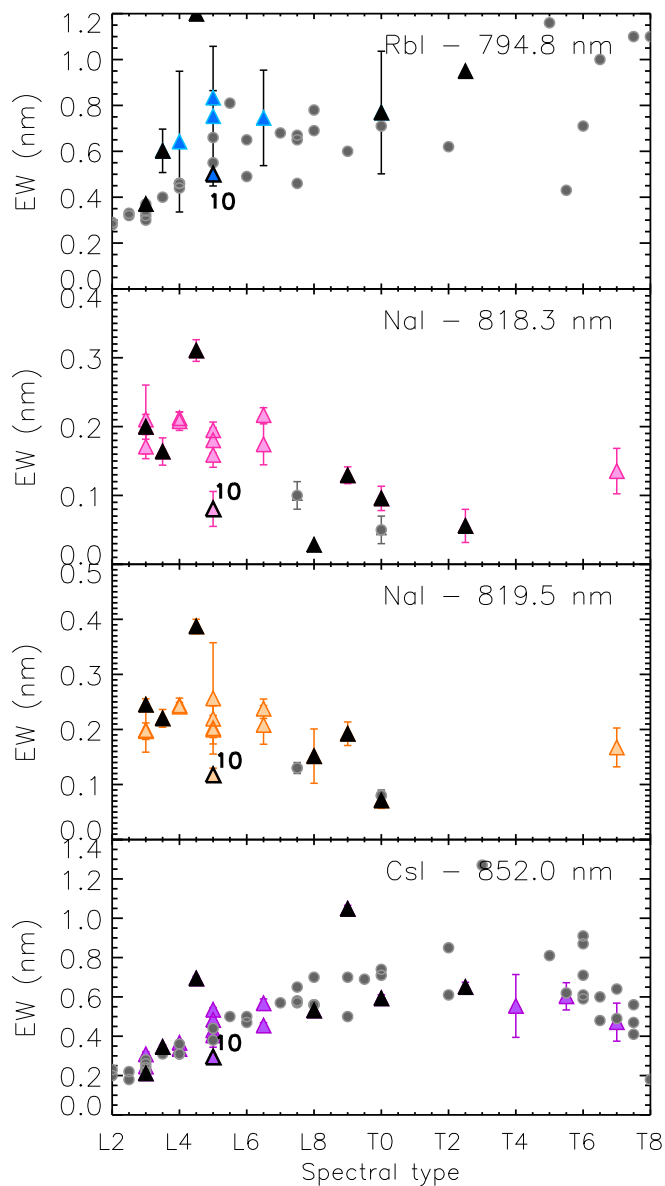


Figure 5.6: Equivalent widths of the detected alkali lines in the optical for our targets (color triangles), binary candidates or known binaries from our sample (black triangles) and for objects with equivalent width available in the literature (grey circles). The young object 2M0355 (number 8) is marked as well. These equivalent widths come from Chiu et al. (2006); Golimowski et al. (2004b); Knapp et al. (2004) and Lodieu et al. (2014, submitted to A&A).

Table 5.8: Equivalent widths in nm for alkali lines measured in the optical and in the near infrared.

Name	Rb I (794.8 nm)	Na I (818.3 nm)	Na I (819.5 nm)	Cs I (852.0 nm)	K I (1253 nm)
LHS 102B	1.19±0.01	0.31±0.01	0.38±0.01	0.69±0.01	0.79±0.01
2MASS J00361617+1821104	0.53±0.01	0.21±0.01	0.24±0.01	0.34±0.01	0.93±0.01
2MASS J00531899-3631102	0.60±0.09	0.16±0.02	0.22±0.02	0.35±0.01	0.85±0.01
SIMP 01365662+0933473	≤0.3	0.06±0.02	≤0.06	0.65±0.02	0.83±0.01
2MASS J01443536-0716142				0.43±0.09	0.82±0.02
2MASS J02182913-3133230	≤0.09	0.17±0.02	0.19±0.02	0.31±0.01	0.79±0.01
DENIS-P J0255.0-4700	≤0.18	0.13±0.01	0.19±0.02	1.04±0.02	0.45±0.01
2MASS J02572581-3105523	≤0.54		0.15±0.05	0.53±0.03	0.54±0.01
2MASS J03480772-6022270	≤0.46	≤0.28	≤0.013	0.47±0.09	0.42±0.01
2MASS J03552337+1133437	≤0.03	0.08±0.03	0.12±0.01	0.29±0.01	0.28±0.01
SDSS J0423485-041403	0.77±0.27	0.09±0.02	0.07±0.01	0.59±0.02	0.67±0.01
2MASS J04390101-2353083	≤0.28	0.17±0.03	0.21±0.04	0.57±0.02	0.72±0.01
2MASS J04532647-1751543	≤0.15	0.21±0.05	0.19±0.04	0.25±0.03	0.70±0.01
2MASS J05002100+0330501	0.64±0.31	0.21±0.01	0.24±0.01	0.37±0.01	0.81±0.01
2MASS J05395200-0059019	0.83±0.03	0.19±0.01	0.20±0.02	0.54±0.01	0.89±0.01
2MASS J06244595-4521548	≤0.61	0.16±0.02	0.19±0.03	0.48±0.02	0.70±0.01
Gl 229B					0.24±0.01
2MASS J10043929-3335189	0.75±0.30	0.18±0.02	0.22±0.02	0.40±0.02	0.85±0.01
2MASS J11263991-5003550	0.75±0.21	0.22±0.01	0.24±0.02	0.45±0.02	1.05±0.01
2MASS J13411160-3052505	0.37±0.28	0.19±0.02	0.25±0.01	0.21±0.01	0.64±0.01
2MASS J18283572-4849046				0.60±0.07	0.71±0.01
2MASS J21513839-4853542				0.55±0.16	0.98±0.01

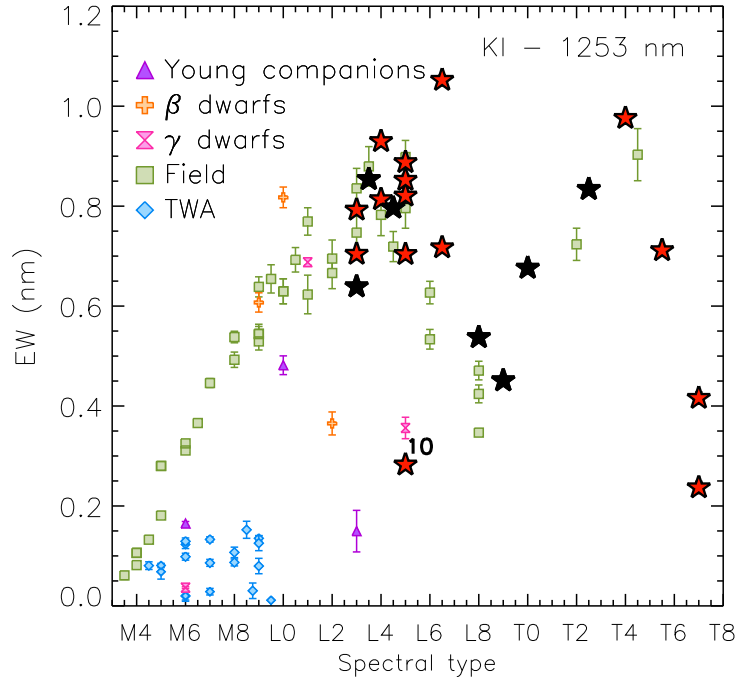


Figure 5.7: Equivalent widths of the KI alkali line at 1253 nm of our objects (red stars), and binary candidates or known binaries of our sample (black stars), compared to the equivalent widths of field brown dwarf, young companions, young brown dwarfs (β and γ dwarfs) and members of the TW Hydrae Association (TWA). The young object 2M0355 (number 8) is also marked.

5.5 COMPARISON TO SYNTHETIC SPECTRA

In this section, we compare the optical and near-infrared spectra of our objects, to predictions from BT-Settl atmospheric models (Allard et al. 2007, 2011), excepting brown dwarf binary candidates and objects with low signal to noise. We derive atmospheric parameters of the objects and to reveal non-reproducibilities of the models. The models are described in Allard et al. (2011, 2012a,c).

We selected subgrids of synthetic spectra with $400 \text{ K} \leq T_{eff} \leq 3000 \text{ K}$, $3.5 \leq \log g \leq 5.5$ and metallicities of +0.0 and +0.3, which are the metallicities for which the latest version of the BT-Settl models are available. The solar metallicity is based on metallicities calculated by Caffau et al. (2011). The spacing of the model grid is 50 K and 0.5 dex in $\log g$. Effective temperature, gravity, metallicity and alpha element enhancement are described in the model name strings as `lte-LOGG+[M/H]a+[ALPHA/H]`.

The BT-Settl 2014 synthetic spectra were smoothed to the resolution of X-Shooter. The models were then reinterpolated on the X-Shooter wavelength grid. The spectra were normalized using

the same method than in Section 5.3 and explained in Cushing et al. (2008). The results from the fit were always double checked visually. The atmospheric parameters corresponding to the best fit models are reported in Table 5.9. The parameters T_{eff} , $\log g$, and $[M/H]$ have minimum uncertainties of 50 K, and 0.5 dex respectively. These errors correspond to the sampling of the atmospheric parameters of the model grids. In Figures 5.8, 5.9 and 5.10 we show the best fit of the synthetic spectra to our targets. We avoid the following objects to test models: binary candidates (2M1341, DE0255, SIMP0136, 2M0053, 2M0257), known binaries (LHS102B, SD0423), noisy spectra (2M0144) or targets with known nearby objects that may contaminate the spectra, like in the case of Gl229B.

The CH_4 and the FeH molecules opacities are still incomplete in the new BT-Settl 2014 models. Methane line opacities are based on the semi-empirical list of Homeier et al. (2003), which is highly incomplete in the H band and only supplemented with a small set of room-temperature transitions for the Y and J bands. Iron hydride causes absorption features through the $F^4\Delta - X^4\Delta$ system between 650 and 1600 nm, but in addition to this Hargreaves et al. (2010) identified significant opacity contributions from the $A^4\Pi - A^4\Pi$ system, which is not yet included in the list of FeH lines available to PHOENIX. This explains that the H-band is not well reproduced for any of the L or T brown dwarf spectra, and also the J band in the case of T brown dwarfs. For three of the L brown dwarfs, the best match is found for $\log g = 5.5$, with solar metallicity, four of the L brown dwarfs have best matches with $\log g = 5.0$, but $[M/H] = +0.3$.

Best matches to the BT-Settl models are shown in Fig. 5.8, 5.9 and 5.10. There are two of the L brown dwarfs that have best matches with low gravity models, 2M0355 and 2M0624. Object 2M0355 is known previously to be young (Cruz et al. 2009b; Allers & Liu 2007; Zapatero Osorio et al. 2014), so we expect gravity to be lower, therefore, the result given by the models is consistent. There are no references of youth for object 2M0624. Best matches to T brown dwarfs are always to solar metallicity models. The best match to object 2M1828 is to a model with high gravity.

5.6 REVISED PROPERTIES

In this section we aim at revisiting the properties of some of our targets taking into account the results of Section 5.3 and Section 5.5.

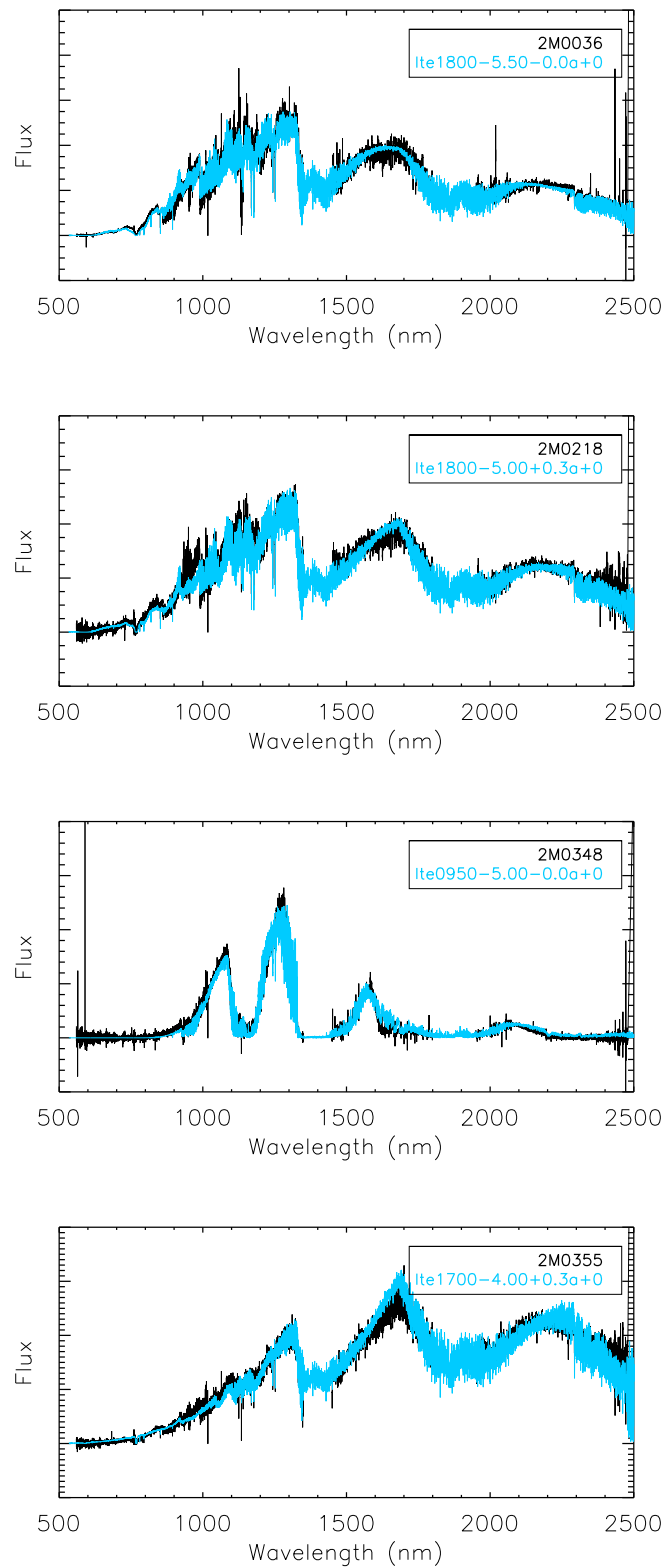


Figure 5.8: Best matches to BT-Settl models 2014. Effective temperature, gravity, metallicity and alpha element enhancement are described in the model name strings as $1te-LOGG+[M/H]a+[ALPHA/H]$. The flux is $F(\lambda)$.

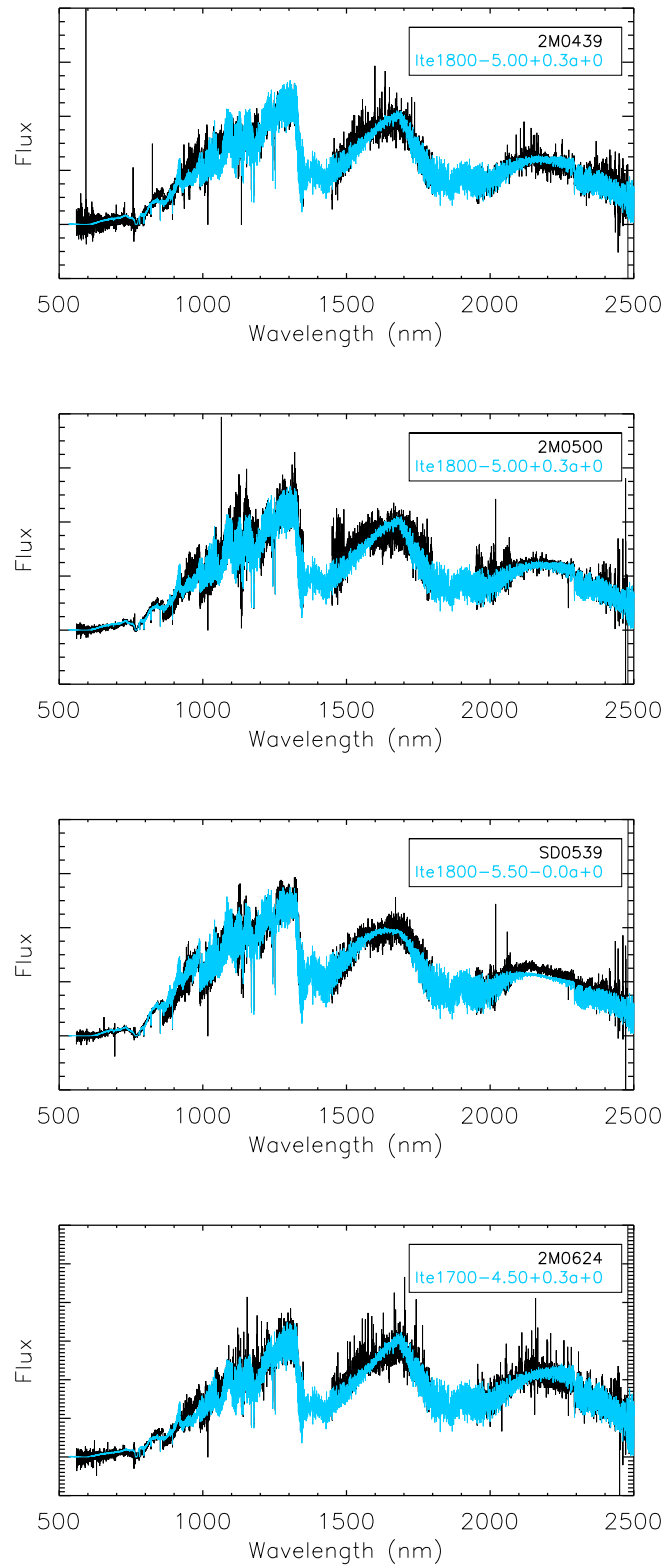


Figure 5.9: Best matches to BT-Settl models 2014. Effective temperature, gravity, metallicity and alpha element enhancement are described in the model name strings as $1te-LOGG+[M/H]a+[ALPHA/H]$. The flux is $F(\lambda)$.

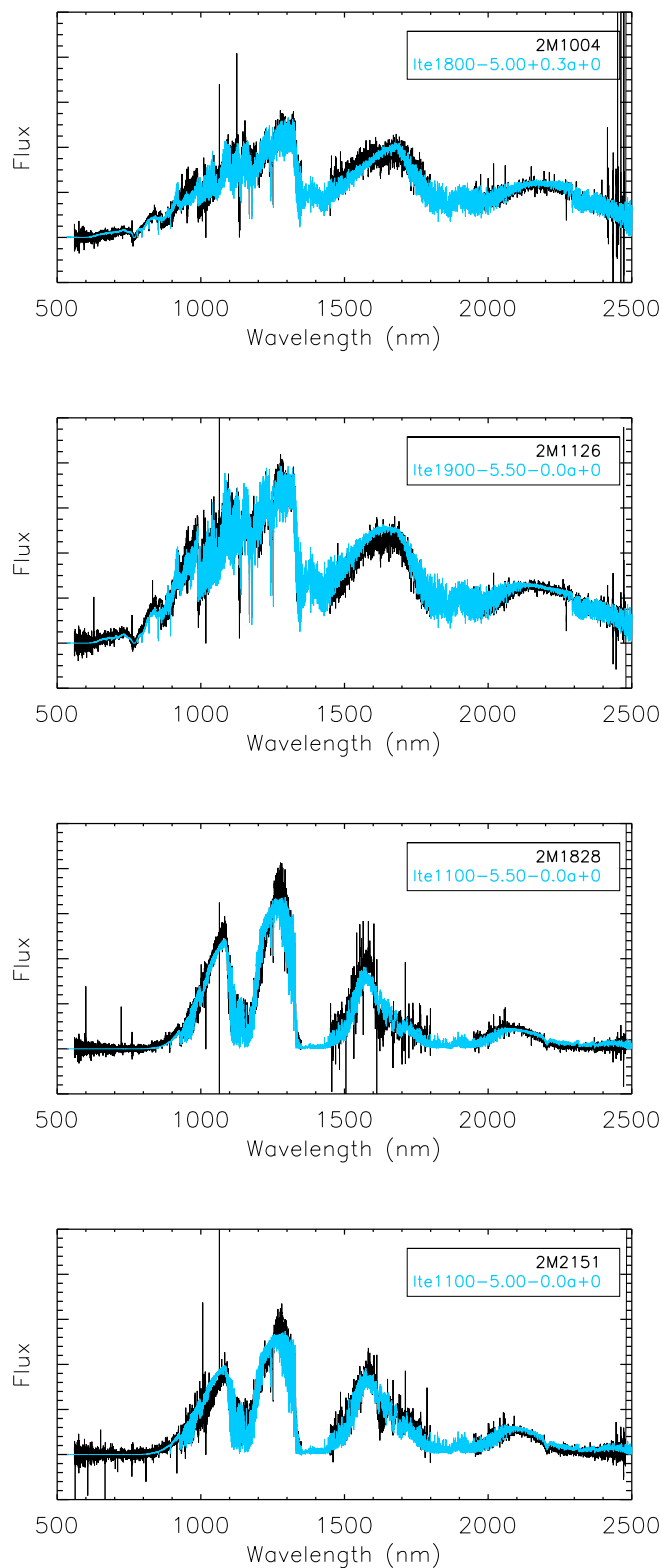


Figure 5.10: Best matches to BT-Settl models 2014. Effective temperature, gravity, metallicity and alpha element enhancement are described in the model name strings as $1te-LOGG+[M/H]a+[ALPHA/H]$. The flux is $F(\lambda)$.

Table 5.9: Atmospheric parameters corresponding to the best fit spectra or synthetic fluxes for our targets. We give $T_{\text{eff}}/\log g/[M/H]$.

Name	T_{eff}	$\log g$	[M/H]
2MASS J00361617+1821104	1800±100	5.5±0.5	+0.0
2MASS J02182913-3133230	1800±100	5.0±0.5	+0.3
2MASS J03480772-6022270	950±100	5.0±0.5	+0.0
2MASS J03552337+1133437	1700±100	4.0±0.5	+0.3
2MASS J04390101-2353083	1800±100	5.0±0.5	+0.3
2MASS J05002100+0330501	1800±100	5.0±0.5	+0.3
2MASS J05395200-0059019	1800±100	5.5±0.5	+0.0
2MASS J06244595-4521548	1700±100	4.5±0.5	+0.3
2MASS J10043929-3335189	1800±100	5.0±0.5	+0.3
2MASS J11263991-5003550	1900±100	5.5±0.5	+0.0
2MASS J18283572-4849046	1100±100	5.5±0.5	+0.0
2MASS J21513839-4853542	1100±100	5.0±0.5	+0.0

Grid sample in T_{eff} is 50 K and in $\log g$ is 0.5 dex.

5.6.1 SIMP 01365662+0933473

SIMP 0136 was discovered by [Artigau et al. \(2006\)](#) in the SIMP (Sondage Infrarouge de Mouvement Propre) near infrared proper motion survey, and it was classified as a T2.5. [Goldman et al. \(2008\)](#) searched for companions using high resolution imaging with NACO at VLT with sensitivity of 0.2" (1-40 au), but no companions were found. [Artigau et al. \(2009\)](#) detected photometric variability in the J and K bands with a modulation of ~ 2.4 h and an amplitude of 50 mmag. [Radigan et al. \(2012\)](#) calculated the amplitude of the variability for a object similar to SIMP 0136 (2MASS J21392676+0220226, T1.5) if it were produced by a companion. The variability in that case would be much smaller than the variability found. [Apai et al. \(2013\)](#) explained this variability as a mixture of thick and thin patchy iron and silicate clouds covering the surface of the object.

In Section 5.3.1 we used the indices by [Burgasser et al. \(2006, 2010\)](#) and [Bardalez Gagliuffi et al. \(2014b\)](#) to select potential L plus T brown dwarf binary candidates. Object SIMP 0136 was selected as a brown dwarf binary candidate, but it was rejected by a F-statistic analysis. These indices are suitable to select peculiar spectral characteristics that appear usually in binary L plus T brown dwarf spectra. However, if variability is produced by a mixture of thick and thin clouds in the brown dwarf atmosphere, similar peculiar spectral characteristics would appear in brown

dwarf spectra. We also compared our X-Shooter spectra with several single and composite of brown dwarf spectra of several spectral libraries (McLean et al. (2003), Cushing et al. (2011) and Spex) and we found a best match with SDSS152103.24+013142.7 (T2) (see Fig. 5.13), which is compatible with the rejected binary hypothesis by the F-test.

A preliminary parallax of 166.2 ± 2.92 mas for SIMP 0136 was obtained from the NPARSEC program (ESO program 186.C-0756, Smart et al. 2013). Using this parallax, we placed the object in a CMD diagram together with objects published in Dupuy & Liu (2012a) (see Fig. 5.5) and we compared to objects of similar spectral type. We do not find significant overluminosity for this object, i. e. overluminosity of more than ~ 0.8 mag within the error bars. This contradicts the hypothesis of similar spectral type binaries (see Fig. 5.5).

5.6.2 DENIS-P J0255.0-4700

Object DE0255 was discovered by Martín et al. (1999) and it was classified as a peculiar L6. Koen et al. (2005a) reported evidence of variability in different timescales (1.7 and 5 h). Morales-Calderón et al. (2006) concluded that DE0255 may vary with a 7.4 h period at $4.5 \mu\text{m}$, but it does not at $8 \mu\text{m}$. Other groups did not see variability (Koen et al. 2005b). Costa et al. (2006) reported absolute parallax for this object: $\pi = 201.37 \pm 3.89$ mas. Burgasser et al. (2008) classified this object in the optical as a L8 and in the near infrared as a L9. Finally, Reid et al. (2008a) searched for multiplicity for this object using high-resolution NICMOS NIC1 camera imaging on the Hubble Space Telescope but found no evidence of multiplicity.

In Section 5.3.1, DE0255 was selected as a weak candidate L plus T binary using Burgasser et al. (2006, 2010) and Bardalez Gagliuffi et al. (2014b) indices. We compared DE0255 near infrared X-Shooter spectra to single and composite spectra from McLean et al. (2003), Cushing et al. (2011) and Spex libraries and found reliable matches to single late L spectra and to composite spectra of late L plus early T spectra (see Fig. 5.12).

Using the Costa et al. (2006) published parallax for this object, we plot this object in a CMD diagram together with objects published in Dupuy & Liu (2012a) (see Fig. 5.5), as done for SIMP0136 previously, and no overluminosity is found.

5.6.3 2MASS J13411160-3052505

Object 2M1341 was discovered by Reid et al. (2008a) using 2MASS data. Faherty et al. (2009b) published its distance: 24 ± 2 pc. Kirkpatrick et al. (2011) classified it as a L2 with a peculiar spectrum. Bardalez Gagliuffi et al. (2014b) compared to several SpeX templates and concluded

that this objects could be a $L1.2\pm0.3$ plus a $T6.3\pm1.0$.

In Section 5.3.1, object 2M1341 was selected as a weak candidate L plus T binary using Burgasser et al. (2006, 2010); Bardalez Gagliuffi et al. (2014a) indices. We compared the 2M1341 X-Shooter near infrared spectrum to McLean et al. (2003), Cushing et al. (2011) and Spex libraries and the best matches to this object were composite spectra of L plus T brown dwarf spectra: SDSS 175805.46+463311.9 (T6.5) + GJ1048B (L1) or 2MASS 1217110-031113 (T7) + GJ1048B (L1). However, none of the matches are able to fully reproduce features in the H and K bands. No overluminosity is found for this object when we plot it in the CMD.

5.6.4 2MASS J00531899-3631102

The object 2M0053 was discovered by Reid et al. (2008c) in a 2MASS survey. Kirkpatrick et al. (2008) obtained its optical spectra and classified as a L3.5.

This object was selected by Burgasser et al. (2006, 2010) and Bardalez Gagliuffi et al. (2014a) indices as a weak brown dwarf binary candidate. After comparing to all library spectra from Spex, Cushing et al. (2005) and McLean et al. (2003), we found a best match to single and composite templates. The best match to a single spectra is 2MASS J17461199+5034036 (L5). The best match to a composite spectra is a combination of SDSS120602.51 (T3) and Kelu-1 (L3). Best matches can be found in Fig. 5.16. There is not parallax for this object, so we cannot confirm or refute if this object is a binary.

5.6.5 2MASS J02572581-3105523

The object 2M0257 was discovered by Reid et al. (2008c) in a 2MASS survey. Kirkpatrick et al. (2008) obtained its optical spectra and classified as a L8. Marocco et al. (2013b) provided its trigonometric parallax: $\pi = 99.7\pm6.7$ mas.

This object was selected by spectral indices as a weak brown dwarf binary candidate. The comparison with single and composite template spectra from SpeX, Cushing et al. (2005) and McLean et al. (2003) libraries give as best match a combination of two spectra: 2MASS0028208+224905 (L7) and SDSS1044749.61-071818.3 (T0). The best match for this object is available in Fig. 5.15. Nevertheless, when we compare with objects of similar spectral type in a color-magnitude diagram (see Fig. 5.5), no overluminosity is found.

5.7 VERY LOW MASS BINARY FRACTION

The last update in the very low mass spectral binary fraction was published by Bardalez Gagliuffi et al. (2014a). They reported a summary of all confirmed and candidate spectral binaries discovered to date, with spectral types from M7 to T3. There are 34 very low mass spectral binaries and candidates, and ten of them have been confirmed by various methods: direct imaging, radial velocity or astrometric variability. We provide five brown dwarf binary candidates, two of them confirmed using imaging method. This increases the number of very low mass binary candidates by 15%.

In our sample of 22 objects, we find 5 very low mass binary candidates, from which 2 of them are confirmed and one more, LHS 102B is a L4.5 known brown dwarf binary. We find that $27 \pm 11\%$ of the L and T objects in our sample may be unresolved binary candidates with one L and one T possible members, which corresponds to a mass ratio of $q \geq 0.2$ for an age of a few Gyr (expected for most investigated objects). This percentage agrees with previous results (Burgasser 2007; Goldman et al. 2008; Bardalez Gagliuffi et al. 2014a). Our work does not explore smaller mass ratios. It is necessary to consider that employing Burgasser et al. (2006, 2010) and Bardalez Gagliuffi et al. (2014a) method, we are not detecting similar spectral type low mass binaries, i.e. L plus L and T plus T binaries. In this case, we miss systems that are closer than 3-4 au, as high imaging resolution does not have enough resolution. Therefore, the only method left to detect similar spectral type binaries would be astrometric variability or radial velocity monitoring.

5.8 CONCLUSIONS

We observed and analyzed 22 optical and near infrared medium resolution VLT/X-Shooter spectra of brown dwarfs with spectral types between L3 and T7. Our sample has peculiar spectral characteristics or different classifications in the optical and in the near infrared. Two objects from our sample are known binaries, that allow us to test our analysis.

Using Burgasser et al. (2006, 2010) and Bardalez Gagliuffi et al. (2014a) method, we selected six objects as potential L plus T binary candidates: SIMP0136 (T2.5), SD0423 (T0, known binary), DE0255 (L9) and 2M1341 (L3, peculiar spectra), 2M0053 (L4) and 2M0257 (L8.5). We compared these six objects with spectral libraries of field brown dwarfs (McLean et al. (2003); Cushing et al. (2011) and Spex) and composite spectra of these libraries. Object SIMP0136 was discarded as a brown dwarf binary candidate using a one-sided F-test.

We also examined the possibility to find L plus L or T plus T brown dwarfs binaries using a com-

parison to spectral libraries. As they are not remarkable differences in the spectral characteristics within subtypes of the same spectral type, apart from the SED, we are not able to find L plus L or T plus T brown dwarfs binary systems using this method. Additional data, such as parallax measurements, high-resolution imaging or high resolution spectra are necessary in order to find these systems.

We measured the equivalent width of alkali lines with good signal to noise in the optical and in the near infrared spectra. We conclude that in the transition from L to T spectral types, the Na I doublet in the optical is the first to disappear, while the other alkalines are present in the optical and near infrared in the whole L to T spectral types.

We re-calculated the very low mass binary fraction. Including the results from this work, we increase the fraction of candidates to spectral binaries in approximately 15%. We find that $27 \pm 11\%$ of the L and T objects in our sample may be unresolved binary candidates with one L and one T possible members, which corresponds to a mass ratio of $q \geq 0.2$ for an age of a few Gyr (expected for most investigated objects). This percentage agrees with previous results. Our work does not explore smaller mass ratios.

BT-Settl models 2014 are able to reproduce the majority of the SEDs of our objects in the optical and in the near infrared. Nonetheless, these models usually fail to reproduce the shape of the H-band, due to incomplete opacities for the FeH molecule in BT-Settl 2014 models. Best matches to models give a range of effective temperatures between 950 K and 1900 K, a range of gravities between 4.0 and 5.5. Some best matches correspond to supersolar metallicity.

The optical and near infrared spectra reported in this paper will serve as templates for future studies in any of these wavelengths. In the near future, the Gaia satellite will release high precision parallaxes of more than one billion of objects in the Milky Way, including hundreds of brown dwarfs. These parallaxes will allow us to detect the overluminosity of brown dwarf binaries.

5.A OBSERVING LOG

Table 5.10: Observing log: DIT is the integration time in each position of the slit, and NDIT is the number of exposures.

Name	Date	Arm	DIT (s)	NINT	Seeing (")	Airmass	Notes
LHS102B	October 16, 2009	NIR	300	4	1.0	1.05	
LHS102B	October 16, 2009	VIS	290	4	1.0	1.05	
Hip000349	October 16, 2009	NIR	5	1	1.16	1.06	B9V Telluric Standard
Hip000349	October 16, 2009	VIS	6	1	1.16	1.06	B9V Telluric Standard
2M J0036+1821	November 7, 2009	NIR	300	4	1.1	1.4	
2M J0036+1821	November 7, 2009	VIS	290	4	1.1	1.4	
Hip112022	November 7, 2009	NIR	5	1	1.4	1.5	B2IV Telluric Standard
Hip112022	November 7, 2009	VIS	6	1	1.4	1.5	B2IV Telluric Standard
2M J0053-3631	October 16, 2009	NIR	300	4	1.4	1.05	
2M J0053-3631	October 16, 2009	VIS	290	4	1.4	1.05	
Hip000349	October 16, 2009	NIR	5	1	1.15	1.01	B9V Telluric Standard
Hip000349	October 16, 2009	VIS	6	1	1.15	1.01	B9V Telluric Standard
SIMP J0136+0933	December 14, 2009	NIR	300	4	0.9	1.2	
SIMP J0136+0933	December 14, 2009	VIS	290	4	0.9	1.2	
Hip021576	December 14, 2009	NIR	5	1	1.1	1.05	B3V Telluric Standard
Hip021576	December 14, 2009	VIS	6	1	1.1	1.05	B3V Telluric Standard
2M J0144-0716	December 14, 2009	NIR	300	4	1.05	1.15	
2M J0144-0716	December 14, 2009	VIS	290	4	1.05	1.15	
Hip021576	December 14, 2009	NIR	5	1	1.05	1.15	B6V Telluric Standard
Hip021576	December 14, 2009	VIS	6	1	1.05	1.15	B6V Telluric Standard
2M J0218-3133	January 4, 2010	NIR	300	4	1.05	1.15	
2M J0218-3133	January 4, 2010	VIS	290	4	1.05	1.15	
Hip009534	January 4, 2010	NIR	5	1	0.68	1.1	B6V Telluric Standard
Hip009534	January 4, 2010	VIS	6	1	0.68	1.1	B6V Telluric Standard
DE J0255-4700	October 17, 2009	NIR	300	4	2.2	1.14	
DE J0255-4700	October 17, 2009	VIS	290	4	2.2	1.14	
Hip009549	October 17, 2009	NIR	5	1	2.2	1.2	B6V Telluric Standard
Hip009549	October 17, 2009	VIS	6	1	2.2	1.2	B6V Telluric Standard
2M J0348-6022	October 16, 2009	NIR	300	12	1.7	1.3	
2M J0348-6022	October 16, 2009	VIS	290	12	1.7	1.3	
Hip012389	October 16, 2009	NIR	5	1	1.7	1.3	B8V Telluric Standard
Hip012389	October 16, 2009	VIS	6	1	1.7	1.3	B8V Telluric Standard
2M J0355+1133	December 21, 2009	NIR	300	4	0.92	1.2	
2M J0355+1133	December 21, 2009	VIS	290	4	0.92	1.2	
Hip023060	December 21, 2009	NIR	5	1	0.92	1.2	B2V Telluric Standard
Hip023060	December 21, 2009	VIS	6	1	0.92	1.2	B2V Telluric Standard
SD J0423-0414	December 26, 2009	NIR	300	4	0.8	1.4	
SD J0423-0414	December 26, 2009	VIS	290	4	0.8	1.4	
Hip020424	December 26, 2009	NIR	5	1	0.7	1.4	B9V Telluric Standard
Hip030175	December 26, 2009	VIS	6	1	0.9	1.4	B6.5 Telluric Standard
2M J0439-2353	December 21, 2009	NIR	300	5	1.4	1.0	
2M J0439-2353	December 21, 2009	VIS	290	5	1.4	1.0	
Hip018926	December 21, 2009	NIR	5	1	1.4	1.0	B3V Telluric Standard
Hip018926	December 21, 2009	VIS	6	1	1.4	1.0	B3V Telluric Standard

Table 5.11: Observing log: DIT is the integration time in each position of the slit, and NDIR is the number of exposures.

Name	Date	Arm	DIT (s)	NINT	Seeing (")	Airmass	Notes
2M J0453-1751	December 21, 2009	NIR	300	8	1.1	1.1	
2M J0453-1751	December 21, 2009	VIS	290	8	1.1	1.1	
Hip023060	December 21, 2009	NIR	5	1	1.1	1.1	B2V Telluric Standard
Hip023060	December 21, 2009	VIS	6	1	1.1	1.1	B2V Telluric Standard
2M J0500+0330	February 05, 2010	NIR	300	4	0.7	1.1	
2M J0500+0330	February 05, 2010	VIS	290	4	0.7	1.1	
Hip037623	February 05, 2010	NIR	5	1	0.7	1.1	B5V Telluric Standard
Hip037623	February 05, 2010	VIS	6	1	0.7	1.1	B5V Telluric Standard
SD J0539-0059	January 17, 2010	NIR	300	4	0.7	1.1	
SD J0539-0059	January 17, 2010	VIS	290	4	0.7	1.1	
Hip033007	January 17, 2010	NIR	5	1	0.7	1.1	B4V Telluric Standard
Hip033007	January 17, 2010	VIS	6	1	0.7	1.1	B4V Telluric Standard
GI229B	December 14, 2009	NIR	300	4	1.2	1.4	
GI229B	December 14, 2009	VIS	290	4	1.2	1.4	
Hip044786	December 14, 2009	NIR	5	1	1.2	1.4	B6V Telluric Standard
Hip044786	December 14, 2009	VIS	6	1	1.2	1.4	B6V Telluric Standard
2M J0624-4521	December 16, 2009	NIR	300	5	0.8	1.4	
2M J0624-4521	December 16, 2009	VIS	290	5	0.8	1.4	
Hip030175	December 16, 2009	NIR	5	5	0.8	1.4	B9.5V Telluric Standard
Hip030175	December 16, 2009	VIS	6	5	0.8	1.4	B9.5V Telluric Standard
2M J1004-3335	February 5, 2010	NIR	300	4	0.9	1.0	
2M J1004-3335	February 5, 2010	VIS	290	4	0.9	1.0	
Hip057861	February 5, 2010	NIR	5	1	0.9	1.0	B5V Telluric Standard
Hip057861	February 5, 2010	VIS	6	1	0.9	1.0	B5V Telluric Standard
2M J1126-5003	February 4, 2010	NIR	300	4	1.6	1.1	
2M J1126-5003	February 4, 2010	VIS	290	4	1.6	1.1	
Hip073345	February 4, 2010	NIR	5	4	1.6	1.1	B5V Telluric Standard
Hip073345	February 4, 2010	VIS	6	4	1.6	1.1	B5V Telluric Standard
2M J2151-4853	May 08, 2010	NIR	300	10	1.4	1.2	
2M J2151-4853	May 08, 2010	VIS	290	10	1.4	1.2	
Hip111085	May 08, 2010	NIR	5	10	1.4	1.2	B9V Telluric Standard
Hip111085	May 08, 2010	VIS	6	10	1.4	1.2	B9V Telluric Standard
2M J1341-3052	June 02, 2010	NIR	300	10	0.7	1.0	
2M J1341-3052	June 02, 2010	VIS	290	10	0.7	1.0	
Hip068124	June 02, 2010	NIR	5	10	0.7	1.0	B9V Telluric Standard
Hip068124	June 02, 2010	VIS	6	10	0.7	1.0	B9V Telluric Standard
2M J1828-4849	June 06, 2010	NIR	300	10	1.5	1.4	
2M J1828-4849	June 06, 2010	VIS	290	10	1.5	1.4	
Hip092687	June 06, 2010	NIR	5	1	1.5	1.4	B4III Telluric Standard
Hip092687	June 06, 2010	VIS	6	1	1.5	1.4	B4III Telluric Standard

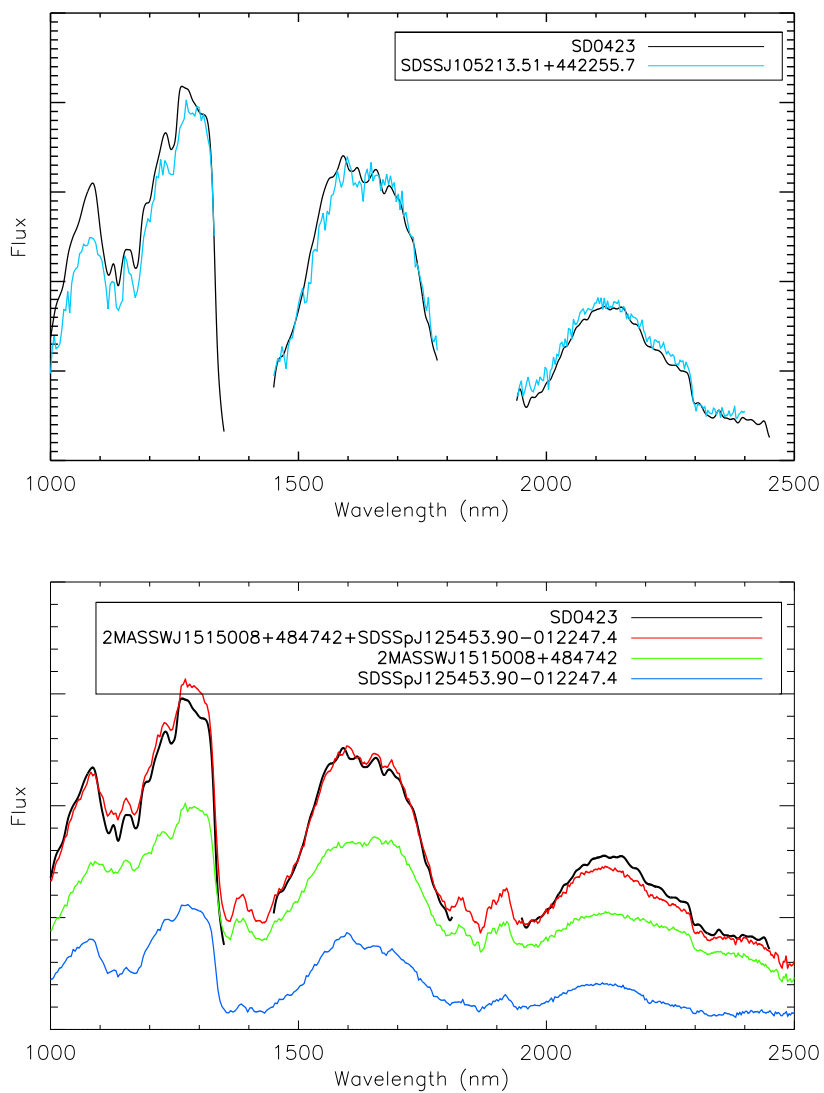


Figure 5.11: Best match for object SD0423 (T0) using single (upper plot) and composite spectra (lower plot) from SpeX library. We show in black our X-Shooter spectra. In the upper plot, the blue spectrum belongs to the best single match. In the lower plot, we show in red the composite spectrum, in green the spectrum of the primary and in blue the spectra of the secondary. The flux is $F(\lambda)$.

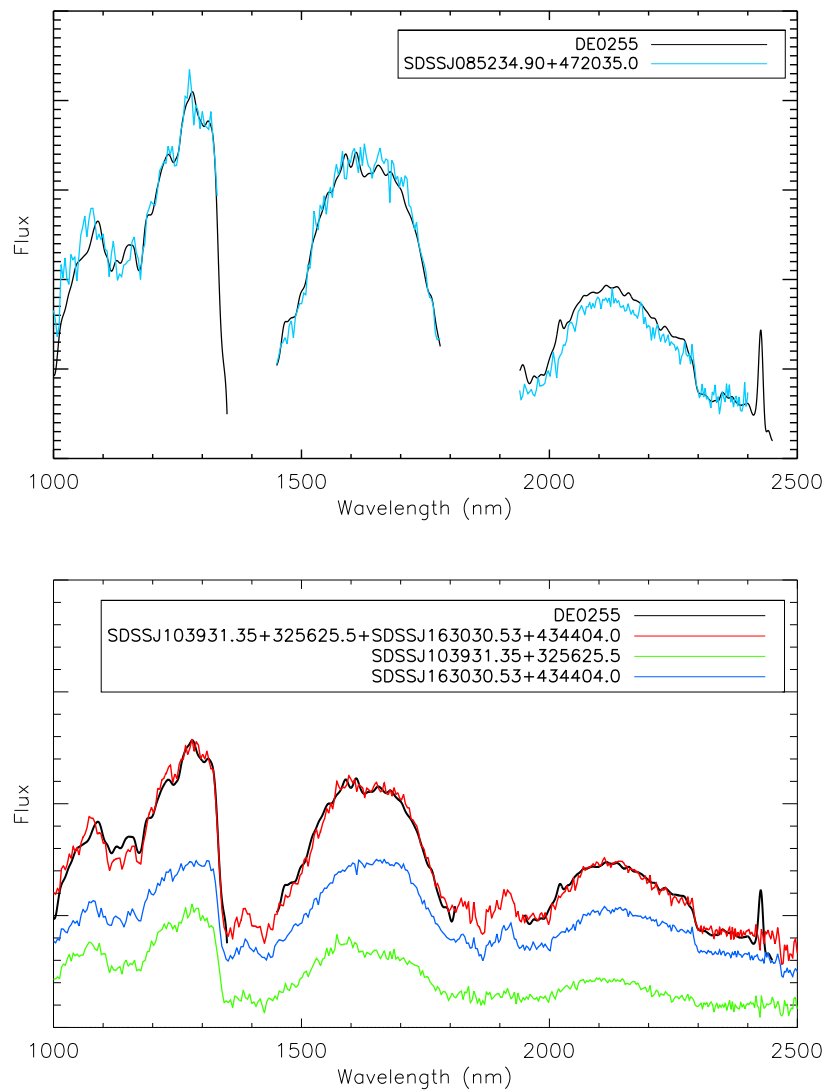


Figure 5.12: Best matches for object DE0255 (L9) using single and composite spectra from SpeX library. We show in black our X-Shooter spectra in both plots. In the upper plot, we show the best match to single spectrum in blue. In the lower plot, we show the red best match composite SpeX spectra, in green SpeX primary and in blue the SpeX secondary. The flux is $F(\lambda)$.

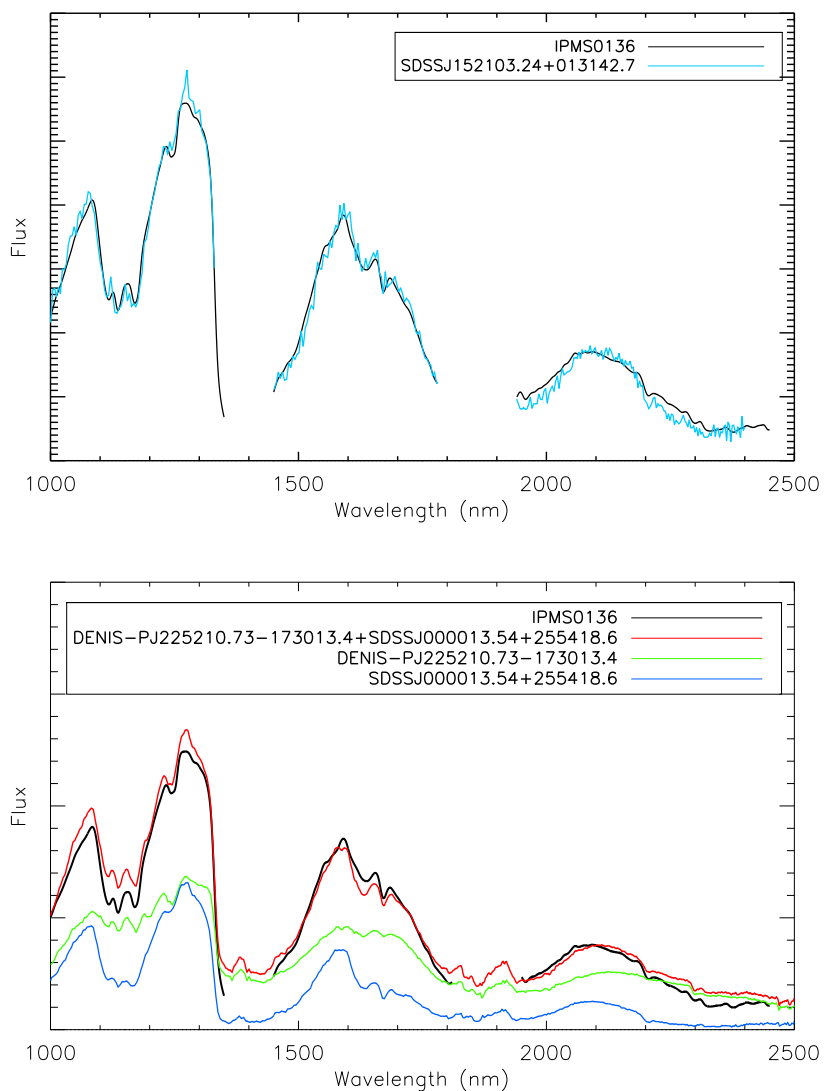


Figure 5.13: Best matches for object SIMP0136 (T2.5) to single and composite spectra. In black our smooth X-Shooter spectrum. In the upper plot, we show the best match to a single spectra in blue. In the lower plot, we show in red the best match to a composite spectra. in green SpeX primary and in blue the SpeX secondary. The flux is $F(\lambda)$.

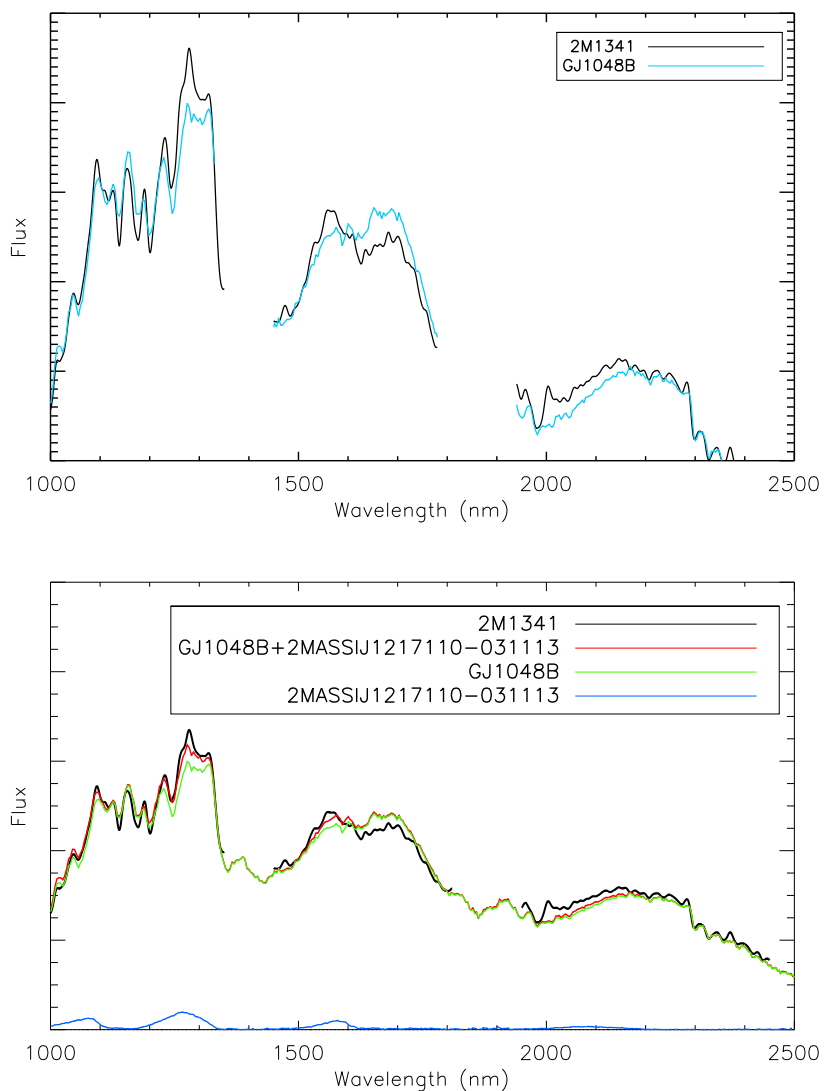


Figure 5.14: Best matches for object 2M1341 (L2, peculiar) to single and composite spectra from SpeX. Our spectra is shown in black. In the upper plot, we show the best match to a single spectra in blue. In the lower plot, we show in red the best match to a composite spectra. in green SpeX primary and in blue the SpeX secondary. The flux is $F(\lambda)$.

5.B BEST MATCHES TO POTENTIAL L PLUS T BINARIES

5.C SYNTHETIC L PLUS L OR T PLUS T BEST MATCHES TO TEMPLATE SPECTRA

5.D BEST MATCHES REST OF OBJECTS

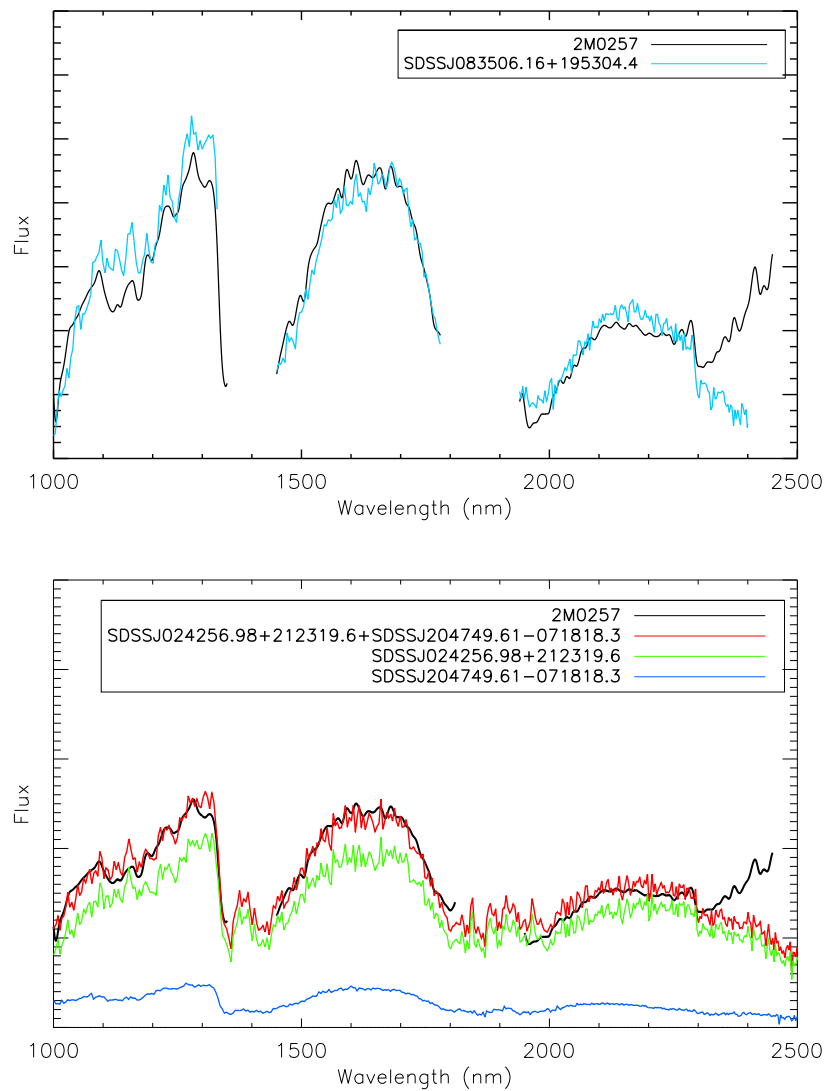


Figure 5.15: Best matches for object 2M0257 to single and composite spectra from SpeX. Our spectra is shown in black. In the upper plot, we show the best match to a single spectra in blue. In the lower plot, we show in red the best match to a composite spectra. in green SpeX primary and in blue the SpeX secondary. The flux is $F(\lambda)$.

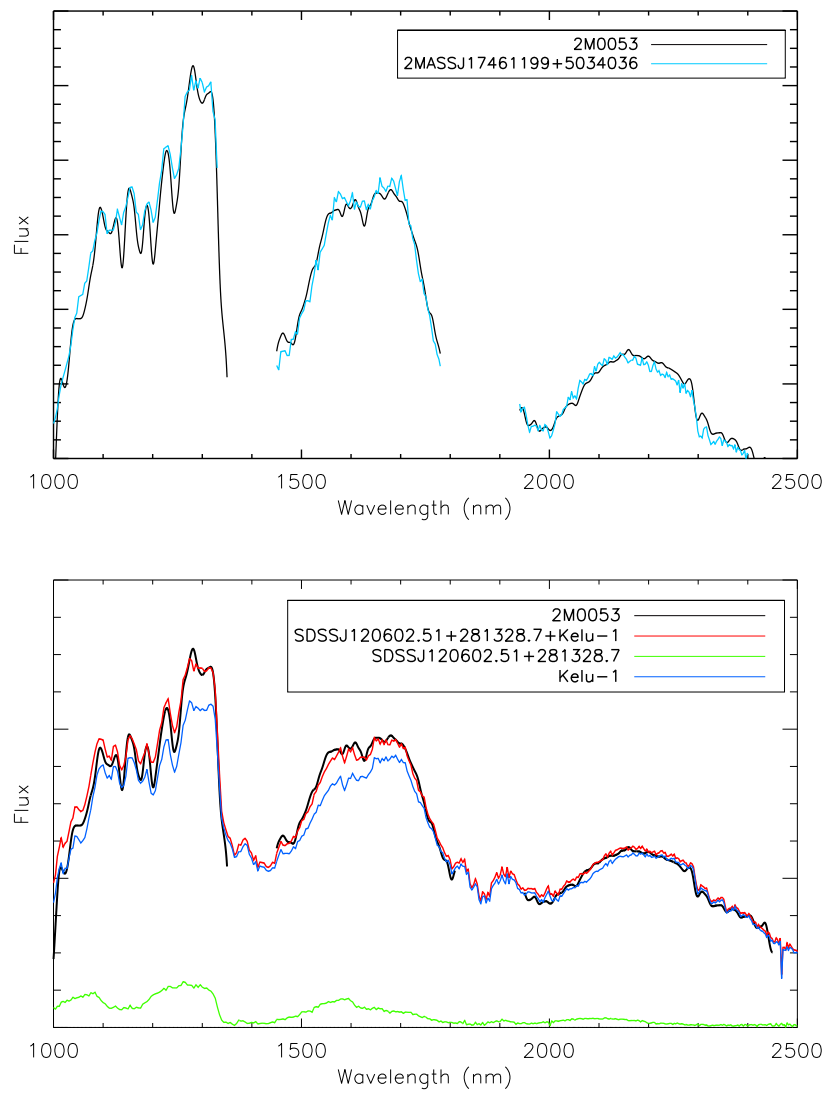


Figure 5.16: Best matches for object 2M0053 to single and composite spectra from SpeX. Our spectra is shown in black. In the upper plot, we show the best match to a single spectra in blue. In the lower plot, we show in red the best match to a composite spectra. in green SpeX primary and in blue the SpeX secondary. The flux is $F(\lambda)$.

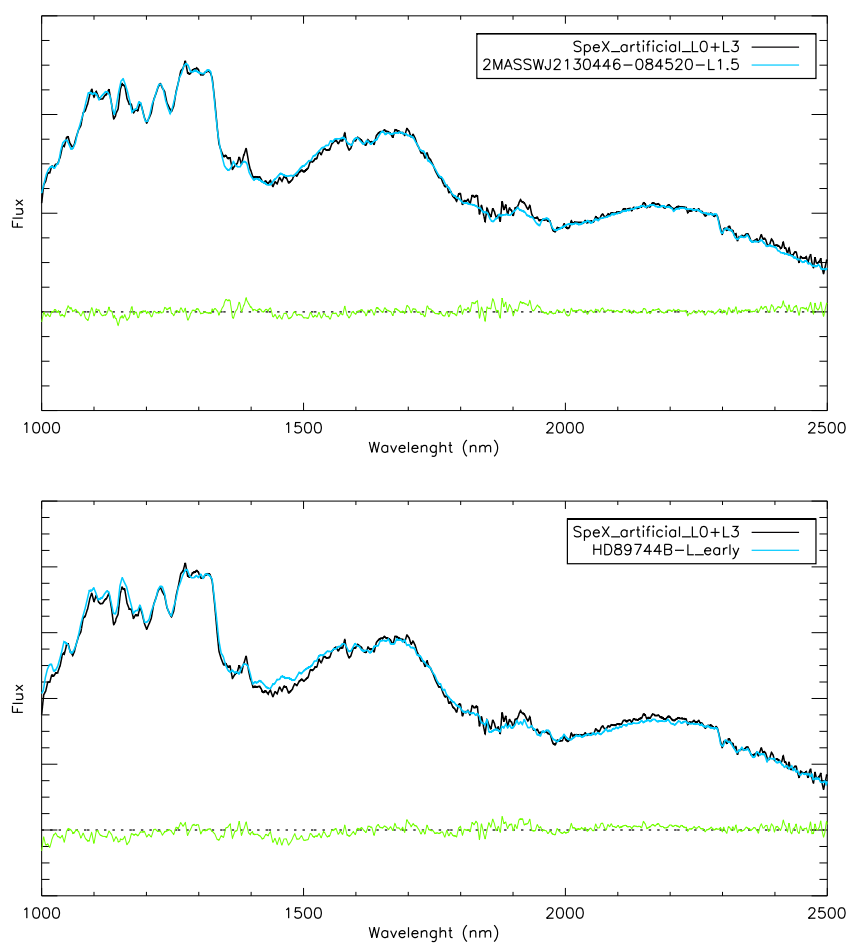


Figure 5.17: Best matches for a L0 (DENIS-PJ220002.05-303832.9B) + L3 (SDSSJ111320.16+343057.9) synthetic binary. We show the synthetic binary in black, the best matches in blue and residuals in green. The flux is $F(\lambda)$.

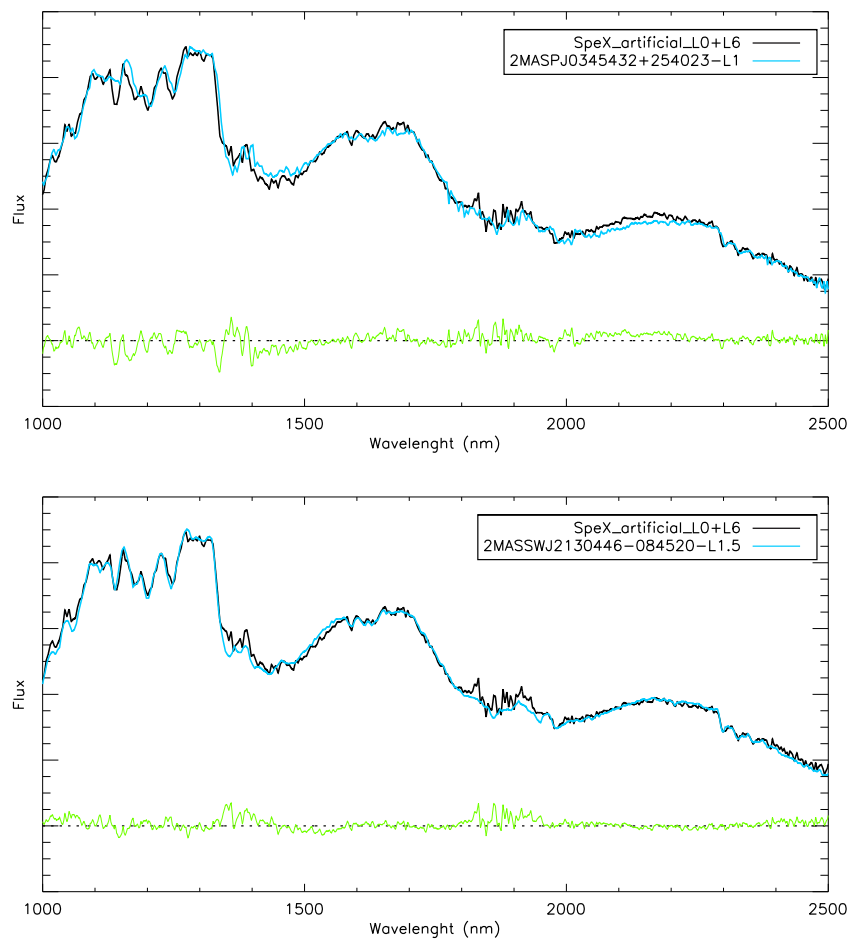


Figure 5.18: Best matches for a L0 (DENIS-PJ220002.05-303832.9B) + L6 (2MASSJ01303563) synthetic binary. The flux is $F(\lambda)$.

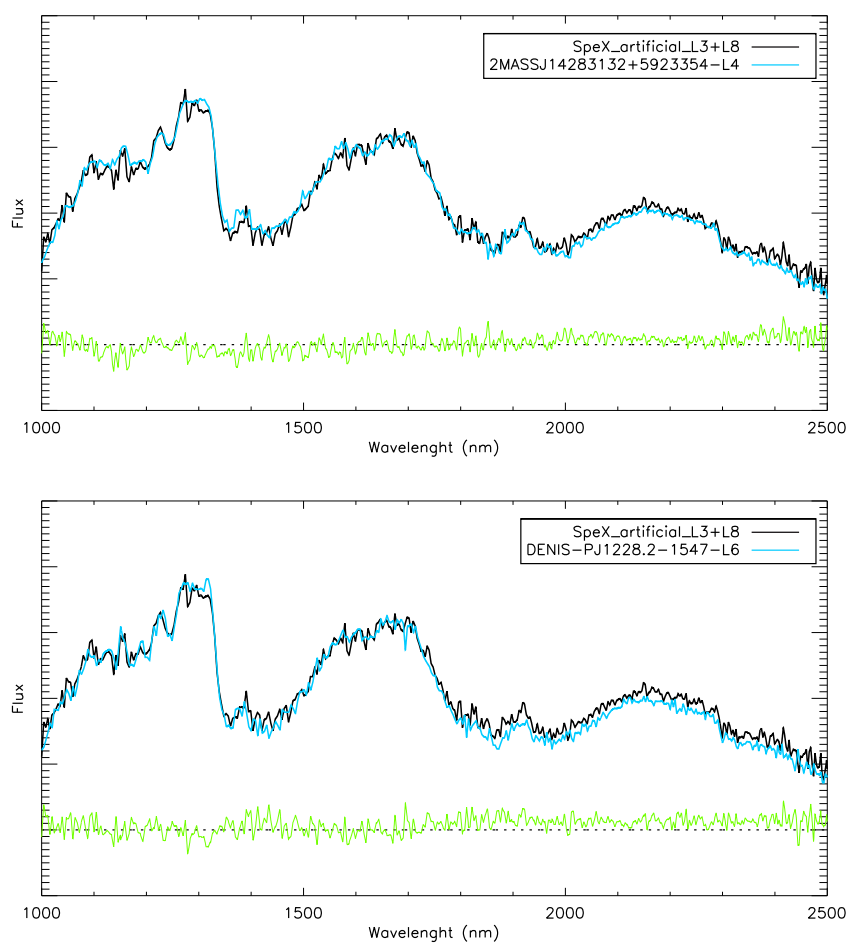


Figure 5.19: Best matches for a L3 (SDSSJ111320.16+343057.9) + L8 (SDSSJ121951.45+312849.4) synthetic binary. The flux is $F(\lambda)$.

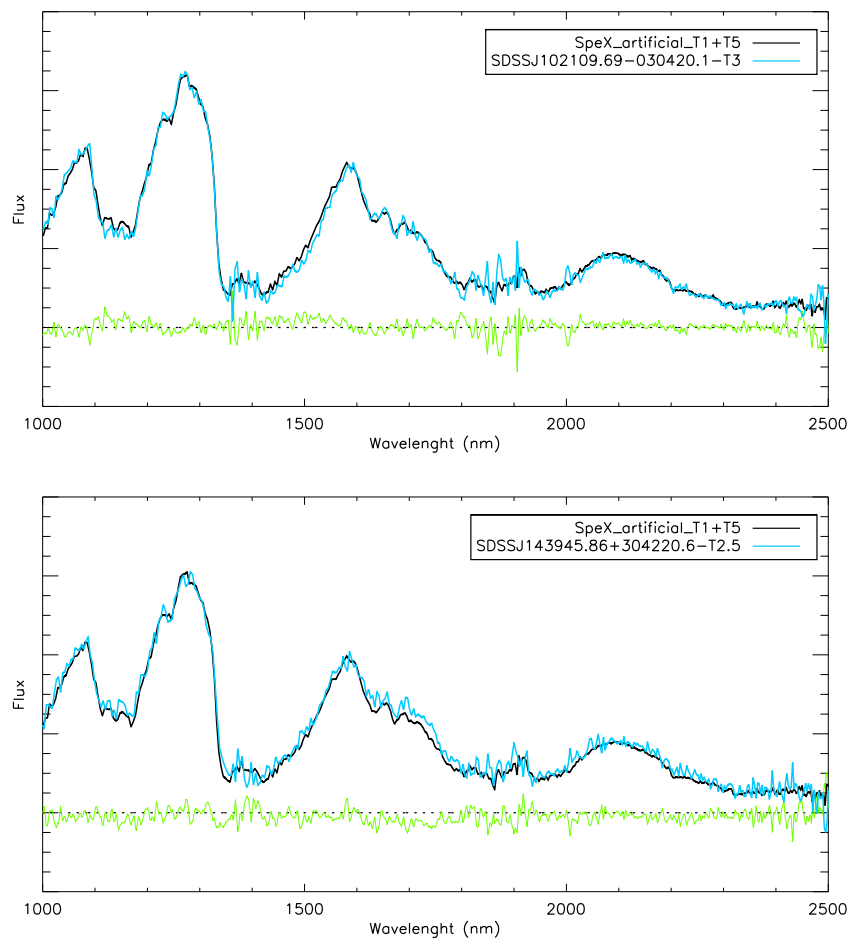


Figure 5.20: Best matches for a T1 (SDSSJ015141.69+124429.6) + T5 (2MASSJ04070885+1514565) synthetic binary. The flux is $F(\lambda)$.

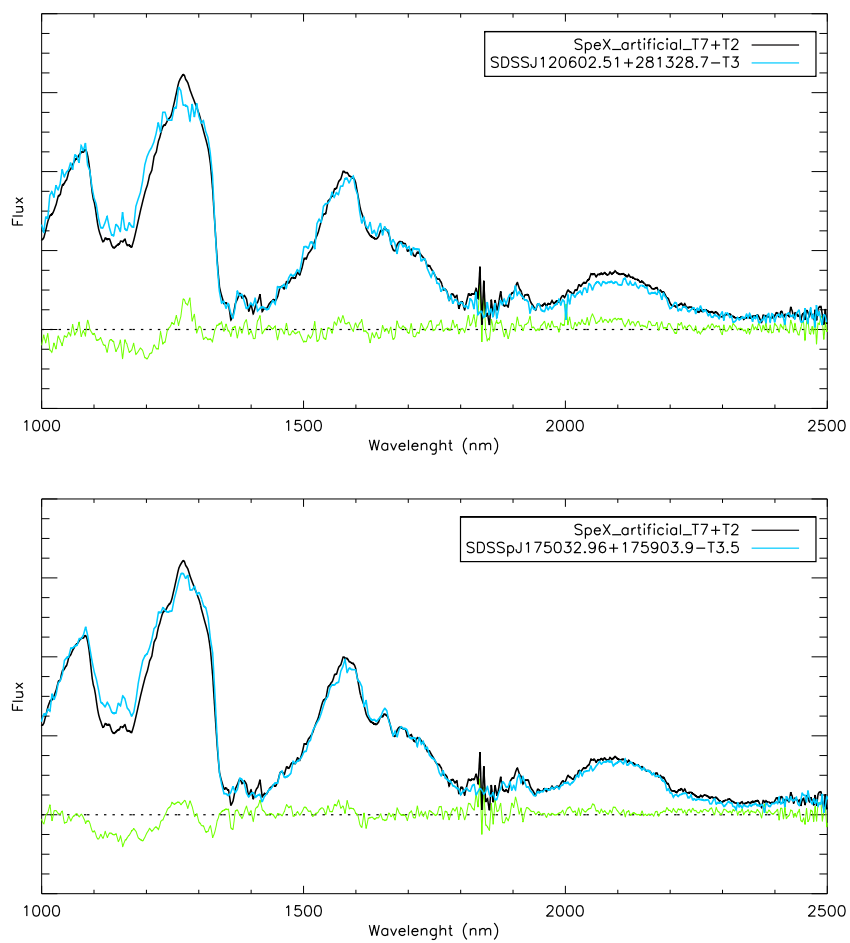
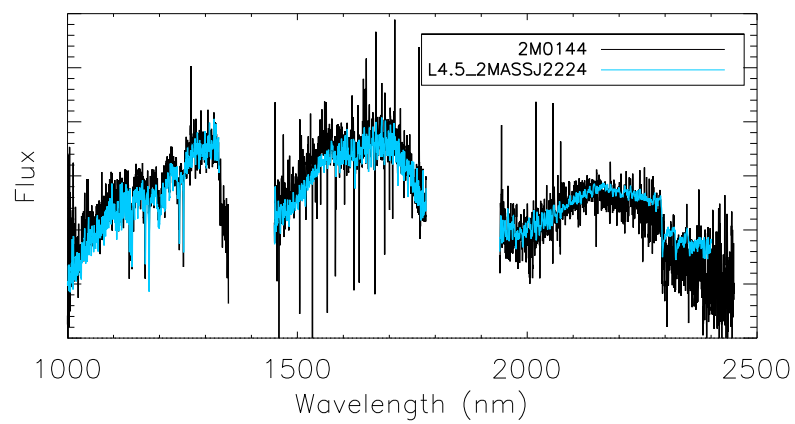
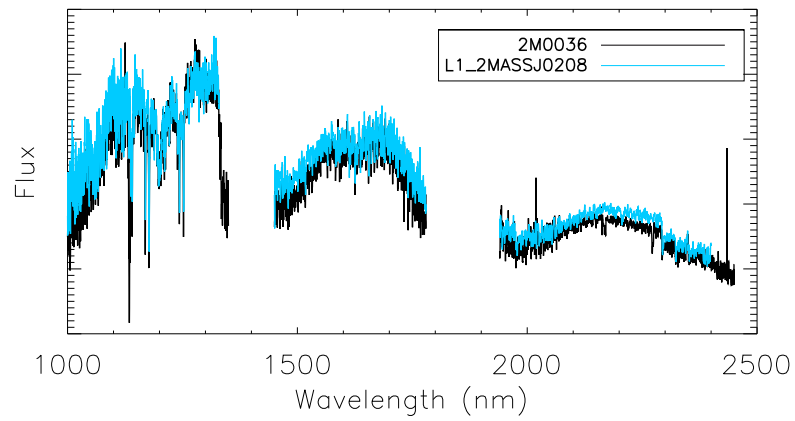
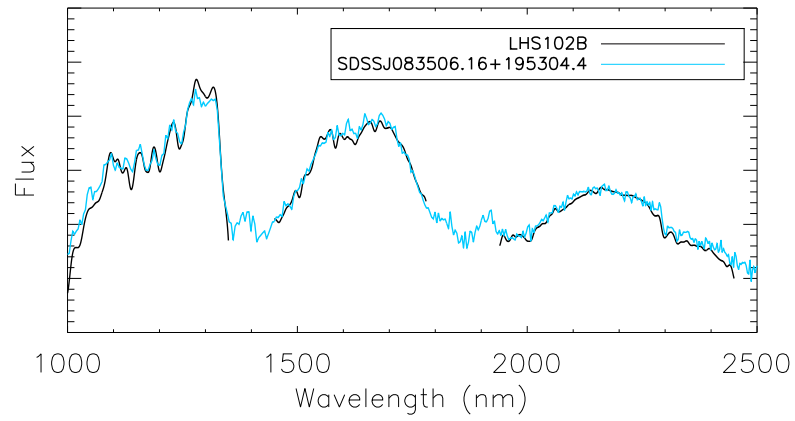


Figure 5.21: Best matches for a T7 (2MASSJ1553022+153236) + T2 (2MASSJ11220826-3512363) synthetic binary. The flux is $F(\lambda)$.



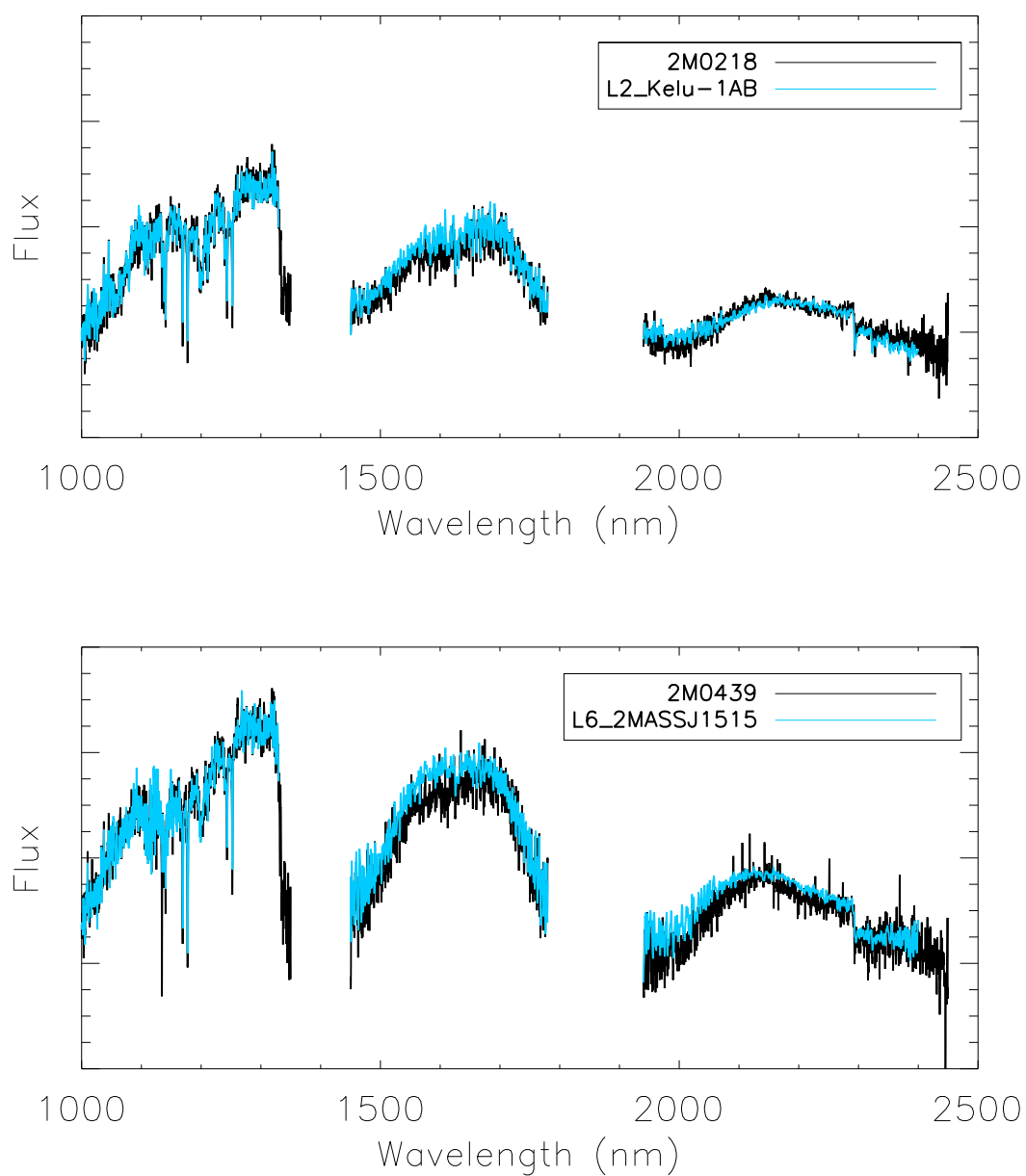


Figure 5.22: Best matches of our objects to spectra from spectral libraries listed in Table 5.7. The flux is $F(\lambda)$.

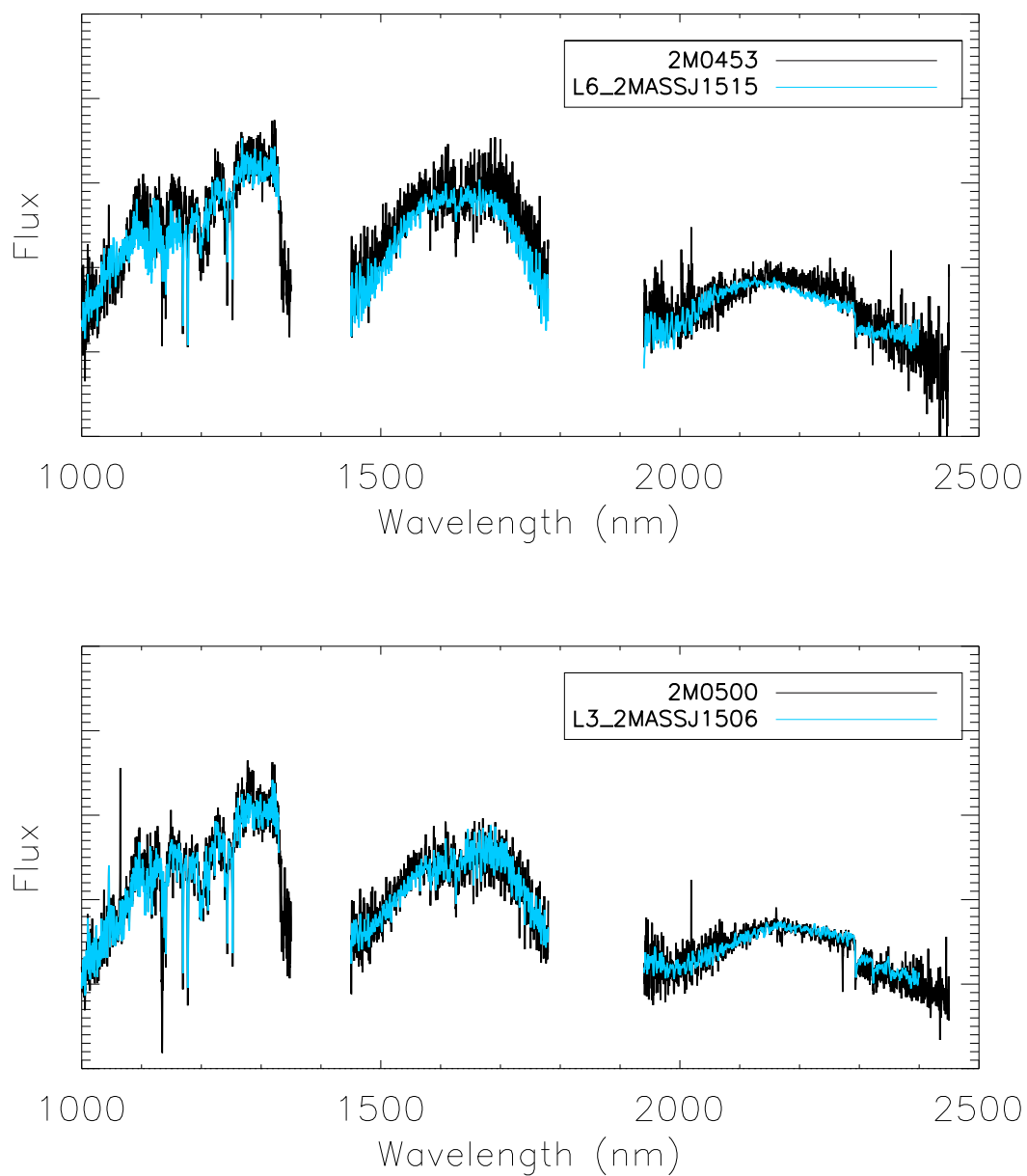


Figure 5.23: Best matches of our objects to spectra from spectral libraries listed in Table 5.7. The flux is $F(\lambda)$.

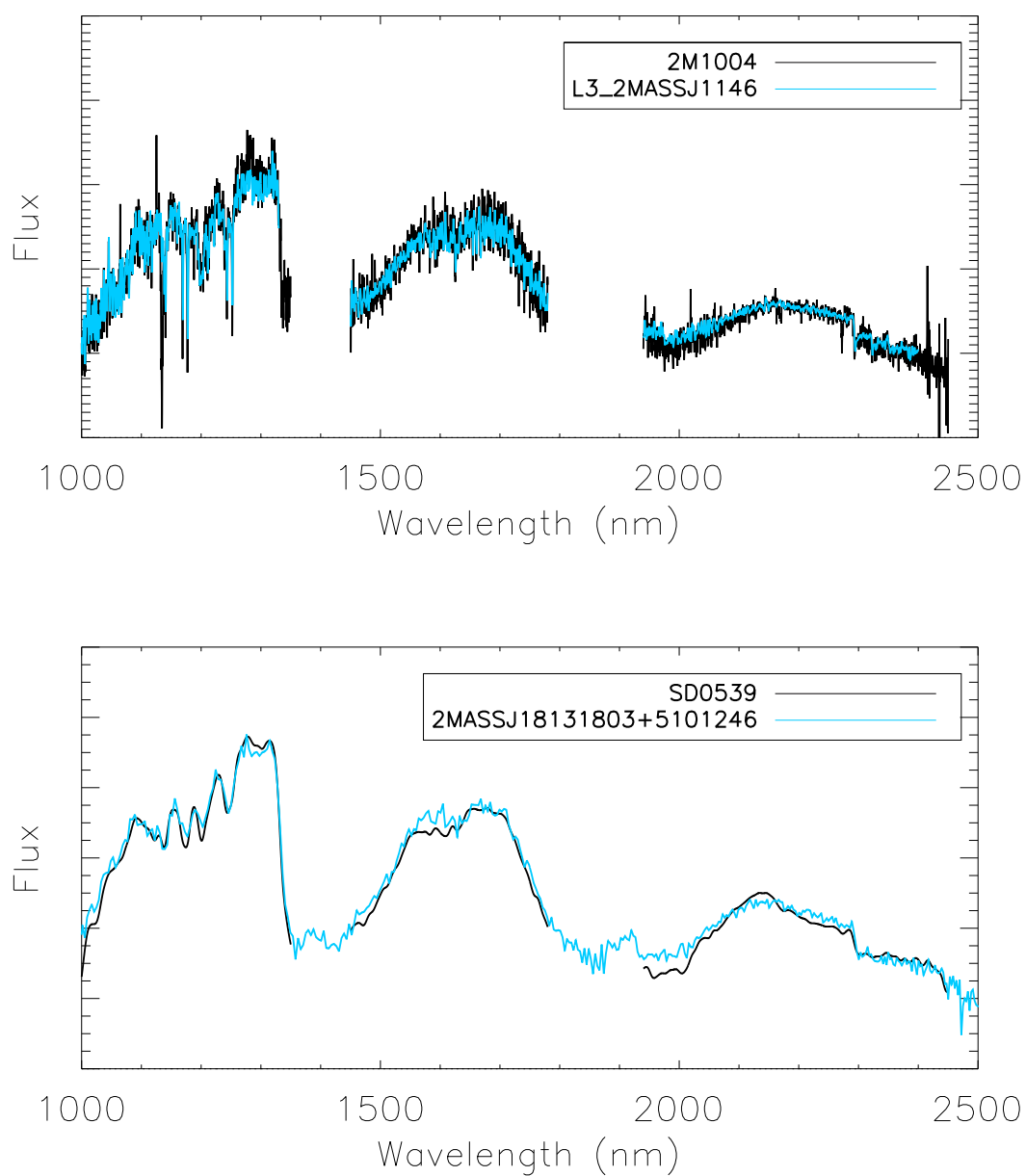


Figure 5.24: Best matches of our objects to spectra from spectral libraries listed in Table 5.7. The flux is $F(\lambda)$.

SUMMARY AND FUTURE WORK

The initial mass function determines the evolution of a population of stars and provides inputs for the constraint of the star formation theory. Since 1955 several authors have tried to measure the initial mass function in the stellar regime: [Salpeter \(1955\)](#), [Miller & Scalo \(1979\)](#), [Kroupa \(2001\)](#) and [Chabrier \(2003\)](#). Apart from [Chabrier \(2003\)](#), all measurements for the initial mass function have been limited to the stellar regime. The mass and the composition of a star determine its radius, luminosity and evolution in the Hertzsprung-Russell diagram. Therefore, if we know the initial mass function of a population for stars with similar composition, we can determine the evolution of this population. The empirical determination of the initial mass function in the substellar regime is one of the open problems in astrophysics.

Objects with masses below $75M_{\text{Jup}}$ are not able to sustain hydrogen fusion, therefore they never reach the main sequence. For these objects, their spectral types do not constrain masses and ages, so these two physical characteristics are degenerate for brown dwarfs. As objects with masses below $75M_{\text{Jup}}$ evolve, they cool down with time, thus, the determination of the initial mass function in the substellar regime becomes complicated.

In order to improve the determination of the initial mass function in the substellar regime, a proper physical characterization of brown dwarfs is necessary, but also an improvement of atmospheric and evolutionary models, which requires in the end the empirical characterization of brown dwarfs.

During this PhD thesis I characterized a sample of brown dwarfs using different techniques:

In Chapter 3, based on [Manjavacas et al. \(2013\)](#), we calculated absolute distances for six late-T brown dwarfs with spectral types between T2.5 and T8 and photometric distances smaller than 25 pc. Parallax is a direct measurement that allow us to identify the effect of secondary param-

eters in brown dwarf atmospheres, like metallicity, gravity, binarity etc. To calculate absolute distances, we observed our objects in the near infrared for 27 months using Omega2000 at the 3.5 m telescope in Calar Alto, Spain. For every epoch, we calculated the position for our targets with respect to the rest of the sources in the field, and the offset of the target with respect to the first epoch. This allow us to calculate the apparent trajectory of our objects and derive the relative parallax for each object, calculated using field stars as a reference frame. Nevertheless, field stars in our images have measurable parallaxes, as they are relatively close to the Earth, although further than our targets. To estimate the average value of the parallax for the field stars, we identified extragalactic sources in our fields, and we calculated the average of the parallax of the field stars with respect to extragalactic sources. Finally, we calculated absolute parallaxes for our objects with a precision between 5% and 9%. We plot our objects in a color-magnitude diagram with other brown dwarfs with known parallaxes. We calculated the luminosity for all targets and we found that the photometric distance and the trigonometric distance for one of our targets was not consistent. This disagreement suggests that this object might be a binary system.

In Chapter 4, based on [Manjavacas et al. \(2014\)](#), we sought to confirm the youth of a selected sample of seven M-L transition brown dwarfs. Young brown dwarfs usually have lower gravity compared to their older counterparts, as they are still contracting. Low gravity modifies brown dwarf spectra: they are redder in the near infrared, their alkali lines are weaker and their H-bands have a triangular shape. We acquired near infrared spectroscopy of these objects using ISAAC at the VLT. We test the youth of our targets in several manners: first, we compared their spectra with other well-characterized brown dwarf spectra. These comparison spectra belong to young brown dwarfs, field brown dwarfs and young companion brown dwarfs. We found matches to young brown dwarfs or young companion brown dwarfs for most of our targets. Object 2M2322 had a better match to a planetary-mass companion. Second, we calculated the equivalent widths of alkali lines for our objects and for the comparison spectra from the libraries. All targets beside one, EROS-MP 0032, had equivalent widths consistent with young objects. [Gagné et al. \(2013\)](#) calculated the probability of EROS-MP 0032 belonging to a young moving group, and found EROS-MP 0032 belong to β -Pictoris moving group (23 ± 3 Myr, [Mamajek & Bell \(2014\)](#)) with 91.8% confidence. Nevertheless, spectral characteristics of this object are not typical for such a young age. In the last part of Chapter 4, we test if the BT-Settl 2010 and 2013 are able to reproduce the spectra of such young objects in the M-L transition. In many cases the spectra were better reproduced by models with super-solar metallicity, pointing to a lack of dust in the models. A modification of the sedimentation rate might solve this problem.

In Chapter 5, based on [Manjavacas et al. \(2014b, submitted\)](#), we searched for brown dwarf binaries, in order to refine the completeness of the brown dwarf binarity fraction. The refinement of the binary fraction may help to understand the substellar formation mechanisms. We obtained X-Shooter spectra at the VLT in the optical and in the near infrared of 22 brown dwarfs with

spectral types between L3 and T7. We searched for brown dwarf binaries with different spectral types using spectral indices. We also compared our spectra to spectra of single brown dwarfs, and to spectra of artificial binaries constructed using spectra of two single brown dwarfs of different spectral types. We attempted to search for potential brown dwarf binaries with similar spectral type by comparing these spectra to single spectra and spectra of artificial binaries, and we conclude that we cannot find similar spectral type brown dwarf binaries using this method. We also calculated the equivalent widths of alkali lines of our targets in the optical and the near infrared and we compared them with the equivalent widths of other brown dwarfs from spectral libraries. We conclude that, in general, there is no significant difference between the equivalent widths of alkali lines of binary candidates and the rest of the sample. In order to find similar spectral type brown dwarf binaries, either radial velocities or parallaxes are needed.

In this PhD thesis, I contributed to the physical characterization of 35 brown dwarfs in total, deriving distances using trigonometric parallaxes, estimating ages through the study of young brown dwarf spectra and searching for close binaries to better constrain the brown dwarf binary fraction. Parallaxes allow us to discover binary systems and to potentially establish moving group membership for brown dwarfs, constraining ages. The study of young brown dwarf spectra and the refinement of the brown dwarf binary fraction shed light into the mechanisms that form brown dwarfs. The results of this PhD thesis, will therefore contribute to the determination of the initial mass function in the substellar regime.

In the last years, the first Y brown dwarfs, with estimated temperatures of few hundreds of kelvins, have been discovered. Nevertheless, they are so faint, that spectra with even moderate resolution are difficult to obtain. Atmospheric models claim that water should be present in their atmospheres, but this fact has not yet been confirmed by observations. With the discovery of Y-dwarfs, the missing link between stars and planets has been found. Furthermore, the frontier between exoplanets and brown dwarfs have been also blurred, as some exoplanets and young brown dwarfs share common spectral characteristics, as is the case object 2MASSJ232252.99.

In summer 2016, trigonometric distances for hundreds of brown dwarfs will become available with the first Gaia data release. Gaia distances will be essential to calculate luminosities, to discover brown dwarf binaries, refine the binary fraction and constrain the formation mechanisms through which brown dwarfs form. Gaia parallaxes will allow us to improve the kinematics of these objects, and establish moving group membership for these objects, constraining ages at the same time.

In fall 2018 the James Webb Space Telescope (JWST) will be launched. JWST will provide near infrared imaging and spectroscopy from the $0.6 \mu\text{m}$ to $5 \mu\text{m}$, allowing the scientific community to obtain high quality imaging and spectra from space in the wavelength range which brown dwarfs emit most of their flux.

In 2022, the 39.3 m European Extremely Large Telescope (E-ELT) will revolutionize all the fields of Astronomy. The E-ELT will have several instruments that will be particularly important in brown dwarf science: specifically, METIS (mid-infrared imager and spectrograph) and MICADO (diffraction-limited near infrared camera). These instruments will enable high resolution spectroscopy of brown dwarfs in the infrared.

Finally, in 2024, PLATO (PLanetary Transits and Oscillations of stars) satellite will be launched. The main objective of PLATO will be searching for Earth-sized planets and super-Earths in the habitable zone around solar-type stars, measure solar oscillation in the host stars of exoplanets and measure oscillations of classical pulsators. Nevertheless, PLATO will also be able to measure variability in brown dwarfs and giant planets with enough accuracy to study the atmospheres of these objects.

These future instruments will help, therefore, to break the mass-age degeneracy in brown dwarfs, which will provide inputs to test evolutionary and atmospheric models and constraining the initial mass function in the substellar regime.

In the next years, brown dwarf science will likely progress quickly due to these upcoming instruments, likely shedding light on many as yet unsolved questions in the field.

ACKNOWLEDGMENTS

I remember the first time I paid attention to the sky when I was still living in my small village in La Mancha (Spain). I was really delighted by such a spectacle and I started wondering about what mysteries all those stars were hiding. I looked at the Milky Way and I imagined thousands of new worlds populated by other people around those small points of light that crossed the sky. That year, uncle Rafa gave me as Christmas present my first telescope, he didn't know what he was doing...

With the end of my PhD thesis, I accomplish the dream of that eight-year-old girl who wanted to discover what the Universe was.

In the first place, I want to thank Jose Caballero and Orlagh Creevey, without their support and encouragement I would have never come to Heidelberg. I must confess that when Jose suggested me to apply to the IMPRS I was a bit scared about the idea of coming to Germany... now I do not want to leave!

I want also to thank my supervisors, Thomas Henning, Bertrand Goldman and Sabine Reffert for supporting me and helping me during these three years, but also for pressuring me when it was necessary. I admit that sometimes I need a bit of pressure to make me give 100% of what I am able to.

This PhD thesis would not have been possible without the help and the motivation provided by some of my collaborators and colleagues: Mickaël Bonnefoy, Josh Schlieder, Juan Alcalá, Beth Biller, Esther Buenzli, Maria Rosa Zapatero Osorio and Víctor Béjar. I really learned a lot from you. I specially thank Beth Biller for correcting my Spanglish.

If I had to summarize the last three years using words I will probably need other 100 pages, so

I will try to summarize them with some numbers instead: one PhD thesis (I hope), one new language (German) and the missing half of other (English), one dialect (Chilean Spanish), 82000 km of travels (more than two times around the world), more than 300 km swum, a uncountable number of friends from more than 10 different nationalities, an infinite number of laughs, and of course many memorable parties, and barbecues at the Neckarwisse.

I want to thank especially to Edu Zornoza, David López-Rey and Estela Fernández for supporting me in those moments in which I felt down and disappointed by science. You are the very best!

I also thank Cristina García, Mauricio Ortiz, Mauricio Carrasco, Jorge Abreu, Eduardo Banãdos, Maria José Cordero, Paulo Miles, Tobias Albertsson, Taisiya Kopytova, Aiara Gomes, Peter Zeidler and Akin Yildirim, for listening all my problems day by day (that is hard, I know!). I specially thank Peter Zeidler for the translation of the abstract to German.

I will have for sure a wonderful memory of these three years, and I will probably remember them as the best three years of my life. Now what I hope, is to keep the contact with all the wonderful people I met here and with all the wonderful science I learned.

BIBLIOGRAPHY

- Alcalá, J. M., et al. 2008, *ApJ*, 676, 427
- . 2014, *A&A*, 561, A2
- Allard, F., Allard, N. F., Homeier, D., Kielkopf, J., McCaughrean, M. J., & Spiegelman, F. 2007, *A&A*, 474, L21
- Allard, F., Guillot, T., Ludwig, H.-G., Hauschildt, P. H., Schweitzer, A., Alexander, D. R., & Ferguson, J. W. 2003, in *IAU Symposium*, Vol. 211, *Brown Dwarfs*, ed. E. Martín, 325
- Allard, F., & Hauschildt, P. H. 1995, *ApJ*, 445, 433
- Allard, F., Hauschildt, P. H., Alexander, D. R., Tamanai, A., & Schweitzer, A. 2001, *ApJ*, 556, 357
- Allard, F., Homeier, D., & Freytag, B. 2011, in *Astronomical Society of the Pacific Conference Series*, Vol. 448, *16th Cambridge Workshop on Cool Stars, Stellar Systems, and the Sun*, ed. C. Johns-Krull, M. K. Browning, & A. A. West, 91
- Allard, F., Homeier, D., & Freytag, B. 2012a, *Royal Society of London Philosophical Transactions Series A*, 370, 2765
- Allard, F., Homeier, D., & Freytag, B. 2012b, in *IAU Symposium*, Vol. 282, *IAU Symposium*, ed. M. T. Richards & I. Hubeny, 235–242
- Allard, F., Homeier, D., Freytag, B., & Sharp, C. M. 2012c, in *EAS Publications Series*, Vol. 57, *EAS Publications Series*, ed. C. Reylé, C. Charbonnel, & M. Schultheis, 3–43
- Allen, P. R. 2007, *ApJ*, 668, 492
- Allen, P. R., Koerner, D. W., McElwain, M. W., Cruz, K. L., & Reid, I. N. 2007, *AJ*, 133, 971
- Allers, K. N., Kessler-Silacci, J. E., Cieza, L. A., & Jaffe, D. T. 2006a, *ApJ*, 644, 364
- . 2006b, *ApJ*, 644, 364
- Allers, K. N., & Liu, M. C. 2007, in *Bulletin of the American Astronomical Society*, Vol. 39,

- American Astronomical Society Meeting Abstracts, 103.15
- Allers, K. N., & Liu, M. C. 2013, ArXiv e-prints
- Allers, K. N., Liu, M. C., Dupuy, T. J., & Cushing, M. C. 2010, *ApJ*, 715, 561
- Allers, K. N., et al. 2007, *ApJ*, 657, 511
- . 2009, *ApJ*, 697, 824
- Andrei, A. H., et al. 2011, *AJ*, 141, 54
- Antonova, A., Hallinan, G., Doyle, J. G., Yu, S., Kuznetsov, A., Metodieva, Y., Golden, A., & Cruz, K. L. 2013, *A&A*, 549, A131
- Apai, D., Radigan, J., Buenzli, E., Burrows, A., Reid, I. N., & Jayawardhana, R. 2013, *ApJ*, 768, 121
- Artigau, É., Bouchard, S., Doyon, R., & Lafrenière, D. 2009, *ApJ*, 701, 1534
- Artigau, É., Doyon, R., Lafrenière, D., Nadeau, D., Robert, J., & Albert, L. 2006, *ApJ*, 651, L57
- Asplund, M., Grevesse, N., Sauval, A. J., & Scott, P. 2009, *ARA&A*, 47, 481
- Bailer-Jones, C. A., Bizenberger, P., & Storz, C. 2000, in *Society of Photo-Optical Instrumentation Engineers (SPIE) Conference Series*, Vol. 4008, *Society of Photo-Optical Instrumentation Engineers (SPIE) Conference Series*, ed. M. Iye & A. F. Moorwood, 1305–1316
- Baraffe, I., Chabrier, G., Allard, F., & Hauschildt, P. H. 1998a, *A&A*, 337, 403
- . 1998b, *A&A*, 337, 403
- Bardalez Gagliuffi, D. C., et al. 2014a, *ApJ*, 794, 143
- . 2014b, ArXiv e-prints
- Barenfeld, S. A., Bubar, E. J., Mamajek, E. E., & Young, P. A. 2013, *ApJ*, 766, 6
- Barman, T. S., Macintosh, B., Ky, Q. M., & Marois, C. 2011, *ApJ*, 733, 65
- Barrado y Navascués, D. 2006, *A&A*, 459, 511
- Basri, G., Marcy, G. W., & Graham, J. R. 1995, in *Bulletin of the American Astronomical Society*, Vol. 27, *American Astronomical Society Meeting Abstracts #186*, 1214
- Bastian, N., Covey, K. R., & Meyer, M. R. 2010, *ARA&A*, 48, 339
- Becklin, E. E., & Zuckerman, B. 1988, *Nature*, 336, 656
- Béjar, V. J. S., Zapatero Osorio, M. R., Pérez-Garrido, A., Álvarez, C., Martín, E. L., Rebolo, R., Villó-Pérez, I., & Díaz-Sánchez, A. 2008, *ApJ*, 673, L185
- Bertin, E. 2006, in *Astronomical Society of the Pacific Conference Series*, Vol. 351, *Astronomical Data Analysis Software and Systems XV*, ed. C. Gabriel, C. Arviset, D. Ponz, & S. Enrique, 112
- Bertin, E., & Arnouts, S. 1996, *A&AS*, 117, 393
- Bonnefoy, M., Chauvin, G., Lagrange, A.-M., Rojo, P., Allard, F., Pinte, C., Dumas, C., & Homeier, D. 2013a, ArXiv e-prints

- . 2014, *A&A*, 562, A127
- Bonnefoy, M., Chauvin, G., Rojo, P., Allard, F., Lagrange, A.-M., Homeier, D., Dumas, C., & Beuzit, J.-L. 2010, *A&A*, 512, A52
- Bonnefoy, M., et al. 2013b, ArXiv e-prints
- . 2013c, *A&A*, 555, A107
- Borysow, A., Jorgensen, U. G., & Zheng, C. 1997, *A&A*, 324, 185
- Bowler, B. P., Liu, M. C., Kraus, A. L., Mann, A. W., & Ireland, M. J. 2011, *ApJ*, 743, 148
- Bowler, B. P., Liu, M. C., Shkolnik, E. L., & Dupuy, T. J. 2013, ArXiv e-prints
- Bowler, B. P., Liu, M. C., Shkolnik, E. L., Dupuy, T. J., Cieza, L. A., Kraus, A. L., & Tamura, M. 2012, *ApJ*, 753, 142
- Briceño, C., Luhman, K. L., Hartmann, L., Stauffer, J. R., & Kirkpatrick, J. D. 2002, *ApJ*, 580, 317
- Burgasser, A. J. 2004, *ApJS*, 155, 191
- . 2007, *ApJ*, 659, 655
- Burgasser, A. J., Bardalez-Gagliuffi, D. C., & Gizis, J. E. 2011, *AJ*, 141, 70
- Burgasser, A. J., Cruz, K. L., Cushing, M., Gelino, C. R.,Looper, D. L., Faherty, J. K., Kirkpatrick, J. D., & Reid, I. N. 2010, *ApJ*, 710, 1142
- Burgasser, A. J., Cruz, K. L., & Kirkpatrick, J. D. 2007, *ApJ*, 657, 494
- Burgasser, A. J., Geballe, T. R., Golimowski, D. A., Leggett, S. K., Kirkpatrick, J. D., Knapp, G. R., & Fan, X. 2003, in *IAU Symposium*, Vol. 211, *Brown Dwarfs*, ed. E. Martín, 377
- Burgasser, A. J., Geballe, T. R., Leggett, S. K., Kirkpatrick, J. D., & Golimowski, D. A. 2006, *ApJ*, 637, 1067
- Burgasser, A. J., Marley, M. S., Ackerman, A. S., Saumon, D., Lodders, K., Dahn, C. C., Harris, H. C., & Kirkpatrick, J. D. 2002a, *ApJ*, 571, L151
- Burgasser, A. J., McElwain, M. W., Kirkpatrick, J. D., Cruz, K. L., Tinney, C. G., & Reid, I. N. 2004, *AJ*, 127, 2856
- Burgasser, A. J., Reid, I. N., Leggett, S. K., Kirkpatrick, J. D., Liebert, J., & Burrows, A. 2005, *ApJ*, 634, L177
- Burgasser, A. J., Vrba, F. J., Lépine, S., Munn, J. A., Luginbuhl, C. B., Henden, A. A., Guetter, H. H., & Canzian, B. C. 2008, *ApJ*, 672, 1159
- Burgasser, A. J., et al. 2002b, *ApJ*, 564, 421
- Burningham, B., et al. 2010, *MNRAS*, 406, 1885
- . 2013, *MNRAS*, 433, 457
- Burrows, A., Hubbard, W. B., Lunine, J. I., & Liebert, J. 2001, *Reviews of Modern Physics*, 73, 719
- Burrows, A., Sudarsky, D., & Hubeny, I. 2006, *ApJ*, 640, 1063

- Burrows, A., et al. 1997a, *ApJ*, 491, 856
— 1997b, *ApJ*, 491, 856
Caballero, J. A., et al. 2007, *A&A*, 470, 903
Caffau, E., Ludwig, H.-G., Steffen, M., Freytag, B., & Bonifacio, P. 2011, *Sol. Phys.*, 268, 255
Castro, P. J., Gizis, J. E., Harris, H. C., Mace, G. N., Kirkpatrick, J. D., McLean, I. S., Pattarakijwanich, P., & Skrutskie, M. F. 2013, *ApJ*, 776, 126
Chabrier, G. 2003, *ApJ*, 586, L133
Chabrier, G., & Baraffe, I. 1997, *A&A*, 327, 1039
Chabrier, G., Baraffe, I., Allard, F., & Hauschildt, P. 2000, *ApJ*, 542, 464
Chiu, K., Fan, X., Leggett, S. K., Golimowski, D. A., Zheng, W., Geballe, T. R., Schneider, D. P., & Brinkmann, J. 2006, *AJ*, 131, 2722
Close, L. M., Thatte, N., Nielsen, E. L., Abuter, R., Clarke, F., & Tecza, M. 2007, *ApJ*, 665, 736
Cohen, M., Wheaton, W. A., & Megeath, S. T. 2003a, *AJ*, 126, 1090
— 2003b, *AJ*, 126, 1090
Costa, E., Méndez, R. A., Jao, W.-C., Henry, T. J., Subasavage, J. P., & Ianna, P. A. 2006, *AJ*, 132, 1234
Cruz, K. L., Faherty, J., Kirkpatrick, D., & Burgasser, A. J. 2007, in *Bulletin of the American Astronomical Society*, Vol. 39, American Astronomical Society Meeting Abstracts #210, 225
Cruz, K. L., Kirkpatrick, J. D., & Burgasser, A. J. 2009a, *AJ*, 137, 3345
— 2009b, *AJ*, 137, 3345
Cruz, K. L., Reid, I. N., Liebert, J., Kirkpatrick, J. D., & Lowrance, P. J. 2003, *AJ*, 126, 2421
Cushing, M. C., Rayner, J. T., Davis, S. P., & Vacca, W. D. 2003, *ApJ*, 582, 1066
Cushing, M. C., Rayner, J. T., & Vacca, W. D. 2005, *ApJ*, 623, 1115
Cushing, M. C., et al. 2008, *ApJ*, 678, 1372
— 2011, *ApJ*, 743, 50
Cutri, R. M., & et al. 2012, *VizieR Online Data Catalog*, 2311, 0
Cutri, R. M., et al. 2003, *VizieR Online Data Catalog*, 2246, 0
Dahn, C. C., et al. 2002a, *AJ*, 124, 1170
— 2002b, *AJ*, 124, 1170
Day-Jones, A. C., et al. 2013, *MNRAS*, 430, 1171
Deacon, N. R., Nelemans, G., & Hambly, N. C. 2008, *A&A*, 486, 283
Devillard, N., Jung, Y., & Cuby, J.-G. 1999, *The Messenger*, 95, 5
Dupuy, T. J., & Liu, M. C. 2012a, *ApJS*, 201, 19
— 2012b, *ApJS*, 201, 19
Dupuy, T. J., Liu, M. C., Bowler, B. P., Cushing, M. C., Helling, C., Witte, S., & Hauschildt, P.

- 2010, *ApJ*, 721, 1725
- Dupuy, T. J., Liu, M. C., & Ireland, M. J. 2009, *ApJ*, 699, 168
- . 2014, *ApJ*, 790, 133
- Duquennoy, A., & Mayor, M. 1991, *A&A*, 248, 485
- Ellis, S. C., Tinney, C. G., Burgasser, A. J., Kirkpatrick, J. D., & McElwain, M. W. 2005, *AJ*, 130, 2347
- Faherty, J. K., Burgasser, A. J., Cruz, K. L., Shara, M. M., Walter, F. M., & Gelino, C. R. 2009a, *AJ*, 137, 1
- . 2009b, *AJ*, 137, 1
- Faherty, J. K., Rice, E. L., Cruz, K. L., Mamajek, E. E., & Núñez, A. 2013, *AJ*, 145, 2
- Faherty, J. K., Tinney, C. G., Skemer, A., & Monson, A. J. 2014, *ApJ*, 793, L16
- Faherty, J. K., et al. 2012a, *ApJ*, 752, 56
- . 2012b, *ApJ*, 752, 56
- . 2012c, *ApJ*, 752, 56
- Fitzpatrick, E. L. 1999, *PASP*, 111, 63
- Folkes, S. L., Pinfield, D. J., Kendall, T. R., & Jones, H. R. A. 2007, *MNRAS*, 378, 901
- Fruchter, A. S., & Hook, R. N. 2002, *PASP*, 114, 144
- Gagné, J., Lafrenière, D., Doyon, R., Malo, L., & Artigau, É. 2013, *ArXiv e-prints*
- Gelino, C. R., Marley, M. S., Holtzman, J. A., Ackerman, A. S., & Lodders, K. 2002, *ApJ*, 577, 433
- Gizis, J. E. 2002, *ApJ*, 575, 484
- Gizis, J. E., Reid, I. N., Knapp, G. R., Liebert, J., Kirkpatrick, J. D., Koerner, D. W., & Burgasser, A. J. 2003, *AJ*, 125, 3302
- Goldman, B., Bouy, H., Zapatero Osorio, M. R., Stumpf, M. B., Brandner, W., & Henning, T. 2008, *A&A*, 490, 763
- Goldman, B., Marsat, S., Henning, T., Clemens, C., & Greiner, J. 2010, *MNRAS*, 405, 1140
- Golimowski, D. A., et al. 2004a, *AJ*, 127, 3516
- . 2004b, *AJ*, 127, 3516
- Goorvitch, D. 1994, *ApJS*, 95, 535
- Goorvitch, D., & Chackerian, Jr., C. 1994a, *ApJS*, 91, 483
- . 1994b, *ApJS*, 92, 311
- Gorlova, N. I., Meyer, M. R., Rieke, G. H., & Liebert, J. 2003, *ApJ*, 593, 1074
- Hargreaves, R. J., Hinkle, K. H., Bauschlicher, Jr., C. W., Wende, S., Seifahrt, A., & Bernath, P. F. 2010, *AJ*, 140, 919
- Hayashi, C., & Nakano, T. 1963, *Progress of Theoretical Physics*, 30, 460

- Hayes, D. S. 1985, in IAU Symposium, Vol. 111, Calibration of Fundamental Stellar Quantities, ed. D. S. Hayes, L. E. Pasinetti, & A. G. D. Philip, 225–249
- Hewett, P. C., Warren, S. J., Leggett, S. K., & Hodgkin, S. T. 2006, MNRAS, 367, 454
- Hog, E., et al. 2000, VizieR Online Data Catalog, 1259, 0
- Homeier, D., Hauschildt, P., & Allard, F. 2003, in ASP Conference Series, Vol. 288, Stellar Atmosphere Modeling, Proceedings of an International Workshop held 8-12 April 2002 in Tübingen, Germany, ed. I. Hubeny, D. Mihalas, & K. Werner (San Francisco: Astronomical Society of the Pacific), 357–360
- Ireland, M. J., Kraus, A., Martinache, F., Law, N., & Hillenbrand, L. A. 2011, ApJ, 726, 113
- Jameson, R. F., Casewell, S. L., Bannister, N. P., Lodieu, N., Keresztes, K., Dobbie, P. D., & Hodgkin, S. T. 2008, MNRAS, 384, 1399
- Jarrett, T. H., et al. 2011, ApJ, 735, 112
- Jayawardhana, R., & Ivanov, V. D. 2006, ApJ, 647, L167
- Joergens, V. 2008, A&A, 492, 545
- Kaczmarczik, M. C., Richards, G. T., Mehta, S. S., & Schlegel, D. J. 2009, AJ, 138, 19
- Kastner, J. H., Zuckerman, B., Weintraub, D. A., & Forveille, T. 1997, Science, 277, 67
- Kirkpatrick, J. D. 2005, ARA&A, 43, 195
- Kirkpatrick, J. D., Barman, T. S., Burgasser, A. J., McGovern, M. R., McLean, I. S., Tinney, C. G., & Lowrance, P. J. 2006, ApJ, 639, 1120
- Kirkpatrick, J. D., Dahn, C. C., Monet, D. G., Reid, I. N., Gizis, J. E., Liebert, J., & Burgasser, A. J. 2001, AJ, 121, 3235
- Kirkpatrick, J. D., et al. 2008, ApJ, 689, 1295
- . 2010, ApJS, 190, 100
- . 2011, ApJS, 197, 19
- . 2012, ApJ, 753, 156
- Knapp, G. R., et al. 2004, AJ, 127, 3553
- Koen, C., Tanabé, T., Tamura, M., & Kusakabe, N. 2005a, MNRAS, 362, 727
- . 2005b, MNRAS, 362, 727
- Konopacky, Q. M., Barman, T. S., Macintosh, B. A., & Marois, C. 2013, Science, 339, 1398
- Konopacky, Q. M., Ghez, A. M., Barman, T. S., Rice, E. L., Bailey, III, J. I., White, R. J., McLean, I. S., & Duchêne, G. 2010, ApJ, 711, 1087
- Kroupa, P. 2001, MNRAS, 322, 231
- Kumar, S. S. 1963a, ApJ, 137, 1126
- . 1963b, ApJ, 137, 1121
- Kurucz, R. L. 1994, in Lecture Notes in Physics, Berlin Springer Verlag, Vol. 428, IAU Colloq.

- 146: Molecules in the Stellar Environment, ed. U. G. Jorgensen, 282
- Lafrenière, D., Jayawardhana, R., & van Kerkwijk, M. H. 2008a, *ApJ*, 689, L153
- . 2008b, *ApJ*, 689, L153
- . 2010a, *ApJ*, 719, 497
- . 2010b, *ApJ*, 719, 497
- Lane, B. F., Zapatero Osorio, M. R., Britton, M. C., Martín, E. L., & Kulkarni, S. R. 2001, *ApJ*, 560, 390
- Lang, D., Hogg, D. W., Mierle, K., Blanton, M., & Roweis, S. 2010, *AJ*, 139, 1782
- Lavigne, J.-F., Doyon, R., Lafrenière, D., Marois, C., & Barman, T. 2009, *ApJ*, 704, 1098
- Leggett, S. K., et al. 2000, *ApJ*, 536, L35
- Lépine, S., & Simon, M. 2009, *AJ*, 137, 3632
- Liebert, J., Kirkpatrick, J. D., Cruz, K. L., Reid, I. N., Burgasser, A., Tinney, C. G., & Gizis, J. E. 2003, *AJ*, 125, 343
- Lindgren, L. 1980, *A&A*, 89, 41
- Liu, M. C., Leggett, S. K., Golimowski, D. A., Chiu, K., Fan, X., Geballe, T. R., Schneider, D. P., & Brinkmann, J. 2006, *ApJ*, 647, 1393
- Liu, M. C., et al. 2013, ArXiv e-prints
- Lodieu, N., Hambly, N. C., Jameson, R. F., & Hodgkin, S. T. 2008, *MNRAS*, 383, 1385
- Looper, D. L., Gelino, C. R., Burgasser, A. J., & Kirkpatrick, J. D. 2008a, *ApJ*, 685, 1183
- Looper, D. L., Kirkpatrick, J. D., & Burgasser, A. J. 2007, *AJ*, 134, 1162
- Looper, D. L., et al. 2008b, *ApJ*, 686, 528
- Lovis, C., & Mayor, M. 2007, *A&A*, 472, 657
- Luhman, K. L. 1999, *ApJ*, 525, 466
- Luhman, K. L., Adame, L., D'Alessio, P., Calvet, N., Hartmann, L., Megeath, S. T., & Fazio, G. G. 2005a, *ApJ*, 635, L93
- . 2005b, *ApJ*, 635, L93
- Luhman, K. L., Peterson, D. E., & Megeath, S. T. 2004, *ApJ*, 617, 565
- Luhman, K. L., Stauffer, J. R., Muench, A. A., Rieke, G. H., Lada, E. A., Bouvier, J., & Lada, C. J. 2003, *ApJ*, 593, 1093
- Luhman, K. L., et al. 2007, *ApJ*, 654, 570
- Malo, L., Doyon, R., Lafrenière, D., Artigau, É., Gagné, J., Baron, F., & Riedel, A. 2013, *ApJ*, 762, 88
- Mamajek, E. E., & Bell, C. P. M. 2014, *MNRAS*, 445, 2169
- Manara, C. F., et al. 2013a, *A&A*, 551, A107
- . 2013b, *A&A*, 551, A107

- Manjavacas, E., Goldman, B., Reffert, S., & Henning, T. 2013, *A&A*, 560, A52
- Manjavacas, E., et al. 2014, *A&A*, 564, A55
- Marocco, F., et al. 2010, *A&A*, 524, A38
- . 2013a, ArXiv e-prints
- . 2013b, *AJ*, 146, 161
- Martín, E. L., Delfosse, X., Basri, G., Goldman, B., Forveille, T., & Zapatero Osorio, M. R. 1999, *AJ*, 118, 2466
- Martín, E. L., et al. 2010, *A&A*, 517, A53
- McLean, I. S., McGovern, M. R., Burgasser, A. J., Kirkpatrick, J. D., Prato, L., & Kim, S. S. 2003, *ApJ*, 596, 561
- Melnikov, S., & Eislöffel, J. 2012, *A&A*, 544, A111
- Metchev, S. A., & Hillenbrand, L. A. 2006, *ApJ*, 651, 1166
- Miller, G. E., & Scalo, J. M. 1979, *ApJS*, 41, 513
- Mohanty, S., Jayawardhana, R., Huélamo, N., & Mamajek, E. 2007, *ApJ*, 657, 1064
- Monet, D. G., Dahn, C. C., Vrba, F. J., Harris, H. C., Pier, J. R., Luginbuhl, C. B., & Ables, H. D. 1992, *AJ*, 103, 638
- Monet, D. G., et al. 2003, *AJ*, 125, 984
- Moorwood, A., et al. 1998, *The Messenger*, 94, 7
- Morales-Calderón, M., et al. 2006, *ApJ*, 653, 1454
- Mountain, C. M., Selby, M. J., Leggett, S. K., Blackwell, D. E., & Petford, A. D. 1985, *A&A*, 151, 399
- Murray, D. N., et al. 2011, *MNRAS*, 414, 575
- Mutchler, M., & Fruchter, A. 1997, in *Bulletin of the American Astronomical Society*, Vol. 29, American Astronomical Society Meeting Abstracts, 1271
- Nakajima, T., Oppenheimer, B. R., Kulkarni, S. R., Golimowski, D. A., Matthews, K., & Durrance, S. T. 1995, *Nature*, 378, 463
- Oasa, Y., Tamura, M., & Sugitani, K. 1999, *ApJ*, 526, 336
- Oppenheimer, B. R., Golimowski, D. A., Kulkarni, S. R., Matthews, K., Nakajima, T., Creech-Eakman, M., & Durrance, S. T. 2001, *AJ*, 121, 2189
- Parker, S. R., & Tinney, C. G. 2013, *MNRAS*, 430, 1208
- Patience, J., King, R. R., de Rosa, R. J., & Marois, C. 2010, *A&A*, 517, A76
- Pecaut, M. J., Mamajek, E. E., & Bubar, E. J. 2012, *ApJ*, 746, 154
- Perryman, M. A. C. 1997, in *Bulletin of the American Astronomical Society*, Vol. 29, American Astronomical Society Meeting Abstracts, 1314
- Phillips, J. G., & Davis, S. P. 1993, *ApJ*, 409, 860

- Pravdo, S. H., & Shaklan, S. B. 1996, *ApJ*, 465, 264
- Preibisch, T., & Zinnecker, H. 1999, *AJ*, 117, 2381
- Radigan, J., Jayawardhana, R., Lafrenière, D., Artigau, É., Marley, M., & Saumon, D. 2012, *ApJ*, 750, 105
- Radigan, J., Jayawardhana, R., Lafrenière, D., Dupuy, T. J., Liu, M. C., & Scholz, A. 2013, *ApJ*, 778, 36
- Raghavan, D., et al. 2010, *ApJS*, 190, 1
- Rayner, J. T., Cushing, M. C., & Vacca, W. D. 2009, *ApJS*, 185, 289
- Rebolo, R., Zapatero Osorio, M. R., & Martín, E. L. 1995, *Nature*, 377, 129
- Reid, I. N., Cruz, K. L., Burgasser, A. J., & Liu, M. C. 2008a, *AJ*, 135, 580
- Reid, I. N., Cruz, K. L., Kirkpatrick, J. D., Allen, P. R., Mungall, F., Liebert, J., Lowrance, P., & Sweet, A. 2008b, *AJ*, 136, 1290
- . 2008c, *AJ*, 136, 1290
- Reid, I. N., Kirkpatrick, J. D., Gizis, J. E., Dahn, C. C., Monet, D. G., Williams, R. J., Liebert, J., & Burgasser, A. J. 2000, *AJ*, 119, 369
- Rice, E. L., Barman, T., Mclean, I. S., Prato, L., & Kirkpatrick, J. D. 2010, *ApJS*, 186, 63
- Rossow, W. B. 1978, *icarus*, 36, 1
- Ruiz, M. T., Leggett, S. K., & Allard, F. 1997, *ApJ*, 491, L107
- Salpeter, E. E. 1955, *ApJ*, 121, 161
- Saumon, D., & Marley, M. S. 2008, *ApJ*, 689, 1327
- Scalo, J. 1998, in *Astronomical Society of the Pacific Conference Series*, Vol. 142, *The Stellar Initial Mass Function (38th Herstmonceux Conference)*, ed. G. Gilmore & D. Howell, 201
- Schilbach, E., Röser, S., & Scholz, R.-D. 2009, *A&A*, 493, L27
- Schlieder, J. E., Lépine, S., & Simon, M. 2010, *AJ*, 140, 119
- . 2012, *AJ*, 143, 80
- Schneider, A., Melis, C., & Song, I. 2012, *ApJ*, 754, 39
- Schneider, A. C., Cushing, M. C., Kirkpatrick, J. D., Mace, G. N., Gelino, C. R., Faherty, J. K., Fajardo-Acosta, S., & Sheppard, S. S. 2014, *AJ*, 147, 34
- Scholz, A., Geers, V., Clark, P., Jayawardhana, R., & Muzic, K. 2013, *ApJ*, 775, 138
- Scholz, R.-D. 2010, *A&A*, 515, A92
- Schwenke, D. W. 1998, *Faraday Discussions*, 109, 321
- Seifahrt, A., Neuhauser, R., & Hauschildt, P. H. 2007, *A&A*, 463, 309
- Sembach, K. R., & Savage, B. D. 1992, *ApJS*, 83, 147
- Silva, D. R., & Peron, M. 2004, *The Messenger*, 118, 2
- Slesnick, C. L., Hillenbrand, L. A., & Carpenter, J. M. 2004, *ApJ*, 610, 1045

- . 2008, *ApJ*, 688, 377
- Smart, R. L., et al. 2013, *MNRAS*, 433, 2054
- Spezzi, L., et al. 2008, *ApJ*, 680, 1295
- Stephens, D. C., & Leggett, S. K. 2004, *PASP*, 116, 9
- Stone, R. C. 1996, *PASP*, 108, 1051
- Tanaka, H. K. M. 2005, *Journal of Atmospheric and Solar-Terrestrial Physics*, 67, 1544
- Theodossiou, E., & Danezis, E. 1991a, *Ap&SS*, 183, 91
- . 1991b, *Ap&SS*, 183, 91
- Tinney, C. G., Burgasser, A. J., & Kirkpatrick, J. D. 2003, *AJ*, 126, 975
- Todorov, K., Luhman, K. L., & McLeod, K. K. 2010, *ApJ*, 714, L84
- Torres, C. A. O., Quast, G. R., Melo, C. H. F., & Sterzik, M. F. 2008, *Young Nearby Loose Associations*, 757
- Tsuji, T., Ohnaka, K., Aoki, W., & Nakajima, T. 1996, *A&A*, 308, L29
- Vernet, J., et al. 2011, *A&A*, 536, A105
- Vrba, F. J., et al. 2004a, *AJ*, 127, 2948
- . 2004b, *AJ*, 127, 2948
- Wahhaj, Z., et al. 2011, *ApJ*, 729, 139
- Weinberger, A. J., Anglada-Escudé, G., & Boss, A. P. 2013a, *ApJ*, 762, 118
- . 2013b, *ApJ*, 762, 118
- Whittet, D. C. B., Prusti, T., Franco, G. A. P., Gerakines, P. A., Kilkenny, D., Larson, K. A., & Wesselius, P. R. 1997, *A&A*, 327, 1194
- Witte, S., Helling, C., Barman, T., Heidrich, N., & Hauschildt, P. H. 2011, *A&A*, 529, A44
- Zapatero Osorio, M. R., Béjar, V. J. S., Miles-Páez, P. A., Peña Ramírez, K., Rebolo, R., & Pallé, E. 2014, *A&A*, 568, A6
- Zapatero Osorio, M. R., Caballero, J., Martín, E. L., Béjar, V. J. S., & Rebolo, R. 2004a, *Ap&SS*, 292, 673
- Zapatero Osorio, M. R., Lane, B. F., Pavlenko, Y., Martín, E. L., Britton, M., & Kulkarni, S. R. 2004b, *ApJ*, 615, 958
- Zapatero Osorio, M. R., Rebolo, R., Bihain, G., Béjar, V. J. S., Caballero, J. A., & Álvarez, C. 2010, *ApJ*, 715, 1408
- Zuckerman, B., & Song, I. 2004, *ARA&A*, 42, 685
- Zuckerman, B., Song, I., & Webb, R. A. 2001, *ApJ*, 559, 388